NUMERICAL SIMULATION OF CARDIOPULMONARY RESUSCITATION

Jafar Moradicheghamahi

UNIVERSITAT ROVIRA i VIRGILI

Numerical Simulation of Cardiopulmonary Resuscitation

Author:

Jafar MORADICHEGHAMAHI

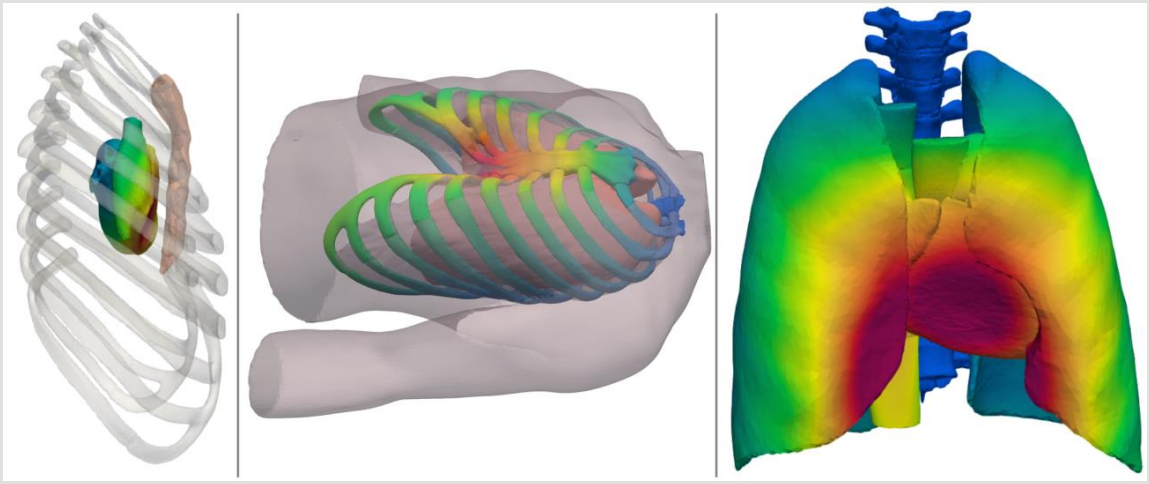

DOCTORAL THESIS

2023

UNIVERSITAT ROVIRA I VIRGILI
NUMERICAL SIMULATION OF CARDIOPULMONARY RESUSCITATION
Jafar Moradicheghamahi

UNIVERSITAT ROVIRA I VIRGILI

DOCTORAL THESIS

Numerical Simulation of Cardiopulmonary Resuscitation

Author:
Jafar MORADICHEGHAMAHI

Supervisors:
Dr. Josep M. LOPEZ
Dr. Gerard FORTUNY

Departament d'Enginyeria Informàtica i Matemàtiques

July, 2023

UNIVERSITAT ROVIRA i VIRGILI

UNIVERSITAT ROVIRA i VIRGILI

FAIG CONSTAR que aquest treball, titulat "Numerical Simulation of Cardiopulmonary Resuscitation", que presenta Jafar Moradicheghamahi per a l'obtenció del títol de Doctor, ha estat realitzat sota la meva direcció al Departament d'Enginyeria Informàtica i Matemàtiques d'aquesta universitat.

HAGO CONSTAR que el presente trabajo, titulado "Numerical Simulation of Cardiopulmonary Resuscitation", que presenta Jafar Moradicheghamahi para la obtención del título de Doctor, ha sido realizado bajo mi dirección en el Departamento de Ingeniería Informática y Matemáticas de esta universidad.

I STATE that the present study, entitled "Numerical Simulation of Cardiopulmonary Resuscitation", presented by Jafar Moradicheghamahi for the award of the degree of Doctor, has been carried out under my supervision at the Department of Computer Engineering and Mathematics of this university.

Tarragona, 27 de Julio de 2023

El/s director/s de la tesi doctoral
El/los director/es de la tesis doctoral
Doctoral Thesis Supervisor/s

Dr. Josep Maria López Besora

Dr. Gerard Fortuny Anguera

The research presented in this thesis was carried out with funding from the Universitat Rovira i Virgili (URV) under Grant 2018PFR-URV-B2-29.

UNIVERSITAT
ROVIRA i VIRGILI

UNIVERSITAT ROVIRA I VIRGILI

Abstract

Departament d'Enginyeria Informàtica i Matemàtiques

Doctor of Philosophy

Numerical Simulation of Cardiopulmonary Resuscitation

by Jafar MORADICHEGHAMAHI

Cardiac arrest, responsible for a significant number of fatalities amounting to 800,000 in Europe and the US, poses a major challenge. Despite considerable research efforts directed towards cardiopulmonary resuscitation (CPR), the survival rate following cardiac arrest remains dishearteningly low, below 10 percent. Thus, it is imperative to continue investigating CPR to enhance survival outcomes. However, conducting extensive clinical and laboratory studies poses limitations and high costs. Consequently, numerical methods, notably the finite element (FE) method, have gained prominence in medical research, including CPR studies, as a cost-effective and efficient alternative.

The impact of thoracic cage dimensions on CPR outcomes has been a subject of debate. These dimensional parameters play a crucial role in determining CPR success and can provide patient–specific CPR instructions based on individual

thoracic characteristics. Although limited clinical studies have explored the effect of thorax dimensions on CPR outcomes, the specific influence of dimensional parameters remains unclear, warranting further investigation. In this study, realistic FE models were employed to examine the impact of various factors on CPR outcomes, with a focus on compression depth and maximum ribcage stress. Thus, the primary objective of this study was to analyze the effects of thoracic dimensions on CPR outcomes. Additionally, a comprehensive FE model encompassing all internal thoracic organs during CPR has not been previously presented. Therefore, the second objective of this study is to develop a comprehensive realistic FE model for simulating CPR and evaluating the behavior, deformation, and response patterns of different internal organs, thereby providing valuable insights into the resuscitation process.

We employed FE simulations to examine how alterations in rib cage dimensions impact compression depth during CPR. We explored 216 different models of rib cage geometries and conducted simulations with varying compression forces up to 600 N. Our findings demonstrate that rib cages characterized by a low Haller Index and/or greater height tend to achieve lower compression depths when a fixed compression force is applied. Conversely, individuals with higher Haller Index and/or lower chest height generally require lower compression forces to attain a target compression depth. Furthermore, individuals with a wider chest experience reduced levels of rib stress while achieving the desired compression depth. To enhance future empirical correlations of CPR data, we propose predictive models that incorporate anthropometric parameters, with the patients' Haller Index and vertical cross-area serving as appropriate independent variables for compression depth and rib stress during chest compressions.

The findings from the comprehensive model simulation demonstrate that applying a force within the range of approximately 440-540 N successfully achieves the recommended compression depth of 5-6 cm. This leads to heart volume changes between 15.6 and 20.1 %, as well as lung volume changes ranging from 13.4 to 16.6 %. Notably, smaller hearts experience more pronounced deformations, whereas larger hearts result in substantial lung volume alterations.

In the final step of the study, the impact of time factor and compression rate, a time-dependent parameter, were examined using a viscoelastic rib model in dynamic CPR simulations. The force-deflection curves displayed residual deflection and hysteresis, illustrating the ribcage's tendency to deform time-dependently and resist immediate recovery. Notably, an initial substantial residual deflection was observed, followed by minimal increases in subsequent cycles. The variations in heart and lung volume over time indicated a progressive decrease in the capacity for cardiac and thoracic pumping. A comparison between compression rates of 100 and 120 compressions per minute unveiled disparities in maximum compression depth, with the lower compression rate allowing for deeper compressions. Notably, changes in heart and lung volumes at the higher compression rate suggested a negative impact on cardiac and thoracic pump efficiency, characterized by reduced maximum volumes and increased minimum volumes.

The FEM models employed in this study serve as valuable tools for evaluating the influence of various parameters on CPR outcomes, enhancing our insight into CPR and offering potential improvements. These models demonstrate a high capability in studying the affecting parameters in CPR.

UNIVERSITAT ROVIRA I VIRGILI
NUMERICAL SIMULATION OF CARDIOPULMONARY RESUSCITATION
Jafar Moradicheghamahi

Resum

L'aturada cardíaca, responsable d'un nombre significatiu de defuncions que arriba als 800.000 a Europa i als Estats Units, suposa un gran desafiament. Malgrat els considerables esforços de recerca dirigits cap a la reanimació cardiopulmonar (RCP), la taxa de supervivència després d'una aturada cardíaca continua sent decebedorament baixa, per sota del 10 per cent. Per tant, és imprescindible continuar investigant la RCP per millorar els resultats de supervivència. No obstant això, realitzar extensos estudis clínics i de laboratori té limitacions i costos elevats. En conseqüència, els mètodes numèrics, especialment el mètode dels elements finits (FE), han guanyat rellevància en la recerca mèdica, inclosos els estudis de RCP, com una alternativa econòmica i eficient.

L'impacte de les dimensions de la caixa toràcica en els resultats de la RCP ha estat objecte de debat. Aquests paràmetres dimensionals juguen un paper crucial en la determinació de l'èxit de la RCP i poden proporcionar instruccions específiques per a la RCP basades en les característiques toràciques individuals. Tot i que s'han realitzat estudis clínics limitats per explorar l'efecte de les dimensions del tòrax en els resultats de la RCP, la influència específica dels paràmetres dimensionals encara no està clara i requereix més investigació. En aquest estudi, s'han utilitzat models realistes de FE per examinar l'impacte de diversos factors en els resultats de la RCP, amb un enfocament en la profunditat de la compressió i l'estrès màxim de la caixa toràcica. Per tant, l'objectiu principal d'aquest estudi va ser analitzar els efectes de les dimensions toràciques en els resultats de la RCP. A més, no s'ha presentat anteriorment un model de FE realista i exhaustiu que

englobi tots els òrgans interns toràcics durant la RCP. Per tant, el segon objectiu d'aquest estudi és desenvolupar un model de FE realista i exhaustiu per simular la RCP i avaluar el comportament, la deformació i els patrons de resposta dels diferents òrgans interns, proporcionant així informació valuosa sobre el procés de reanimació.

Hem utilitzat simulacions de FE per examinar com les alteracions en les dimensions de la caixa toràcica afecten la profunditat de la compressió durant la RCP. Hem explorat 216 models diferents de geometries de la caixa toràcica i hem realitzat simulacions amb forces de compressió variables fins a 600 N. Les nostres troballes demostren que les gàbies toràciques caracteritzades per un índex de Haller baix i/o una altura més gran tendeixen a assolir profunditats de compressió més baixes quan s'aplica una força de compressió fixa. Al contrari, les persones amb un índex de Haller més alt i/o una altura de pit més baixa generalment requereixen forces de compressió més baixes per aconseguir una profunditat de compressió objectiu. A més, les persones amb un pit més ample experimenten nivells més baixos d'estrès a les costelles mentre aconsegueixen la profunditat de compressió desitjada. Per millorar futures correlacions empíriques de les dades de RCP, proposem models predictius que incorporin paràmetres antropomètrics, sent l'índex de Haller dels pacients i l'àrea de secció vertical variables independents adequades per a la profunditat de la compressió i l'estrès a les costelles durant les compressions toràciques.

Els resultats de la simulació del model exhaustiu demostren que l'aplicació d'una força dins del rang aproximat de 440-540 N aconsegueix amb èxit la profunditat de compressió recomanada de 5-6 cm. Això porta a canvis de volum cardíac

entre el 15,6 i el 20,1 %, així com a canvis de volum pulmonar que oscil·len entre el 13,4 i el 16,6 %. Cal destacar que els cors més petits experimenten deformacions més pronunciades, mentre que els cors més grans provoquen canvis substancials en el volum pulmonar.

En l'últim pas de l'estudi, es va examinar l'impacte del factor de temps i la velocitat de compressió, un paràmetre dependent del temps, utilitzant un model viscoelàstic de costelles en simulacions dinàmiques de RCP. Les corbes de força-deflexió van mostrar una deflexió residual i histèresi, il·lustrant la tendència de les costelles a deformar-se de manera dependent del temps i resistir la recuperació immediata. Cal destacar que es va observar una deflexió residual substancial inicial, seguida d'increments mínims en cicles posteriors. Les variacions del volum del cor i del pulmó al llarg del temps van indicar una disminució progressiva de la capacitat de bombament cardíac i toràcic. Una comparació entre les taxes de compressió de 100 i 120 compressions per minut va revelar disparitats en la profunditat màxima de compressió, amb la taxa de compressió més baixa permetent compressions més profundes. Cal destacar que els canvis en els volums del cor i del pulmó a la taxa de compressió més alta van suggerir un impacte negatiu en l'eficiència de la bomba cardíaca i toràcica, caracteritzat per volums màxims reduïts i volums mínims augmentats.

Els models de FE utilitzats en aquest estudi serveixen com a eines valuoses per avaluar la influència de diversos paràmetres en els resultats de la RCP, millorant la nostra comprensió de la RCP i oferint millores potencials. Aquests models demostren una gran capacitat per estudiar els paràmetres que afecten la RCP.

Resumen

La parada cardíaca, responsable de un número significativo de muertes que alcanza los 800.000 en Europa y Estados Unidos, representa un desafío importante. A pesar de los considerables esfuerzos de investigación dirigidos hacia la reanimación cardiopulmonar (RCP), la tasa de supervivencia después de una parada cardíaca sigue siendo desalentadoramente baja, por debajo del 10 por ciento. Por lo tanto, es imperativo seguir investigando la RCP para mejorar los resultados de supervivencia. Sin embargo, llevar a cabo extensos estudios clínicos y de laboratorio presenta limitaciones y altos costos. En consecuencia, los métodos numéricos, en particular el método de elementos finitos (FE), han ganado importancia en la investigación médica, incluidos los estudios de RCP, como una alternativa rentable y eficiente.

El impacto de las dimensiones de la caja torácica en los resultados de la RCP ha sido objeto de debate. Estos parámetros dimensionales desempeñan un papel crucial en la determinación del éxito de la RCP y pueden proporcionar instrucciones de RCP específicas para cada paciente en función de las características torácicas individuales. Aunque se han realizado estudios clínicos limitados sobre el efecto de las dimensiones del tórax en los resultados de la RCP, la influencia específica de los parámetros dimensionales sigue sin estar clara, lo que justifica una mayor investigación. En este estudio, se utilizaron modelos realistas de FE para examinar el impacto de diversos factores en los resultados de la RCP, con un enfoque en la profundidad de compresión y el estrés máximo de la caja torácica. Por lo tanto, el

objetivo principal de este estudio fue analizar los efectos de las dimensiones torácicas en los resultados de la RCP. Además, no se ha presentado previamente un modelo completo de FE realista que abarque todos los órganos torácicos internos durante la RCP. Por lo tanto, el segundo objetivo de este estudio es desarrollar un modelo completo y realista de FE para simular la RCP y evaluar el comportamiento, deformación y patrones de respuesta de los diferentes órganos internos, proporcionando así conocimientos valiosos sobre el proceso de reanimación.

Empleamos simulaciones de FE para examinar cómo las alteraciones en las dimensiones de la caja torácica afectan la profundidad de compresión durante la RCP. Exploramos 216 modelos diferentes de geometrías de la caja torácica y realizamos simulaciones con fuerzas de compresión variables de hasta 600 N. Nuestros hallazgos demuestran que las cajas torácicas caracterizadas por un índice de Haller bajo y/o mayor altura tienden a lograr profundidades de compresión más bajas cuando se aplica una fuerza de compresión fija. Por el contrario, las personas con un índice de Haller más alto y/o una altura torácica más baja generalmente requieren fuerzas de compresión más bajas para alcanzar una profundidad de compresión objetivo. Además, las personas con un pecho más ancho experimentan niveles reducidos de estrés en las costillas mientras logran la profundidad de compresión deseada. Para mejorar futuras correlaciones empíricas de datos de RCP, proponemos modelos predictivos que incorporen parámetros antropométricos, siendo el índice de Haller de los pacientes y el área transversal vertical variables independientes apropiadas para la profundidad de compresión y el estrés en las costillas durante las compresiones torácicas.

Los hallazgos de la simulación del modelo completo demuestran que aplicar

una fuerza dentro del rangoaproximado de 440-540 N logra con éxito la profundidad de compresión recomendada de 5-6 cm. Esto conduce a cambios en el volumen del corazón entre 15,6 y 20,1 %, así como cambios en el volumen pulmonar que oscilan entre 13,4 y 16,6 %. Es importante destacar que los corazones más pequeños experimentan deformaciones más pronunciadas, mientras que los corazones más grandes resultan en alteraciones sustanciales del volumen pulmonar.

En la etapa final del estudio, se examinó el impacto del factor tiempo y la tasa de compresión, un parámetro dependiente del tiempo, utilizando un modelo de costilla viscoelástica en simulaciones dinámicas de RCP. Las curvas de fuerza-deflexión mostraron deflexión residual e histéresis, ilustrando la tendencia de las costillas a deformarse de manera dependiente del tiempo y resistir una recuperación inmediata. Es importante destacar que se observó una deflexión residual inicial sustancial, seguida de aumentos mínimos en ciclos posteriores. Las variaciones en el volumen del corazón y los pulmones a lo largo del tiempo indicaron una disminución progresiva en la capacidad de bombeo cardíaco y torácico. Una comparación entre las tasas de compresión de 100 y 120 compresiones por minuto reveló disparidades en la profundidad máxima de compresión, siendo la tasa de compresión más baja la que permitía compresiones más profundas. Es importante destacar que los cambios en los volúmenes del corazón y los pulmones a la tasa de compresión más alta sugirieron un impacto negativo en la eficiencia de bombeo cardíaco y torácico, caracterizado por una reducción en los volúmenes máximos y un aumento en los volúmenes mínimos.

Los modelos de elementos finitos empleados en este estudio son herramientas valiosas para evaluar la influencia de varios parámetros en los resultados de la

RCP, mejorando nuestra comprensión de la RCP y ofreciendo posibles mejoras. Estos modelos demuestran una gran capacidad para estudiar los parámetros que afectan a la RCP.

Acknowledgements

I would like to express my sincere appreciation to the Martí i Franquès Fellowship at Rovira i Virgili (URV) University for their generous financial support, which has been instrumental in the completion of this research. It has been a great honor to be affiliated with URV, and I am grateful for the academic freedom provided throughout this study.

I am deeply grateful to my supervisors, Dr. Josep M. López, Dr. Gerard Fortuny, Dr. Joan Herrero, Dr. Dolors Puigjaner, and Dr. Youcef Azeli. Their guidance and mentorship have been invaluable, particularly during my initial year of PhD studies. Our regular meetings have played a significant role in honing my skills in the field of Biomechanics. I extend my heartfelt thanks to each of them for their patience during challenging times, their constructive feedback during discussions and presentations, and their dedication in reviewing and correcting my manuscripts. The collaborative experience, particularly in developing our new anisotropic-viscoelastic constitutive model, has been truly enriching.

I would like to extend a special thank you to Dr. López and Dr. Fortuny for their assistance with study-related paperwork and their prompt responsiveness to my emails and messages, even during weekends and late hours. I appreciate their unwavering support and optimism. To Dr. Herrero, my Cum Laude supervisor, I am grateful for your kindness and approachability, and for taking the time to address my inquiries and clarify any doubts. Dr. Puigjaner, as one of the project module leaders, I extend my heartfelt appreciation for your encouragement and support throughout this research endeavor. Dr. Azeli, I am grateful for your

guidance and the time you dedicated to editing my manuscripts.

To all my friends at the university, I am thankful for the enriching conversations and encouragement we have shared. My office mates, Qasim, Najeeb, Younes, Benet, Carlos, and Faisal have been valuable collaborators, and I appreciate their unwavering assistance. I would also like to extend my thanks to my friends Saeed, Amin, Foad, and Ciroos for their continuous support and motivation.

Finally, my heartfelt appreciation goes to my family for their unwavering love, affection, and moral support throughout this journey.

Contents

List of Figures

List of Tables

Nomenclature

3D	Three (**3**) **D**imentional
δ_{ij}	Kronecker delta
$\delta_x, \delta_y, \delta_z$	strechingcompressing ratios
ε	Strain
η	Poisson Ratio, Viscous Coefficient
θ	Rib Angle
λ	Lamé Constant
$\dot{\lambda}$	Non-Negative Hardening Parameter
μ	Lamé Constant
ν	Poisson Ratio
σ	Stress
σ_{Mises}	Von-Mises equivalent Stress
A	**A**rea
AHA	**A**merican **H**eart **A**ssociation
BVC	**B**lood **V**olume **C**hange
C	Stiffness Tensor
CA	**C**ardiac **A**rrest
CPR	**C**ardio**p**ulmonary **R**esuscitation
CT	**C**omputerized **T**omography

D	**D**iameter
E	**E**lastic Modulus
e	Deviatoric Strain Tensor
ERC	**E**uropean **R**esuscitation **C**ouncil
F	**F**orce
FE	**F**inite **E**lement
$f(\sigma)$	Yield Function
G	Shear Modulus
H	**H**eight
H	Plastic Modulus
HI	**H**aller **I**ndex
HVC	**H**eart **V**olume **C**hange
J_1, J_2, J_3	Invariants of Stress Tensor
k	Material Parameter Representative the Yield Stress
L	**L**ength
LLVC	**L**eft **L**ung **V**olume **C**hange
LVC	**L**ung **V**olume **C**hange
LVVC	**L**eft **V**entricle **V**olume **C**hange
OHCA	**O**ut of **H**ospital **C**ardiac **A**rrest
RLVC	**R**ight **L**ung **V**olume **C**hange
ROSC	**R**eturn **o**f **S**pontaneous **C**irculation
RVVC	**R**ight **V**entricle **V**olume **C**hange
S	Compliance Tensor
s	Deviatoric Stress Tensor
V	**V**olume

W	**W**idth
DOF	**D**egree **o**f **F**reedom

TO MY FAMILY

Chapter 1

Introduction

In this chapter, information is presented on the overall context of Cardiopulmonary resuscitation (CPR), including background research on CPR and finite element (FE) models. The goals of the thesis are also explained. Furthermore, the chapter includes an outline of the thesis structure and an index of the quality of the scientific papers that have been published or are currently in progress.

1.1 Background

Many medical emergencies require immediate intervention to save a patient's life. The total number of Cardiac Arrests (CA) in the United States and Europe is reported to exceed 700,000 per year, out of which only approximately 50,000 patients are able to survive and be discharged from the hospital [1]. Apart from the well-known causes of cardiac arrest, including coronary artery disease, heart attack, heart failure, abnormal heart rhythms (arrhythmias), and certain inherited heart

disorders, there are other contributing circumstances that can result in cardiac arrest. These encompass scenarios such as drowning, choking, drug overdose, and trauma-related cardiac arrest. Drowning is a leading cause of accidental death with approximately 372000 drowning deaths occurring in the world each year [2]. While it's difficult to estimate the number of suffocation emergencies that occur annually, choking is a common cause of accidental death in children worldwide [3, 4]. In 2018, the number of drug overdose deaths reported in Europe was 8,317, while the United States reported 67,367 drug overdose deaths in the same year [5, 6]. Out-of-hospital trauma-related CA is a leading cause of death with a very poor survival rate [7].

Cardiopulmonary resuscitation (CPR) is an emergency procedure that combines chest compressions often with artificial ventilation in an effort to manually preserve intact brain function until further measures are taken to restore spontaneous blood circulation and breathing [8]. In all of the mentioned emergencies causing CA, CPR can be a crucial intervention that helps to maintain vital blood flow to vital organs until more advanced medical care can be provided, and it can mean the difference between life and death.

CPR has a long and evolving history. The first documented case of chest compressions was performed by Dr. Friedrich Maass, a German surgeon in 1891 [9]. Then, in the 1950s, Dr. Peter Safar and Dr. James Elam developed the rescue breathing technique, which allowed for the restoration of breathing in patients who had stopped breathing [10]. The American Heart Association (AHA) published the first guidelines for CPR in 1960, which was followed by subsequent updates and revisions over the years [11]. Today, CPR continues to be refined and

improved, and it remains a critical technique that has saved countless lives.

CPR guidelines have undergone significant changes and improvements over time to optimize the effectiveness of resuscitation techniques. AHA published the first CPR guidelines in 1960. The initial guidelines recommended a compression depth of 1.5 to 2 inches for adults, with a compression rate of 60 compressions per minute. Two breaths of artificial respiration were also recommended after every 15 compressions [12]. Subsequent revisions to the AHA guidelines aimed to improve the quality of CPR by optimizing the chest compression-to-ventilation ratio. In 2005, AHA increased the recommended compression rate to 100 compression per minute and a compression-to-ventilation ratio of 30:2 was recommended [13]. In 2010, the recommended compression depth was increased to at least 2 inches [14]. Similarly, the European Resuscitation Council (ERC) released their first CPR guidelines in 1992, which emphasized high-quality chest compressions with a compression-to-ventilation ratio of 5:1 [15]. The ERC guidelines have been updated several times, with the most recent version published in 2021, which is in line with the AHA guidelines. Currently, both the AHA and ERC guidelines are widely used in Europe and the USA. The ERC guidelines, last updated in 2021, recommend a compression depth of at least 5 to 6 cm, a compression rate of 100 to 120 compressions per minute, and a compression-to-ventilation ratio of 30:2 for adults [16]. The components of high quality CPR recommended by the latest update of AHA guideline are almost the same [17].

However, CPR is not always successful in reviving patients, and there are limitations to its effectiveness. According to the American Heart Association, less than 10% of people who experience CA outside of a hospital setting survive [18].

Additionally, CPR can also cause injuries such as rib fractures, which occur in up to 30% of patients who receive CPR [19]. Even when CPR is performed, the survival rate varies depending on various factors such as age, underlying health conditions, and the response time of emergency medical services [20]. These limitations emphasize the need for continued research and development in CPR techniques to improve its effectiveness and ultimately save more lives. Despite these risks, CPR remains a crucial tool in emergency situations and ongoing research can help improve its outcomes while minimizing its negative effects.

Different types of studies have been conducted to evaluate the effectiveness of CPR. Clinical studies on patients are considered the most reliable and relevant, as they provide direct evidence of the effectiveness of different CPR techniques. However, ethical concerns limit the extent to which these studies can be conducted, and the findings may be affected by confounding factors such as differences in patient populations and variations in the quality of CPR delivery [21, 22]. Studies on Cadaver models, while less ethically problematic, may not accurately reflect the effectiveness of CPR in a live patient [23]. Animal studies have been used to address some of the ethical concerns of human studies, but the differences between animal and human anatomy and physiology may limit the applicability of the findings to human patients [24]. Another type of CPR study is the use of manikins, which have been increasingly used in recent years due to their cost-effectiveness and reproducibility. However, there are several disadvantages and limitations associated with the use of manikins. Firstly, it can be difficult to prepare a manikin that closely mimics the tissue behavior of a real patient, which may affect the accuracy of the results obtained. Additionally, manikins may not be able to take into account the variations in patient body dimensions and other

factors that may impact the effectiveness of CPR. Finally, preparing a manikin for use can be quite expensive, which may limit its use in certain settings [25].

Numerical simulation is a method of creating computer-based models that simulate real-world scenarios. In the context of CPR, numerical simulations can be used to study the efficacy of different CPR techniques and the impact of various factors on resuscitation outcomes. One commonly used numerical simulation method is the finite element (FE) method, which is a mathematical technique used to compute approximations of real solutions to partial differential equations. FE method is a useful tool for studying CPR because it allows researchers to create accurate and detailed models of the human body, including the chest and heart, which are involved in CPR [26]. Unlike other types of CPR studies, FE simulations do not have ethical concerns associated with clinical studies, and they do not have the problem of differences among species that arise in animal studies. Furthermore, FE simulations allow researchers to investigate the effect of a wide range of factors, such as compression depths, compression rates, thoracic dimensions, bone properties, and many other factors which can be difficult or impossible to consider in other types of CPR studies. Another advantage of using FE simulations for CPR research is that they are relatively low-cost compared to other types of CPR studies. However, there are some limitations to this method. One limitation is that FE simulations rely on assumptions and simplifications, which may not accurately reflect the complex dynamics of real-world scenarios [26]. Additionally, creating accurate FE models of the human body can be time-consuming and require specialized knowledge and expertise [27]. Despite these limitations, FE simulations are a valuable tool for investigating CPR techniques and optimizing resuscitation outcomes.

In conclusion, the FE method has proven to be a valuable tool in conducting CPR studies. It allows for the investigation of multiple factors in a controlled and ethical manner without the limitations of other types of CPR studies. This thesis aims to investigate the effects of various factors on CPR using FE models. The first step involves examining the impact of thorax dimensions on compression depth and ribcage stress. The second step will focus on providing comprehensive models for CPR and examining the effects of applied force levels on different organs, including the ribcage, heart chambers, and lungs. Finally, in the third step, the effects of compression rate will be investigated by means of a more sophisticated dynamical FE model that allows us to incorporate the temporal aspect in the simulations. By utilizing FE, this thesis can provide a more detailed understanding of the mechanisms of CPR and contribute to the development of more effective resuscitation techniques.

1.2 Literature Review

CA is a significant public health concern in developed nations and is responsible for a substantial number of deaths [28, 29]. Out-of-hospital CA is a common occurrence, but only a small proportion of patients receive chest compressions as part of basic life support, resulting in a low rate of return of spontaneous circulation (ROSC) at 8.3% and a low survival rate until hospital discharge at 4.12% [18, 30]. Therefore, the timely and high-quality administration of CPR is crucial, as the

chances of survival for patients with CA depend on the effectiveness of CPR interventions in the initial minutes following the event [31]. Therefore, having knowledge about the criteria for high-quality CPR is essential. However, acquiring this knowledge is not an easy task due to the many limitations in studies related to CPR and the abundance of parameters involved in CPR quality. In the following, we will review some of these parameters that have been investigated in previous studies.

The technique of chest compressions was first described in 1960 and has remained largely unchanged until recently [11]. Studies have shown that during CPR, the blood flow is closely related to the depth of chest compressions [32]. In 2010, resuscitation guidelines recommended an increase in the compression depth from 4 cm to 5 cm [33]. However, controversy arose within the scientific community when higher survival rates were reported for compression depths ranging from 4.03 to 5.53 cm with the highest survival rate at 4.56 cm during out of hospital cardiac arrests (OHCA) [34]. However, the latest CPR guidelines still recommend a compression depth between 5 and 6 cm for the average adult [35]. Despite this, recent studies based on large patient samples have suggested that smaller compression depths, such as 4.56 cm or 4.7 cm, are associated with the highest survival rates [36]. Therefore, it is clear that the quality of CPR is highly dependent on achieving an appropriate compression depth.

In attempting to improve CPR technique, it is important to consider the potential injury risk associated with chest compressions. Although in CPR with a deeper chest compression the probability of blood recirculation is higher, it also has a higher probability of causing injuries, including skeletal fractures, upper

airway complications, pulmonary barotraumas, hemothorax, and lacerations of internal organs [37]. While skeletal chest injuries produced by CPR are generally considered insignificant, some thoracic lesions have potentially fatal consequences [38, 39]. Thoracic CPR-related injuries have been linked to the loss of thoracic elasticity and poorer survival outcomes [40], and have recently been identified as an independent factor associated with poor prognosis [41]. Serious thoracic lesions secondary to CPR can result in a deterioration of the elastic properties of the thorax. Thus, the potential injuries suffered by victims must be considered as a complementary standard for determining the quality of CPR. Increasing the compression depth during CPR can enhance cardiac output but can also increase the incidence of injury and worsen hemodynamics [42, 43]. To maintain a high probability of saving lives while minimizing injury risk, more research is needed to optimize CPR technique.

Several studies have investigated the influence of the mechanical properties of the surface on which CPR is performed on patient outcomes [44–50]. The data suggest that performing CPR on a hard surface results in better chest compression and hence better quality of CPR [45, 46, 50, 51]. However, despite these findings, most in-hospital emergency CPRs for children are performed on soft surfaces [52, 53]. To improve the quality of CPR on soft surfaces, the 2005 International Consensus on Resuscitation Science recommended inserting a backboard under the patient to reduce the deflection of the soft mattress (Resuscitation 2005).

Hands position is an important factor in the effectiveness of CPR. However,

current CPR guidelines do not provide much specificity on this issue, only suggesting that compressions should be performed on the lower half of the breastbone [54]. The 2020 AHA guidelines for CPR and emergency cardiovascular care, 2021 ERC Guidelines, and 2020 Korean guidelines all support this hand placement recommendation [16, 17, 55, 56]. Studies on swine models have found that performing chest compressions at the left ventricle can increase coronary perfusion pressure, improve hemodynamics, and increase the rate of return of spontaneous circulation (ROSC) [57]. However, compression of the aortic root may have an adverse effect on the efficacy of CPR by increasing resistance to forward blood flow from the left ventricle [58].

The quality of CPR can be affected by numerous parameters, many of which are related to the physical characteristics of the patient. Extensive research has been conducted in recent years to provide patient-specific criteria to improve the quality of CPR. Medical teams specialized in the resuscitation of critical patients perform personalized hemodynamic-directed CPR maneuvers with complex protocols that consider several parameters, including compression depth and compression point location, among others [59–61]. The CPR guideline has prescribed chest compression depth for patients of different ages [62]. CPR performed on children differs from that performed on adults, and in clinical practice, CPR is divided into adult and pediatric categories [26]. CPR techniques differ between these two groups, and the frequencies of injuries, such as rib fractures, are known to be rare among pediatric subjects while being frequent in adult and especially elderly subjects [63–65].

Recent literature strongly supports the notion that the dimensions of each individual patient should be taken into account when establishing a target compression depth for CPR [66–69]. Very few studies have been conducted in this area, and the results are somewhat contradictory. One clinical study found that patients with low thoracic volume and dimensions had a higher incidence of CPR-related thoracic injury when compression depth and frequency were standardized [70]. However, another clinical study concluded that iatrogenic thoracoabdominal injuries caused by CPR were independent of thoracic diameters when performed according to the guidelines [71]. These findings suggest that further research is needed to fully understand the relationship between thoracic dimensions and CPR performance. It is important to consider these factors when developing CPR protocols and training programs to improve patient outcomes. One of the primary purposes of this thesis is to investigate the effect of thoracic dimensions on CPR performance indicators.

To date, no study has quantified the deformation of the heart and lungs during CPR, and the primary focus of studies in this area has been on the mechanism of blood flow and the behavior of various components of the heart and lungs during closed-chest CPR. Two main theories have been proposed, namely the "cardiac pump" and "thoracic pump"[72]. The "cardiac pump theory" suggests that blood flows during compression due to direct squeezing of the heart between the spine and sternum, while the "thoracic pump" theory postulates that intrathoracic pressure during compression exceeds extrathoracic vascular pressure, forcing blood to flow from the thoracic to systemic vessels with the heart acting as a passive conduit [73–75]. The timing from cardiovascular collapse to CPR has been found to be a significant determinant of the observed pump mechanism, with shorter

times associated with the cardiac pump mechanism and longer times with the thoracic pump mechanism, likely due to myocardial stiffness [76]. Gaining a comprehensive understanding of the intricate mechanisms and physiological interactions that govern the behavior of thoracic internal organs during CPR is paramount in directing future research endeavors to enhance survival rates and outcomes for patients who have experienced CA [76].

Numerical methods have gained increasing popularity in recent years as an alternative to overcome some of the limitations involved in traditional CPR studies. FE simulations have been utilized to study CPR due to the challenges of conducting studies on human corpses [77]. By utilizing the FE model of the thorax with anatomical detail, the exact rib strains can be predicted and compared with literature data on rib damage, making it an essential tool for studying CPR [78]. To assess the potential risks of injury caused by pediatric CPR and to study how variations of the pediatric victim chest affect CPR quality, a detailed biomechanical pediatric thorax surrogate is necessary. Previous FE studies have mainly focused on simulating car crash conditions to examine rib cage responses to compression [79–82]. To date, no research has been conducted to develop a comprehensive FE method model for CPR, and it is clear that such a model is necessary. Despite the increasing popularity of numerical methods in studying CPR due to the limitations of traditional methods, there is still a gap in the literature regarding a comprehensive FE model for CPR. The development of such a model would provide valuable insights into the physical characteristics of CPR and allow for a more accurate prediction of the effects of CPR on the thorax and ribs. Additionally, it would enable the evaluation of potential risks of injury due to CPR and contribute to the optimization of CPR techniques.

1.3 Goal of the Thesis

The primary objective of this thesis is to utilize the FE method as an effective tool for advancing the knowledge of CPR, taking advantage of its unique strengths over traditional study approaches. To achieve this, we have used two types of FE models. A simple model to analyze the impact of dimensional parameters on CPR output, and a comprehensive model to examine the behavior of various organs during CPR. Through these FE models, we aim to accomplish the following objectives:

- To study the relationship between thoracic dimensions and compression depth during CPR.
- To investigate the effect of thoracic dimensions on rib fractures during CPR under the application of a specific force.
- To identify the most relevant thoracic dimensions that affect CPR outcomes and propose suitable dimensional parameters to capture these effects.
- To derive mathematical equations that can predict compression depth and maximum ribcage stress based on these dimensional parameters.
- To integrate a comprehensive FE model of the thorax that includes all relevant organs involved in CPR.
- To study the behavior of different organs under the application of varying levels of force.

- To examine the effect of the time factor on the behavior of the different organs.
- To investigate the effect of the compression rate on the deformation of different organs.

1.4 Thesis Structure

This research is divided into three sub-studies. The first sub-study focuses on examining the effects of the thoracic dimensional parameter, while the second sub-study investigates the behavior of different organs during CPR using a comprehensive FE model. The methodology, results, and discussion pertaining to these two sub-studies can be found in Chapters 2, 3, and 4. The third sub-study, which explores the effects of the time factor and compression rate using dynamic simulation, is presented in Chapter 5 in its entirety. The structure of each chapter of the thesis has been presented in this section.

Chapter 2 provides the methodology of the research, which consists of two sub-studies. The chapter discusses the creation of geometries, the development of material properties, software used, mesh generation, and important description for both studies.

In Chapter 3, the findings are presented. The chapter starts by highlighting the outcomes of the study that investigated the effects of thoracic dimensions. It explores the connection between chest dimensional parameters and compression depth, as well as ribcage maximum stress. Predictive equations are introduced to

estimate these parameters based on dimensional factors. Furthermore, the chapter discusses the results of the comprehensive models, specifically the deformation of internal organs like the myocardium, heart chambers, and lungs. The examination also considers how heart size influences these deformations.

Chapter 4 conducts a comprehensive analysis of the findings from Chapter 3. It discusses the equations for compression depth and ribcage maximum stress, aiming to simplify them while maintaining precision. The chapter provides a detailed examination of the simulation results on the full model, comparing them with existing theoretical mechanisms of CPR described in the literature.

Chapter 5 investigates the influence of the time factor and compression rate in CPR simulations by utilizing a dynamic simulation and a viscoelastic model for ribs and intercostal muscles. The chapter focuses on analyzing the force-deflection curves, which highlight the impact of the ribcage's viscoelastic properties and enable a comparison of the study's findings with experimental data. Furthermore, the chapter examines the temporal changes in heart and lung volume to explore the behavior of the ribcage, heart, and lungs over time. Lastly, the results are presented to study the effect of compression rate, considering two different compression rates.

Chapter 6 serves as the concluding chapter, highlighting the key contributions and main conclusions of the dissertation. It emphasizes the significance of these findings. Additionally, the chapter outlines potential avenues for future research and further developments in the field. These proposed research directions aim to enhance our knowledge of CPR techniques, improve patient outcomes, and contribute to the advancement of the field.

1.5 Publication List

Some of the results presented in this thesis are from the following published/in–progress articles.

1. **Moradicheghamahi J**, Fortuny G, López JM, Puigjaner D, Herrero J, Azeli Y. "The effect of thoracic dimensions on compression depth during cardiopulmonary resuscitation." *International Journal for Numerical Methods in Biomedical Engineering* (2023): e3718.

2. **Moradicheghamahi J**, Fortuny G, López JM, Herrero J, Puigjaner D. "Deformation of the myocardium during CPR." *arXiv preprint arXiv* (2022): 2205.15804.

Chapter 2

Methodology

This chapter will cover the different methods used in carrying out this research. The creation of geometries and the development of material properties for the constitutive models are the most crucial elements of the methodology employed in this study. This thesis is comprised of three sub-studies. In the first sub-study, which we will refer to as "study 1" hereafter, we aim to investigate the impact of chest dimensions on CPR outcomes, specifically compression depth and maximum induced stress in the ribs. In the second sub-study, which we will refer to as "study 2," we aim to present a comprehensive FE model to better understand the behavior of internal organs under the application of force on the sternum, as well as the effect of heart size on CPR outcomes. The third study, which involves the dynamic simulation of CPR, will be presented in Chapter 5. In study 2, the models used were developed by building upon the base model used in study 1. Therefore, in each section, we first discuss the details of study 1 and then describe the modifications made to the base model to create the comprehensive model used in study 2. In addition to the presentation of geometric models and material properties, this chapter will also include the discussion of used software, generated meshes and other important definitions.

2.1 Geometry resources and software

This thesis exclusively employed open-source and costume-made software. The refined models were created by improving a raw model from the BodyParts3D database [83], which was initially obtained by segmenting CT images of an adult man. This database consists of 3-D triangular surface models defining individual elements like bones, muscles, and organs. The 3-D surface meshes were modified to ensure consistency and integrity using homemade and open-source software [84]. The set of 3-D meshes were then processed in the `Gmsh` software to obtain 3D tetrahedral volume meshes using the Netgen algorithm [85]. The organs and soft tissues were combined into a single model based on male thoracic anatomy. After defining the material properties and boundary conditions, the simulations were carried out using open-source `Code Aster` software [86]. The results were then analyzed using ParaView for post-processing analysis.

2.2 Geometry

2.2.1 The geometry of the base model

To study the effects of thoracic dimensions, we initially created a base model using a row model sourced from the BodyParts3D database.Henceforth, this model will be referred to as the "base model" throughout the study. Subsequently, we generated 215 additional models by individually stretching or compressing the base model along the three spatial axes (X, Y, Z). This approach allowed us to explore

the effects of varying thoracic dimensions on the study. The geometry of the base model, illustrated in Fig. 2.1A and 2.1B, includes the sternum, costal cartilages, ribs, and intercostal muscles. The intercostal muscles are depicted in red, while the breastbone and bony ribs are represented in dark gray. The vertebral column is displayed in dark yellow, and the cartilages are indicated by a lighter shade of gray. To apply the compression force, a small patch on the outer surface of the breastbone was selected (labeled as P1 in Fig. 2.1C), covering an area of approximately 10 cm^2. The location of the compression area (P1) is indicated in Figure 1C as a ratio of the breastbone length. The vertebral column is subjected to fixed boundary conditions.

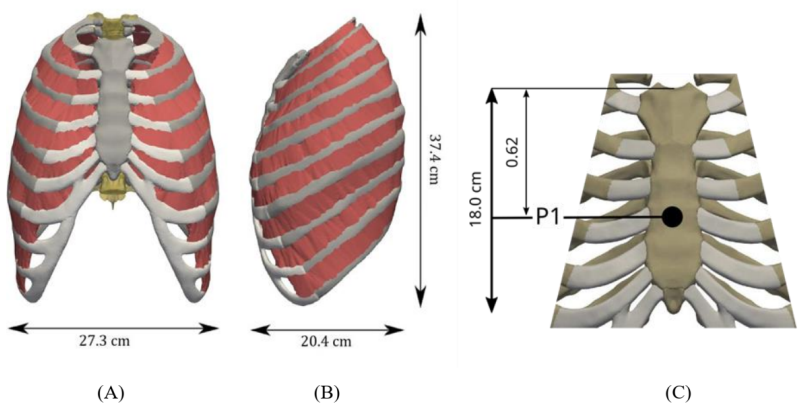

Figure 2.1: The geometry model used in the present study: (A) Frontal view of the rib cage; (B) Sagittal view; (C) Magnified view of the region around the breastbone in part (A)

2.2.2 Dimensions of the base model

Table 2.1 presents the key characteristics of the geometry model utilized as the base model. Additionally, the values of other commonly referenced geometric

parameters from the literature [87, 88] are provided in this table.

The antero-posterior diameter (D_{AP}) and transverse diameter (D_{AP}) of the ribcage were measured as depicted in Fig. 2.2. The Haller index (HI) is a simple and quantitative measure used in describing the shape of the thorax. As illustrated in Fig. 2.2, the HI is calculated by dividing the transverse diameter of the chest by the anteroposterior diameter. The height of the horizontal slice for measurement was selected at the axial location where the fifth rib joints the breastbone, as shown in Fig. 2.2B [87, 88]. The rib angle (θ) in relation to the vertical axis was measured at the height of the ninth rib. The selected ranges for rib cage width, depth, and height were based on existing experimental data found in the literature [89, 90].

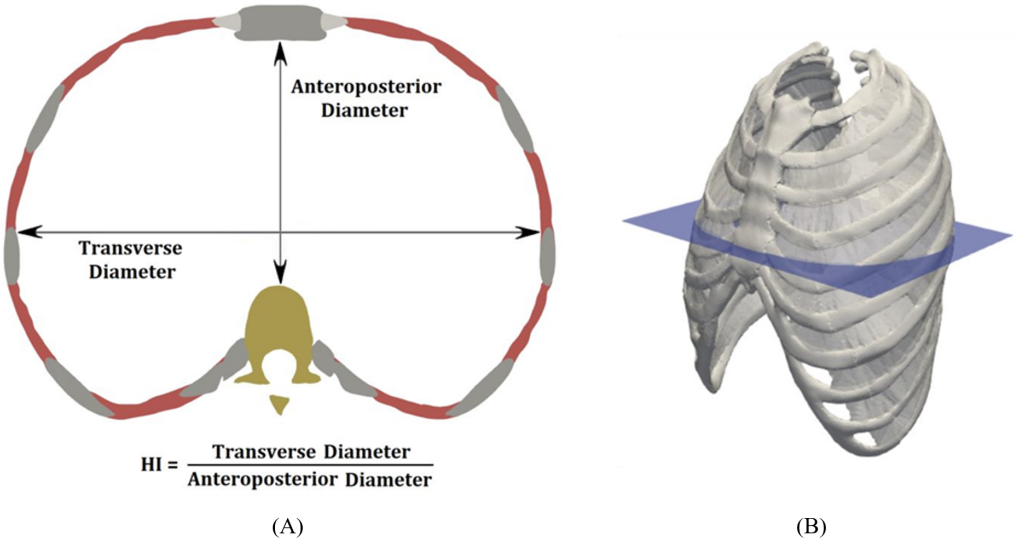

Figure 2.2: Sketch illustrating the determination of the antero-posterior (D_{AP}) and transverse (D_T) diameters used in the computation of the Haller Index [87, 88]

Table 2.1: Base geometry model dimensions and investigated geometrical parameters range in simulations

Parameter	Value	Range investigated
Rib cage width, W_R (cm)	27.3	22.9 - 28.4
Rib cage depth, L_R (cm)	20.4	15.5 - 21.4
Rib cage height, H_R (cm)	37.4	31.4 - 38.9
Transverse diameter, D_T (cm)	25.0	21.0 - 26.0
Antero-posterior diameter, D_{AP} (cm)	11.7	8.9 - 12.3
Haller index, HI (see Fig. 2A)	2.13	1.70 - 2.91
Rib angle, θ (degrees)	50.9	56.9 - 41.9
Rib cage volume, V (dm^3) = $W_R \times L_R \times H_R$	20.8	11.1 - 23.7
Horizontal (axial) cross-section area A_{XY} (cm^2) = $W_R \times L_R$	556.9	355.5 - 608.1
Frontal (X-Z) cross-section area A_{XZ} (cm^2) = $W_R \times H_R$	1021.0	720.4 - 1104.3
Sagittal (Y-Z) cross-section area A_{yz} (cm^2) = $D_{AP} \times H_R$	763.0	487.1 - 833.2

2.2.3 Dimensions of other models used in study 1

In the third row of Table 2.1, the investigated range of dimensional parameters is presented. These ranges were selected based on data available in the literature [87, 88] regarding the anteroposterior diameter, transverse diameter, and ribcage height. By comparing this information with the dimensions of the base model, it was determined that the range of ribcage dimensions reported in the literature can be achieved by applying three ranges of ratios, which are referred to as "ratios of stretching/shortening" in this study. Specifically, for the x-direction, the ratio (δX) ranges from 0.84 to 1.04; for the y-direction, the ratio (δY) ranges from 0.76 to 1.05; and for the z-direction, the ratio (δZ) ranges from 0.84 to 1.04. Six ratios were selected for each direction within these ranges. These final ratios, along with the resulting values of rib cage width (W_R), rib cage depth (L_R), and rib cage height (H_R), are presented in Table 2.2 for clarity. They were used to generate a total of 216 geometries (6x6x6) for studying the effects of ribcage dimensional parameters. It should be noted that the proportions of the median individual would correspond to δX = 0.94 (94%), δY = 0.905 (90.5%), and δZ = 0.94 (94%).

2.2.4 The geometry of the comprehensive model

Fig. 2.3A shows a general view of the geometry model used for the simulations in study 2. Different parts of the model are shown in Fig. 2.3B-D. The base model in study 1 was enhanced with the additional new organs, namely the lung and the heart, including all its chambers, sections of the aortic and pulmonary artery, and superior and inferior vena cava. A generic soft tissue was assigned to the

Table 2.2: Ratios of stretching/shortening applied along the X (δX), Y (δY), and Z (δZ) directions

δX	%	Rib cage Width (cm)	δY	%	Rib cage Depth (cm)	δZ	%	Rib cage Height (cm)
0.84	84	22.9	0.76	76	15.5	0.84	84	31.89
0.88	88	24.0	0.82	82	16.7	0.88	88	33.41
0.92	92	25.1	0.88	88	18.8	0.92	92	34.93
0.96	96	26.2	0.94	94	19.6	0.96	96	36.45
1	100	27.3	1	100	20.4	1	100	37.97
1.04	104	28.4	1.05	105	21.2	1.04	104	39.49

remaining void space in the thorax to account as well for the effect of internal organs not specifically included in the model. It is important to note that the skin surrounds all of these organs and provides an outer boundary for the geometry. As can be seen in Fig. 2.3C, the model of the heart comprises different elements, namely, the myocardium muscle, the right and left atria, and the right and left ventricles. Differentiating the parts of the heart means that we can calculate the volume of each part separately. Like the base model, the additional parts were derived from three-dimensional surface meshes available in the 3D Body Parts database for anatomy [83].

Two different heart models were employed with varying total volumes to investigate how heart volume impacts CPR outcomes. The total heart volume in model B (0.707 liters) is 10 % larger than the total heart volume in model A (0.643 liters). Notably, a clinical study encompassing several post-mortem cases reported a range of heart volumes between 0.342-1.495 liters, with a median value of 0.770

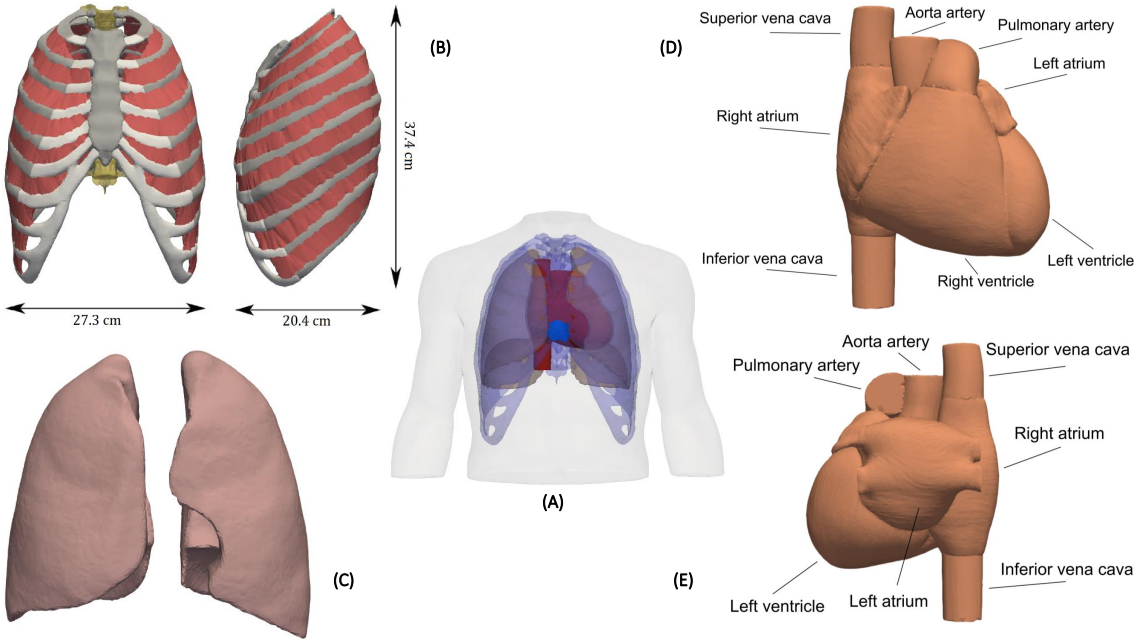

Figure 2.3: Geometry model; (A) General view; (B) Rib cage consisting of the breastbone, ten pairs of osseous ribs with nine sections of intercostal muscles, and seven pairs of costal cartilages; (C) Frontal view of the lungs in model A; (D, E) Frontal and rear view of the heart in the geometry model A

liters [91]. It is worth mentioning that the heart models used in the present study closely align with the median value observed in the clinical study. Additionally, the myocardial wall in model B is thicker than in model A. Table 3 presents the initial volumes for all heart chambers and lungs. These values are in line with the findings reported in clinical studies [92]. The third row of the table shows the percentage difference in initial volumes between model B and model A. The force was applied to a specific area of the skin located above the sternum, which is illustrated in Figure 1a with blue color. The volume of the heart denotes the region surrounded by the myocardium, whereas the volume of blood is measured as the sum of the volumes enclosed by the two atria and the two ventricles.

Table 2.3: Initial volumes of heart chambers and lung for both models. The third row represents the numerical value of the difference between model smaller heart and model with larger heart.

Heart model	Heart	Left Ventricle	Left Atrium	Right Ventricle	Right Atrium	Miocardium	Left Lung	Right Lung
Volume of model A (cm^3)	643	97	49	114	84	299	1141	1382
Volume of model B (cm^3)	707	99	53	117	85	353	1114	1356
Δ Vol (%)	10.0	1.9	8.4	2.5	0.67	18.4	-2.4	-1.9

2.3 Mesh Generation

To produce three-dimensional tetrahedral meshes, the individual surface meshes defining the boundary of each organ were imported into the `Gmsh` software [85]. The refined geometry model was then discretized to create a computational mesh. In study 1, the final meshes were made up of 1,006,571 nodes, 1,235,972 triangles, and 4,388,675 linear tetrahedral elements. For study 2, the complete computational mesh of model A consisted of 565,437 nodes, 166,188 triangular elements, and 3,235,399 tetrahedral elements. The computational mesh of model B included 543,522 nodes, 172,243 triangular elements, and 3,103,616 tetrahedral elements.

2.4 Constitutive material models

This section begins by introducing the fundamental principles and governing equations of the constitutive material models employed in this study[1]. Two types of material models have been utilized: the "isotropic linear elastic" model and the "von Mises elastoplastic model with linear isotropic hardening." Subsequently, the material properties employed in this research will be described.

2.4.1 Constitutive equations for isotropic linear elastic model

For uniaxial loading, Hooke's law can be given as follows:

$$\sigma \sim \varepsilon, \quad \sigma = E\varepsilon. \tag{2.1}$$

The proportional factor E is known as the elasticity modulus or Young's modulus. It is a material parameter that tells how much material is going to deform under tension and compression. σ represents axial stress, and ε is the strain produced due to this axial stress.

The generalized form Hooke's law for the three-dimensional case is given as:

$$\sigma_{ij} = C_{ijkl}\varepsilon_{kl}. \tag{2.2}$$

[1]The comprehensive details of all the equations in sections 2.4.1 and 2.4.2 can be found in the reference [93].

Here, σ_{ij} and ε_{kl} are the second-order stress and strain tensors, respectively. C_{ijkl} is the elastic stiffness of the material. It is a fourth-order tensor with 81 components. By inverting Equation (2.2), the relationship between strain and stress can be expressed as:

$$\varepsilon_{ij} = S_{ijk\ell}\sigma_{k\ell}. \tag{2.3}$$

Here, S_{ijkl} is known as the compliance tensor. Computation of a matrix C_{ijkl} with 81 components is a bit time-consuming process. Using the symmetrical property of the stiffness matrix C_{ijkl}, Equation (2.2) can be written as follows:

$$\begin{pmatrix} \sigma_{11} \\ \sigma_{22} \\ \sigma_{33} \\ \sigma_{23} \\ \sigma_{31} \\ \sigma_{12} \end{pmatrix} = \begin{pmatrix} C_{11} & C_{12} & C_{13} & C_{14} & C_{15} & C_{16} \\ & C_{22} & C_{23} & C_{24} & C_{25} & C_{26} \\ & & C_{33} & C_{34} & C_{35} & C_{36} \\ & & & C_{44} & C_{45} & C_{46} \\ & & & & C_{55} & C_{56} \\ \text{sym.} & & & & & C_{66} \end{pmatrix} \begin{pmatrix} \varepsilon_{11} \\ \varepsilon_{22} \\ \varepsilon_{33} \\ 2\varepsilon_{23} \\ 2\varepsilon_{13} \\ 2\varepsilon_{12} \end{pmatrix}. \tag{2.4}$$

Here, the stiffness matrix C_{ijkl} has 21 independent components.

An isotropic linear elastic material is a type of linear elastic material that possesses no characteristic orientation. When subjected to a uniaxial tensile test, the stress-strain curve of an isotropic linear elastic material remains the same regardless of the specimen's orientation within the material. In other words, the mechanical properties of the material, including the stress-strain relationship, are independent of the specimen's orientation relative to the material. For Isotropic materials, the matrix form of Equation (2.4) can be written as:

$$\begin{pmatrix} \varepsilon_{11} \\ \varepsilon_{22} \\ \varepsilon_{33} \\ 2\varepsilon_{23} \\ 2\varepsilon_{13} \\ 2\varepsilon_{12} \end{pmatrix} = \frac{1}{E} \begin{pmatrix} 1 & -\nu & -\nu & 0 & 0 & 0 \\ & 1 & -\nu & 0 & 0 & 0 \\ & & 1 & 0 & 0 & 0 \\ & & & 2(1+\nu) & 0 & 0 \\ & & & & 2(1+\nu) & 0 \\ \text{sym.} & & & & & 2(1+\nu) \end{pmatrix} \begin{pmatrix} \sigma_{11} \\ \sigma_{22} \\ \sigma_{33} \\ \sigma_{23} \\ \sigma_{13} \\ \sigma_{12} \end{pmatrix}. \quad (2.5)$$

Here, ν is the Poisson's ratio and represents the ratio of lateral or transverse strain to longitudinal or axial strain in a material. The theory of classical elasticity predicts that the value of Poisson's ratio for an isotropic material lies between -1 and 0.5. However, experiments have shown that the actual value of ν lies between 0.2 and 0.5 [94].

2.4.2 Constitutive equations for von Mises elastoplastic model with linear isotropic hardening

The field of elasto-plasticity falls within the realm of mechanics, focusing on the analysis of materials that initially experience elastic deformation. However, once they surpass a specific threshold, known as the initial yield stress σ_{Y0}, these materials exhibit permanent (irreversible) deformation. The objective of this section is to provide a concise overview of time-independent plasticity theory and establish the constitutive equations.

Stress-strain relationship

If the load applied on a material body is small than the elastic limit, then the strain occurring due to the force applied per unit area is directly proportional to the applied stress. If the applied load reaches the elastic limit or the yield point of the material, then the stress-strain curve shows nonlinear behavior. Therefore, the application of Hooke's law is not valid beyond this elastic limit. In other words, the material starts yielding or begins to flow.

Applying excessive force beyond the point of initial yielding leads to permanent deformation. This phenomenon, known as plasticity, describes the behavior of the material. To calculate the plastic strain, the total strain can be divided into two components: the reversible elastic strain ε_{ij}^{e} and the irreversible plastic strain ε_{ij}^{p} (refer to Fig. 2.4). Mathematically, the decomposition of strain can be expressed as:

$$\varepsilon_{ij} = \varepsilon_{ij}^{e} + \varepsilon_{ij}^{p}. \tag{2.6}$$

The macroscopic continuum approach generally uses incremental strain or strain rate. The strain rate approach is used in plasticity because deformation is path dependent. Therefore, the incremental form of Equation (2.6) can be expressed as.

$$\dot{\varepsilon}_{ij}^{e} = \dot{\varepsilon}_{ij} - \dot{\varepsilon}_{ij}^{p}. \tag{2.7}$$

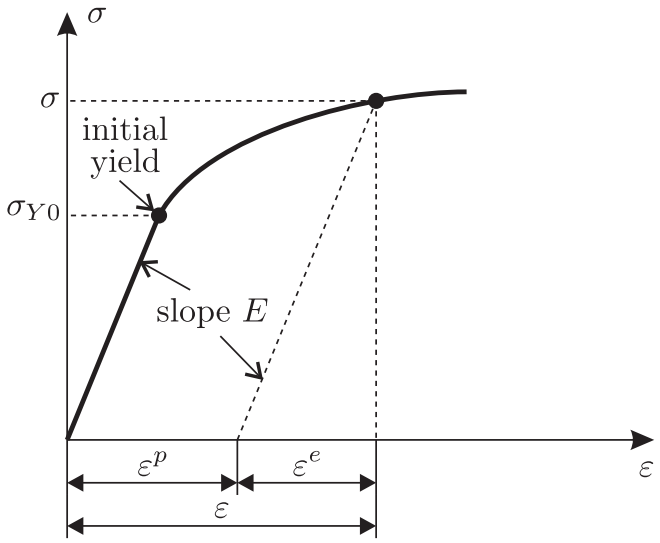

Figure 2.4: Elasto-plastic stress-strain curve for a uniaxial loading, with the initial yield stress and strain decomposition [95].

Unloading processes deviate from obeying Hooke's law, as stated in Equation (2.2), when the material experiences plastic flow. To accommodate this deviation, Hooke's law needs to be modified. The modification involves substituting Equation (2.7) into Equation (2.2), yielding the incremental form of Hooke's law:

$$\dot{\sigma}_{ij} = C_{ijkl}(\dot{\varepsilon}_i j - \dot{\varepsilon}^p_{ij}). \tag{2.8}$$

The Yield Criterion

In an elasto-plastic model, the total strain can be decomposed into elastic strain ε^e_{ij} and plastic strain ε^p_{ij}. The elastic strain components can be determined using Hooke's law. To determine the plastic strain, we need to consider two important

concepts: yield conditions and the flow rule. The yield criterion (condition) is used to determine the transition of a material's behavior from elastic to plastic. In other words, it defines the stress state for which the material shows plastic behavior. For a uniaxial stress test, the yield condition is easy to determine. In the uniaxial yield condition, if the stress σ is smaller than the initial yield stress σ_{Y0}, then the material exhibits elastic behavior; otherwise, it exhibits plastic behavior. In a multiaxial stress state, finding the yield condition is not that straightforward. In this case, the yield criterion is defined by a scalar function known as the yield function [96]:

$$f(\sigma_{ij}) = 0 \tag{2.9}$$

Here, σ_{ij} is a symmetrical stress tensor. Therefore, Eq. (4.8) can be written in the following form:

$$f(\sigma_{11}, \sigma_{22}, \sigma_{33}, \sigma_{23}, \sigma_{31}, \sigma_{12}) = 0 \tag{2.10}$$

If the yield function is equal to zero, $f(\sigma_{ij}) = 0$, then the material shows plastic behavior, and when $f(\sigma_{ij}) < 0$, then the material exhibits elastic behavior.

If the material is considered to be isotropic, then the yield condition is independent of the orientation of the coordinate system. It means that the expression in Equation (2.9) can be expressed in terms of the invariants of the stress tensor [97]:

$$f(J_1, J_2, J_3) = 0 \tag{2.11}$$

Here, J_1, J_2, and J_3 are the first, second, and third invariants of the stress tensor, respectively. These are defined by the following relations:

$$\begin{aligned} J_1 &= \sigma_{11} + \sigma_{22} + \sigma_{33}, \\ J_2 &= -(\sigma_{11}\sigma_{22} + \sigma_{22}\sigma_{33} + \sigma_{33}\sigma_{11}), \\ J_3 &= \sigma_{11}\sigma_{22}\sigma_{33}. \end{aligned} \tag{2.12}$$

Here, σ_{11}, σ_{22}, and σ_{33} are the principal components of the stress tensor.

There exist many different yield criteria. In this study, we have used the von Mises yield criterion which is widely used in engineering applications, mainly for computational analysis. The von Mises yield criterion considers all three principal shear stresses to predict the yielding stress.

Von Mises Yield Criterion

The Von Mises yield criterion states that materials start yielding when the second deviatoric stress invariant, J_2, reaches a critical value. Mathematically, the Von Mises yield criterion is expressed as:

$$J_2 = k^2 \tag{2.13}$$

Here, k is a material parameter that represents the yield stress of the material under simple shear. The value of k is $\sqrt{3}$ times smaller than the tensile yield stress

in the case of simple tension. It can be expressed as:

$$k = \frac{\sigma_Y}{\sqrt{3}} \tag{2.14}$$

Alternatively, the Von Mises yield criterion can be expressed using the Von Mises equivalent stress σ_{Mises}:

$$\sigma_{\text{Mises}} = \sigma_Y = \sqrt{3J_2} \tag{2.15}$$

The Von Mises equivalent stress predicts the yielding of a material under multiaxial loading. To express Equation (2.15) in terms of the deviatoric stress, let us define the second deviatoric stress invariant J_2 in an alternative form:

$$J_2 = \frac{1}{2} s_{ij} s_{ij} \tag{2.16}$$

Here, s_{ij} is the deviatoric stress tensor, which is defined as the difference between the stress tensor σ_{ij} and the hydrostatic stress tensor $p\delta_{ij}$. The hydrostatic stress tensor can be obtained by taking the average of the three normal stress components of any stress tensor. Therefore, the deviatoric stress tensor s_{ij} can be expressed as:

$$s_{ij} = \sigma_{ij} - p\delta_{ij} = \sigma_{ij} - \frac{1}{3}\sigma_{kk}\delta_{ij} \tag{2.17}$$

Substituting Equation (2.17) into Equation (2.16) gives us J_2, which we can substitute into Equation (2.15) to obtain the Von Mises equivalent stress in terms

of the deviatoric stress tensor:

$$\sigma_{\text{Mises}} = \sqrt{\frac{3}{2} s_{ij} s_{ij}} \tag{2.18}$$

The Von Mises yield criterion as a flow function can be written as:

$$f(\sigma_{ij}, \sigma_Y) = \sqrt{\frac{3}{2} s_{ij} s_{ij}} - \sigma_Y \tag{2.19}$$

Here, σ_Y is the current yield stress.

Flow Rule

The flow rule establishes a relationship between stress and plastic strain under multi-axial loading and defines the direction of plastic flow. In other words, we can say that the derivative of plastic potential g, which is a function of stress, with respect to stress is proportional to the plastic strain. Mathematically we can write this as follows:

$$d\varepsilon_{ij}^{p} = d\lambda \frac{\partial g}{\partial \sigma_{ij}} \tag{2.20}$$

The referred form is recognized as the non-associated flow rule. For the materials examined in this study, we specifically focus on those for which the plastic potential can be equated to the yield function, denoted as $g = f$. By substituting f instead of g in Equation (2.20), we obtain an alternative form of the flow rule

termed the associated flow rule.

$$d\varepsilon_{ij}^{p} = d\lambda \frac{\partial f}{\partial \sigma_{ij}} \quad or \quad \dot{\varepsilon}_{ij}^{p} = \dot{\lambda} \frac{\partial f}{\partial \sigma_{ij}} \tag{2.21}$$

Here, $\dot{\lambda}$ is a non-negative hardening parameter that determines the magnitude of the plastic strain. The direction of the plastic strain increment is given by the term $\frac{\partial f}{\partial \sigma_{ij}}$,which is normal to the yield surface. This is why the associated flow rule is also known as the normality hypothesis of plasticity.

After applying the associated flow rule to the Von Mises yield condition and performing some subsequent calculations, we obtain the partial derivative of the yield function f with respect to the stress tensor σ_{ij}. This derivative is equal to the deviatoric stress tensor s_{ij}, expressed as:

$$\frac{\partial f}{\partial \sigma_{ij}} = s_{ij} \tag{2.22}$$

Substituting Equation (2.22) into Equation (2.21) gives us the associated flow rule in terms of the deviatoric stress tensor:

$$\dot{\varepsilon}_{ij}^{p} = \dot{\lambda} s_{ij} \tag{2.23}$$

Consistency Condition

The condition that the stress should remain on the yield surface, which is the graphical representation of the yield function $f(\sigma_{ij})$, during plastic flow is known

as the consistency condition.

To visualize this concept, let's consider a material to which we apply an external load. Initially, the material deforms elastically, and after reaching its yield point, it starts showing plastic behavior. If we assume that the material shows plastic behavior with no hardening, then the material will deform further plastically under constant stress, i.e., the load point remains on the yield surface (see Fig. 2.5). Mathematically, this means that the yield function f remains equal to zero (as shown in Fig. 2.5), and as a result, the time derivative of f will vanish:

$$\dot{f} = 0 \tag{2.24}$$

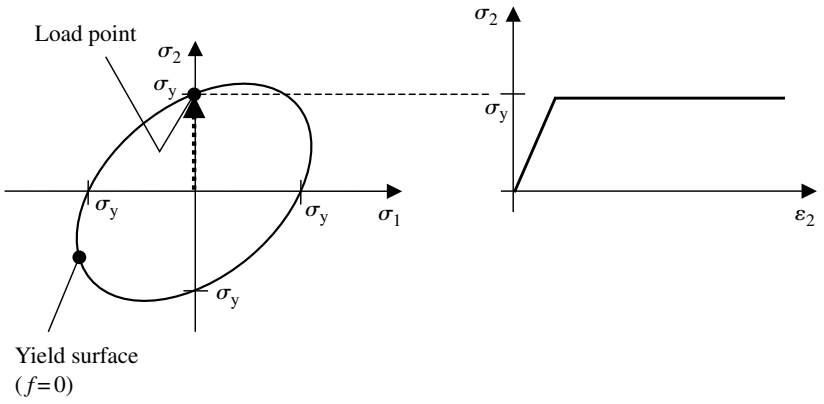

Figure 2.5: Graphical representation of the Von Mises yield surface for plane stress and the corresponding stress-strain curve [98].

The above equation is only valid for plastic yielding and cannot be applied during elastic deformation. The consistency condition is useful for computing the plastic multiplier.

Using Von Mises tield criterion, the following expression for the consistency condition is calculable:

$$\dot{f}(\sigma, \sigma_Y) = s_{ij}\dot{\sigma}_{ij} - \frac{2}{3}\sigma_Y\dot{\sigma}_Y = 0 \tag{2.25}$$

Isotropic Hardening

Hardening refers to the increase in yield stress during plastic deformation. In this study, we used a type of hardening named isotropic hardening. Isotropic hardening is a hardening process where the yield strength or expansion in the yield surface is uniform in all directions (see Fig. 2.6). For uniaxial loading, the isotropic hardening law, which is linear in nature, is given by:

$$\sigma_Y = \sigma_{Y0} + H\varepsilon_{p11}. \tag{2.26}$$

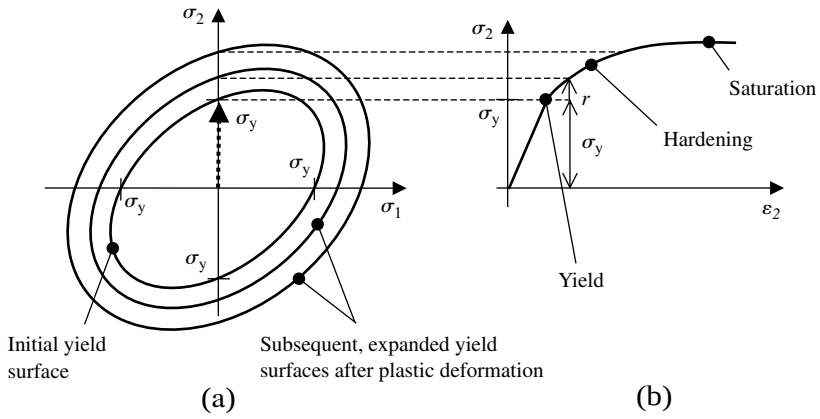

Figure 2.6: Isotropic Hardening: (a): Uniform expansion of the yield surface in stress space with plastic deformation. (b): Stress (σ) strain (ε) curve, representing increase in the yield strength due to strain hardening [98].

Here, H is known as the plastic modulus, which is defined as the slope of the nonlinear part of the stress-strain curve obtained through uniaxial tensile testing. ε_{p11} represents the plastic part of the normal strain, ε_{11}. Whether the material exhibits true hardening, perfect plasticity, or softening depends on the value of the plastic modulus. If the plastic modulus is positive, the yield stress increases. If $H = 0$, it corresponds to perfect plasticity, while a negative value of the plastic modulus indicates softening behavior.

For isotropic materials, the incremental stress tensor is calculable form Equation (2.27) which is known as the Prandtl-Reuss equations for the isotropic materials.

$$\dot{\sigma}_{ij} = \lambda \dot{\varepsilon}_{rr} \delta_{ij} + 2\mu \dot{\varepsilon}_{ij} - \frac{3\mu s_{ij} s_{kl}}{1 + \frac{H}{3\mu}\sigma_Y^2} \dot{\varepsilon}_{kl}. \tag{2.27}$$

Here, λ and μ are scalar quantities, known as Lamé constants and are calculated as follows:

$$\lambda = \frac{E\nu}{(1+\nu)(1-2\nu)}, \quad \mu = G = \frac{E}{2(1+\nu)}. \tag{2.28}$$

Here, (G) is the shear modulus, also known as the modulus of rigidity or elastic modulus in shear, which is a material property that measures the resistance of a material to shear deformation. It quantifies how the material responds when subjected to forces parallel to its surface or when different layers within the material slide past each other.

We can consider Equation (2.30) for two different cases: first for elastic behavior, i.e., $f < 0$, and second for plastic behavior, i.e., $f = 0$:

$$\dot{\sigma}_{ij} = \begin{cases} \lambda \dot{\varepsilon}_{rr} \delta_{ij} + 2\mu \dot{\varepsilon}_{ij} & \text{for } f < 0 \\ \lambda \dot{\varepsilon}_{rr} \delta_{ij} + 2\mu \dot{\varepsilon}_{ij} - \frac{3\mu s_{ij} s_{kl}}{1 + \frac{H}{3\mu} \sigma_Y^2} \dot{\varepsilon}_{kl} & \text{for } f = 0 \end{cases} \tag{2.29}$$

An alternative way to express the Prandtl-Reuss equations for isotropic materials using E and ν is:

$$\dot{\sigma}_{ij} = \frac{E}{1+\nu} \left(\dot{\varepsilon}_{ij} + \frac{\nu}{1-2\nu} \dot{\varepsilon}_{rr} \delta_{ij} - \frac{3}{2} \frac{3E}{3E + 2H(1+\nu)} \frac{s_{ij} s_{kl}}{\sigma_Y^2} \dot{\varepsilon}_{kl} \right). \tag{2.30}$$

2.4.3 Material properties in study 1

The costal cartilages are specifically modeled as materials with linear isotropic elastic behavior. The Young's modulus of cartilage (E_c) is known to be influenced by its degree of calcification, which typically increases with age, and can be described by a mathematical relationship proposed by Forman [99] based on McCormick's calcification score (CS) [100]. In this study, a CS value of 1.5 is assumed for the costal cartilages, resulting in an Ec value of 27 MPa according to Forman's formula. Suazo et al. [54] showed that using this E_c value, along with a Poisson's ratio (η_c) of 0.45 for the cartilage, the linear elastic model provided results in good agreement with the experimental test results obtained by Forman and Kent [101].

It's worth noting that osseous tissues are known to exhibit anisotropic mechanical properties, meaning that their mechanical behavior depends to some extent

on the direction of applied forces. Some recent works [102–104] show how to systematically evaluate a map of the bone anisotropic directions from micro-CT scans, provided a high enough image resolution (a few tens of a μm). However, because of the high-radiation levels involved, micro-CT scans of an adult ribcage can only be obtained postmortem [105]. Therefore, in this study, a simplified homogeneous model is used to characterize the mechanical response of ribs and breastbone, assuming von Mises elastoplastic behavior with linear isotropic hardening [106]. Elastoplasticity is an intermediate behavior between purely elastic (spring-like) and purely plastic (fluid-like) models [107]. The bone tissue is considered to exhibit elastic-like deformation when the stress is within the tensile yield strength limit (σ_Y), and elastoplastic deformation occurs when the stress exceeds the yield limit. Plastic deformation of the bone tissue leads to a reduction in stiffness modulus (E_T) compared to the initial elastic modulus (E_b). It's important to note that in elastoplastic deformation, only part of the total stress work is recoverable as elastic-like energy, while the rest is irrecoverable, resulting in permanent shape change [107]. In this study, the elastoplastic model for bone tissue is characterized by parameter values of E_b = 7 GPa, η_b = 0.45, σ_Y = 30 MPa, and E_T = 2 GPa, which have been shown to produce good simulations of rib bending experiments in previous studies [54, 108].

In this study, the costo-vertebral joints are modeled based on the approach introduced by Suazo et al. [54], where they are represented as capsule-like volumes of a softer material attached to the rear tip of the ribs. The material properties of the capsule are assumed to exhibit elastic behavior, with a Young modulus (E_j) of 1 MPa and a Poisson ratio (η_j) of 0.45. The intercostal muscles tissue, on the other hand, is modeled as a linear isotropic elastic solid with a Young modulus (E_m) of

Table 2.4: Linear Elastic Model Parameters for Various Tissues in the Present Study. Notably, the Elastoplastic Model for Osseous Tissue Includes Two Additional Parameters: Tensile Yield Strength (σ_Y = 30 MPa) and Tangent Modulus (E_Y = 2000 MPa)

Tissue	Young modulus (MPa)	Poisson Ratio
Costal cartilages	27	0.45
Breastbone, osseous ribs(elastic component)	7000	0.45
Costo-vertebral joints (capsule)	1	0.45
Intercostal muscles	2	0.49

2 MPa and a Poisson ratio (η_m) of 0.49.

As outlined in the study by Suazo et al., the chosen value of E_m in the present analysis is intentionally set higher than the value proposed by Kindig et al. [80] (E_m = 1.03 MPa). The purpose of increasing the E_m value is to include the additional stiffness that would be provided by internal tissues and viscera, which are not included in the current geometry model.

2.4.4 Material properties in study 2

Table 2.5 presents the parameter values of material properties in this study 2. In this study, the same material used for the models in study 1 was utilized, except for the osseous parts and intercostal muscles. In this study, values of E_b, σ_Y, and E_T are notably lower than those employed in study 1. The rib cage model in study 1 had to provide the entire chest resistance to compression in the absence of other internal organs and soft tissues. In other words, the previous rib cage model was overly stiff, whereas the model in this study has been slightly softened.

Furthermore, the values of E_b, σ_Y, and E_T have been adjusted to ensure that the compression force used in the simulations aligns more closely with previous experimental data [40, 109]. Furthermore, it has been verified that accurate predictions for rib bending experiments conducted by Kindig et al. [108] are also obtained by the simulations, utilizing the current values of E_b, σ_Y, and E_T (results not included here for brevity). Similarly, the intercostal muscles in the present model have been softened, with the current Young's modulus (E_m) value of 0.5 MPa (four times smaller than in study 1; refer to Table 2.5).

Regarding the mechanical properties of soft tissues in the human body, the elastic moduli reported in scientific literature exhibit a wide range of values. Adipose tissue and internal organs such as lungs, liver, pancreas, and thymus generally have elastic moduli in the range of $1\,\text{kPa} \leq E \leq 10\,\text{kPa}$ [110, 111]. In this study, the lungs have been modeled with an elastic modulus (E) of 5.0 kPa and a Poisson's ratio (η) of 0.22 [111, 112]. For the generic soft tissue material, $E = 5.0\,\text{kPa}$ and a larger Poisson's ratio ($\eta = 0.4995$) have been assumed. This value, close to the incompressibility limit of $\eta = 0.5$, ensures that the soft tissue retains its volume in the simulations and enforces continuity at material boundaries.

The elastic modulus of adult human heart tissue varies considerably in literature, ranging from $E \approx 5\,\text{kPa}$ to $50\,\text{kPa}$ [113]. Notably, the cardiopulmonary resuscitation (CPR) mechanism aimed to simulate here aligns with the concept of passive heart muscle. This means that the myocardium tissue does not spontaneously activate during CPR (at least in the early stages) but responds to externally induced stress (mechanical squeezing). Consequently, $E = 30\,\text{kPa}$ for the

Table 2.5: Parameters used for material properties in the constitutive model

Organ	Constitutive Model	Parameter Values
Ribs and Sternum	Von Mises elasto-plastic with linear isotropic hardening	E= 4 GPa σ_Y = 25 MPa E_T = 1 GPa η = 0.4
Costal Cartilages	linear isotropic elastic	E = 27 MPa η = 0.45
Intercostal Muscles	linear isotropic elastic	E = 0.5 MPa η = 0.49
Lungs	linear isotropic elastic	E = 3.7 kPa η = 0.40
Myocardium Muscle	linear isotropic elastic	E = 30 kPa η = 0.45
Blood (in atria and ventricles)	linear isotropic elastic	E = 3 kPa η = 0.35
Major Blood Vessels	linear isotropic elastic	E = 3 kPa η = 0.499
Soft Tissue	linear isotropic elastic	E = 5 kPa η = 0.4995

myocardium tissue has been set in this study, a value within the assumed range for an adult heart in diastole [114].

Finally, Table 2.5 indicates that blood in study 2 is not modeled as a fluid but as a soft material with $E = 3\,\text{kPa}$ and $\eta = 0.35$. However, the sections of major blood vessels included in the model (inferior and superior vena cava, aorta, and pulmonary arteries) have been modeled with a higher Poisson's ratio ($\eta = 0.499$) to account for the increased rigidity contributed by the blood vessel walls and valves (not incorporated in the present model).

Chapter 3

Results

In this chapter, the results of the two studies previously discussed will be showcased. Initially, the results of study 1 will be presented, which aims to explore how chest dimensional parameters affect compression depth and induced stress in the ribcage. We utilize data obtained from the simulation to develop predictive equations for compression depth and ribcage maximum stress based on dimensional parameters. This chapter will provide the initial form of these equations, which will be further modified in the next chapter. Additionally, the following section will present the results of the simulation on the comprehensive models. This section will primarily investigate the deformation of internal organs, including the myocardium, various heart chambers, and the lungs for two thorax models with different sizes of heart.

3.1 Effects of chest dimensions on CPR outcome

Simulations were conducted on each of the 216 geometry models using 12 different compression force values ranging from F = 50 N to 600 N, with an incremental step of 50 N. The analysis of simulation results is divided into two subsections. The first subsection focuses on the compression depth achieved, while the second subsection discusses the stress levels experienced by the ribs due to the compression.

3.1.1 Compression depth as a function of the problem parameters

The relationship between compression depth and the dimensions of the rib cage is illustrated in Fig. 3.1 for a compression force of 600 N at location P1 (Fig. 2.1), denoted as ΔY_{P1}. In this three-dimensional scatter diagram, the dimensions of the rib cage are represented on each axis, showing the changes in rib cage dimensions in different directions. Each sphere corresponds to a specific geometry model, and the color of each sphere indicates the compression depth achieved in that particular model, with the corresponding ΔY_{P1} levels shown in a color box located adjacent to the graph. Fig. 3.1 reveals that increasing the depth or height of the rib cage has a negative impact on the compression depth, while increasing the width of the rib cage results in an increase in compression depth.

To quantify this relationship, a least squares fit was applied using the form

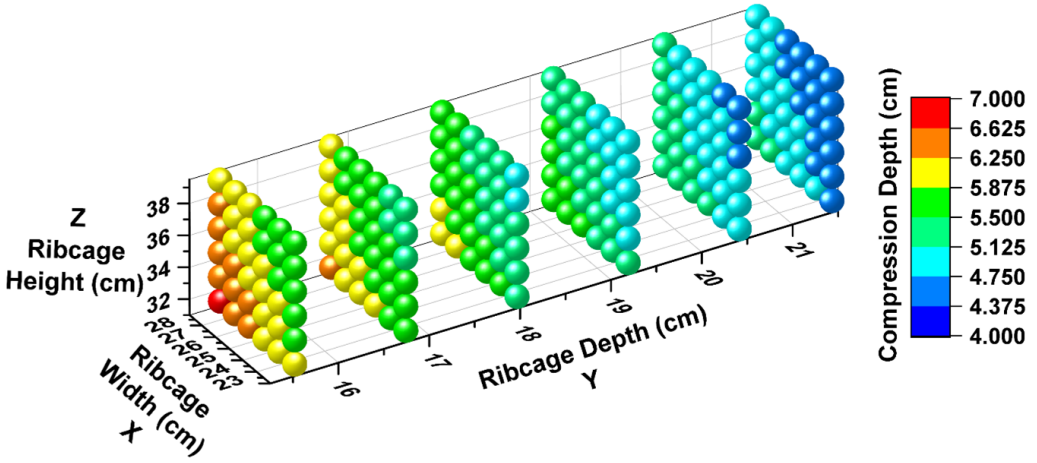

Figure 3.1: Three-dimensional scatter plot depicting the calculated compression depth at the P1 area for all the geometry models, with a compression force of F = 600 N

$\Delta Y = \Delta Y(F, \delta X, \delta Y, \delta Z)$, where ΔY represents the compression depth as a function of the applied force, F, ratios of stretching/shortening of ribcage width (δX), ribcage depth (δY) and ribcage height (δZ).

and F denotes the applied compression force. The functional form of products of powers was found to provide good fits for compression forces in the range of 450 N to 600 N.

$$\Delta Y = \mathrm{C}\mathrm{F}^{\alpha}\delta X^{\beta}\delta Y^{\gamma}\delta Z^{\varepsilon} \tag{3.1}$$

The constants C, α, β, γ, and ε for the fit were determined based on the compression depth values obtained from the 216 simulations. It is worth noting that the range of compression forces used in the simulations (450 N $\leq$ F $\leq$ 600 N) is commonly applied in real CPR procedures [40]. The resulting fit for the predicted

maximum compression depth at the compression location (ΔY_{P1}) is:

$$\begin{gathered}\Delta Y_{P1}(\text{ cm}) = 0.0398 F^{0.757} \delta X^{0.552} \delta Y^{-0.763} \delta Z^{-0.306} \pm 0.0370 \text{ cm}, \\ 450N \leq F \leq 600N\end{gathered} \tag{3.2}$$

Equation (3.2) corroborates the pattern seen in Fig. 3.1. It is worth noting that variation in rib cage depth has the most significant impact on ΔY_{P1}, as evidenced by the negative exponent of -0.763. Rib cage width has a positive exponent of 0.552, indicating that it has a moderate impact, while rib cage height has a lower exponent of -0.306, indicating that it has a weaker effect on ΔY_{P1}. Additionally, it is worth noting that the sum of the absolute negative exponents for δY and δZ is approximately twice as large as the exponent for δX. This implies that in a hypothetical scenario where the rib cage volume changes while maintaining fixed relative proportions in the X, Y, and Z-directions, a smaller rib cage volume would result in a larger compression depth achieved.

The predicted maximum compression depth at the location P2, which is approximately midway between P1 and the xiphoid process (as shown in Fig. 3.2), can be described by the following fit:

$$\begin{gathered}\Delta Y_{P2}(\text{ cm}) = 0.0538 F^{0.729} \delta X^{0.552} \delta Y^{-0.724} \delta Z^{-0.286} \pm 0.0471 \text{ cm}, \\ 450N \leq F \leq 600N\end{gathered} \tag{3.3}$$

It is noteworthy that the fit Equation (3.3) exhibits a similar qualitative behavior, in terms of the signs and proportions of the powers, as that of Equation (3.2) for the P1 compression location.

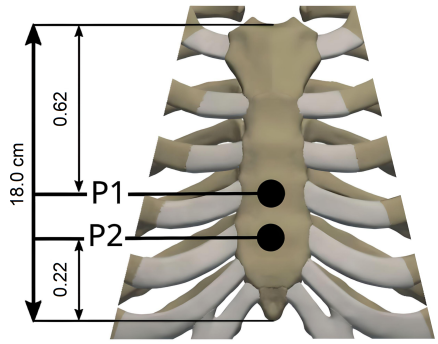

Figure 3.2: Approximate location of P1 and P2

The effectiveness of the fits in Equations (3.2) and 3.3, as evidenced by the low root mean square (rms) error values of 0.0370 cm and 0.0471 cm, respectively, is visually demonstrated in Fig. 3.3. In these plots, the fit results are compared with the corresponding values predicted by the FE simulation for each of the 216 geometry models, considering the four levels of compression force (F) included in the fit for each model. Furthermore, Fig. 3.3 illustrates that the compression depth achieved at location P2 is slightly higher (with an average difference of approximately 0.5 cm) compared to location P1, for a given geometry and compression force level. This phenomenon is attributed to the hinge mechanism concept [54, 115], which suggests that during CPR, the breastbone is, basically, superiorly fixed.

3.1.2 Maximum stress levels in ribs as a function of the problem parameters

In addition to the deformation caused by compression, the FE simulations performed in this study also allow the estimation of the stress distribution within the tissues. The von Mises stress criterion is a criterion method for investigating

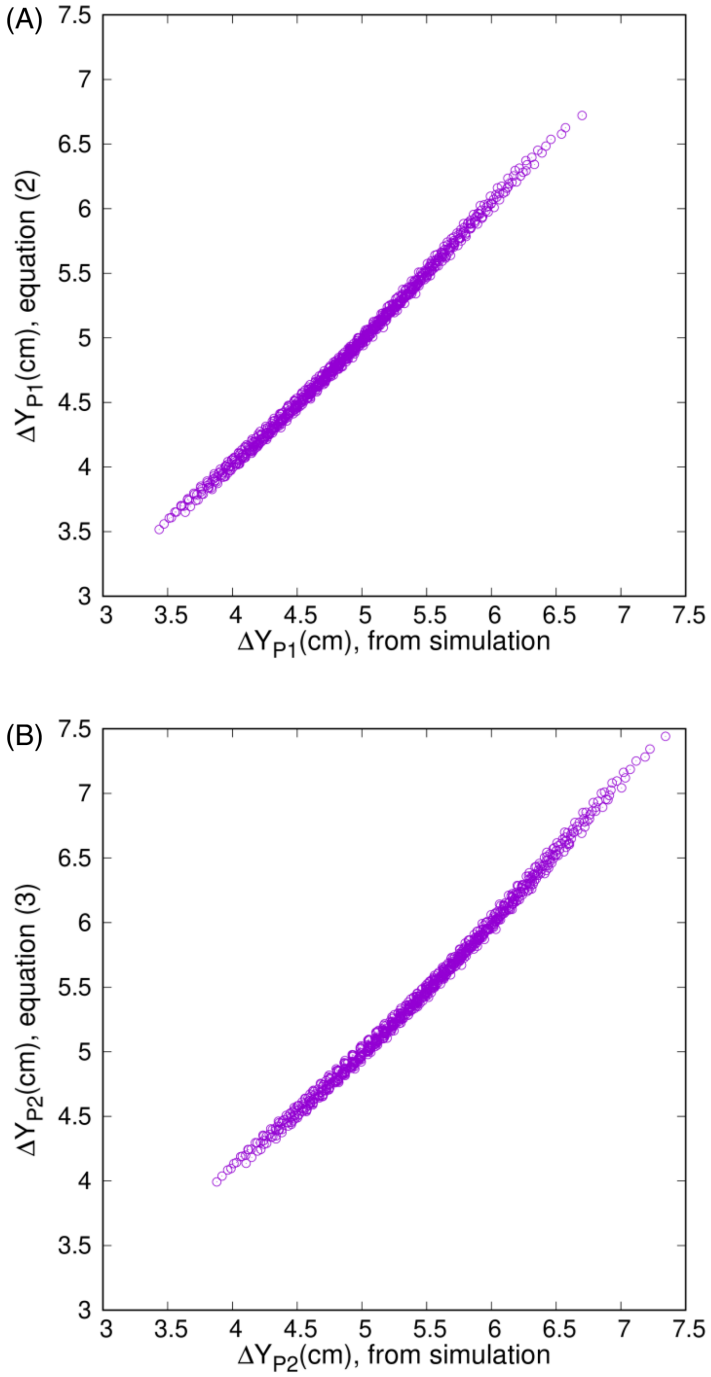

Figure 3.3: (A) Accuracy of the fits for the predicted compression depth (ΔY) measured at the compression area (P1, see Fig. 3.1). (B) Accuracy of the fits for the predicted compression depth (ΔY) measured at the alternative area P2 (located midway between P1 and the xiphoid process [54]

the maximum stress and the location of the fracture [116]. In the context of CPR simulations, the von Mises stress criterion can provide useful information on the location of possible fractures when isotropic material properties are assumed [26]. Therefore, the von Mises stress criterion is a reliable method for investigating the maximum stress and the location of the maximum stress in the simulations. In a previous work, Suazo et al. [54] reported that the calculated von Mises stress, denoted by σ_v, was particularly high in the third to sixth osseous ribs. Fig. 3.4 displays the predicted distributions of σ_v on the surface of the 3rd to 6th left ribs for three different geometries and a compression force of F=600 N. The figure displays both outer and inner views of the ribs, presented in the top and bottom rows, respectively.

The decrease in maximum stress levels on the ribs as the rib cage depth increases is demonstrated in Fig. 3.4. To evaluate the impact of changes in geometry on stress levels, we used a fit based on the FE results of the 216 geometry models. Equation 3.4 represents a fit in the form of power products assumed for each individual rib.

$$\sigma_v = \mathrm{AF(N)}^b \delta X^c \delta Y^d \delta Z^e \text{ MPa}, \; 450N \leq F \leq 600N \tag{3.4}$$

The values of the A, b, c, d, and e parameters obtained from the fits of Equation (3.4) for the 3rd to 6th left ribs are presented in Table 3.1.

It should be noted that, for a constant value of the applied compression force, F, the maximum stress levels on the ribs (σ_v) consistently decrease with larger rib cage dimensions, as evidenced by the negative values of the c, d, and e exponents

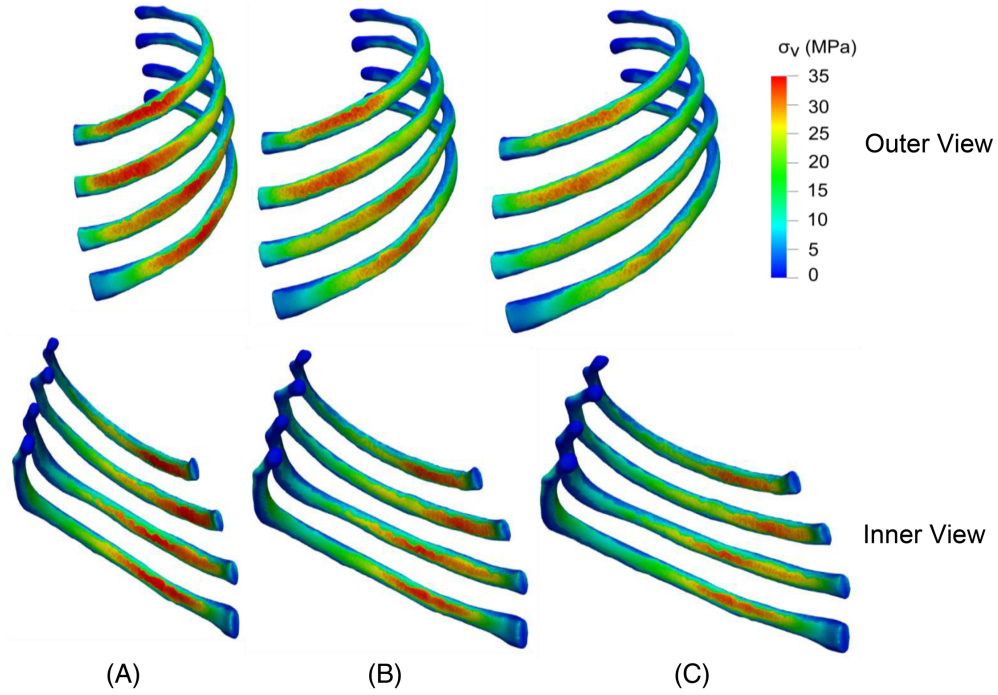

Figure 3.4: The von Mises stress (σ_v) distribution on the surface of the 3rd, 4th, 5th, and 6th left ribs for different geometry models with $\delta X \delta Y \delta Z$ = 1×0.76×1 (A), 1×0.94×1 (B), and 1×1.05×1 (C) when the compression force is F = 600 N

in Equation (3.4).

3.2 Results of the comprehensive model

Table 3.2 displays the detailed results for both models and all 12 force levels. The table presents different parameters that can be classified into three groups: ribcage parameters, heart parameters, and lung parameters.

The following 3D contours (Fig. 3.5 to Fig. 3.10) illustrate the results of model A

Table 3.1: Parameter values for the fits of Equation (3.4) corresponding to the 3rd, 4th, 5th, and 6th left ribs

Rib	A	b	c	d	e	rms (MPa)
3L	1.895	0.457	-0.113	-0.370	-0.445	0.370
4L	1.535	0.484	-0.310	-0.353	-0.331	0.368
5L	1.210	0.526	-0.348	-0.418	-0.311	0.439
6L	1.288	0.514	-0.285	-0.504	-0.267	0.338

for four different applied forces (300, 400, 500, and 600 Newton). To prevent repetition, only the 3D contour outcomes for model A are provided, given the significant resemblance between the results of the two models. Additionally, we have presented only the results for model A as it serves as the base model to maintain brevity. We will refer to the results of model B only when we require a comparison between the two models.

3.2.1 Ribcage deformation

Fig. 3.5 illustrates how the ribcage deforms when various forces are applied. Because of the fixed boundary condition, there is no deformation in the spine. The most prominent displacement in the chest occurs at the end of the sternum. The cartilages have lower stiffness compared to the ribs, resulting in greater deformation, which contributes to the increased displacement of the sternum.

Fig. 3.6 illustrates the relationship between compression force and compression depth. It is worth noting that for both geometry models, A and B, the achieved

Table 3.2: Detailed results for all applied force levels from both models and the variance between the two models; (a): The maximum displacement of the compression area; (b): The change in the whole heart volume, including myocardium and containing blood; (c): the change in the total blood volume that is included in all heart chambers; (d), (e), (f), (g): Changes in the volume of blood in individual parts of the heart; (h), (i): the change in the volume of the left and right lungs

Force Value (N)	Heart model	a		b		c		d		e		f		g		h		i		j	
		Compression Depth (cm)	Difference (%)	Heart volume change (%)	Difference (%)	Blood Volume Change (%)	Difference (%)	Left Ventricle Volume Change (%)	Difference (%)	Left Atrium Volume Change (%)	Difference (%)	Right Ventricle Volume Change (%)	Difference (%)	Right Atrium Volume Change (%)	Difference (%)	Left Lung Volume Change (%)	Difference (%)	Right Lung Volume Change (%)	Difference (%)	Overall Lungs Volume Change (%)	Difference (%)
50	A	0.58	-0.18	1.25	-4.8	2.23	1.38	1.6	0.81	2.22	2.86	3.16	2.45	1.71	-2.86	1.13	1.6	1.08	0.04	1.10	0.75
	B	0.58		1.19		2.26		1.61		2.29		3.23		1.66		1.15		1.08		1.11	
100	A	1.17	-0.19	2.64	-4.88	4.75	1.39	3.35	0.91	4.72	2.81	6.73	2.56	3.7	-3.02	2.36	1.55	2.25	0.03	2.30	0.73
	B	1.17		2.51		4.81		3.38		4.85		6.9		3.58		2.4		2.26		2.32	
150	A	1.76	-0.19	4.16	-4.96	7.55	1.41	5.26	1	7.51	2.77	10.68	2.67	5.97	-3.18	3.7	1.5	3.52	0.02	3.6	0.70
	B	1.75		3.95		7.65		5.31		7.72		10.97		5.78		3.75		3.53		3.63	
200	A	2.34	-0.20	5.81	-5.03	10.61	1.42	7.3	1.09	10.59	2.75	14.98	2.76	8.53	-3.33	5.12	1.44	4.89	0.03	4.99	0.68
	B	2.33		5.52		10.76		7.38		10.88		15.4		8.25		5.2		4.89		5.03	
250	A	2.91	-0.21	7.57	-5.08	13.91	1.44	9.46	1.18	13.94	2.75	19.59	2.85	11.35	-3.47	6.64	1.4	6.33	0.03	6.47	0.66
	B	2.90		7.19		14.11		9.57		14.33		20.15		10.95		6.73		6.33		6.51	
300	A	3.46	-0.16	9.45	-5.11	17.44	1.47	11.73	1.28	17.58	2.75	24.48	2.96	14.42	-3.59	8.24	1.33	7.84	0.02	8.02	0.62
	B	3.45		8.96		17.7		11.89		18.06		25.21		13.9		8.35		7.84		8.07	
350	A	4.00	-0.18	11.42	-5.15	21.18	1.49	14.11	1.37	21.49	2.78	29.63	3.04	17.73	-3.71	9.9	1.32	9.42	0.04	9.64	0.63
	B	3.99		10.84		21.5		14.31		22.09		30.53		17.07		10.03		9.42		9.70	
400	A	4.53	-0.22	13.51	-5.16	25.14	1.52	16.6	1.48	25.68	2.88	35.03	3.09	21.28	-3.83	11.64	1.45	11.05	0.07	11.31	0.70
	B	4.52		12.81		25.52		16.85		26.42		36.12		20.46		11.81		11.05		11.39	
450	A	5.05	-0.24	15.69	-5.23	29.29	1.49	19.19	1.47	30.15	2.81	40.67	3.13	25.05	-3.96	13.44	1.24	12.73	0.09	13.05	0.62
	B	5.04		14.87		29.73		19.47		31		41.95		24.06		13.6		12.74		13.13	
500	A	5.56	-0.27	17.99	-5.28	33.66	1.48	21.88	1.52	34.91	2.83	46.56	3.16	29.06	-4.1	15.29	1.21	14.46	0.08	14.84	0.60
	B	5.54		17.04		34.15		22.21		35.9		48.03		27.87		15.48		14.48		14.93	
550	A	6.06	-0.26	20.38	-5.26	38.21	1.52	24.66	1.61	39.95	2.9	52.67	3.25	33.28	-4.17	17.19	1.22	16.23	0.13	16.67	0.63
	B	6.04		19.31		38.8		25.06		41.11		54.38		31.89		17.4		16.25		16.77	
600	A	6.55	-0.26	22.89	-5.28	42.99	1.54	27.56	1.66	45.3	2.94	59.04	3.31	37.75	-4.27	19.15	1.19	18.05	0.14	18.55	0.62
	B	6.54		21.68		43.66		28.02		46.63		60.99		36.13		19.38		18.07		18.66	

compression depth values are very similar across different F values, and the simulation conducted on the thoracic model that included a 10 % larger heart resulted in a compression depth decrease of just under 0.3 %. With a gradual increase in the level of the applied force, this small difference also increases slightly.

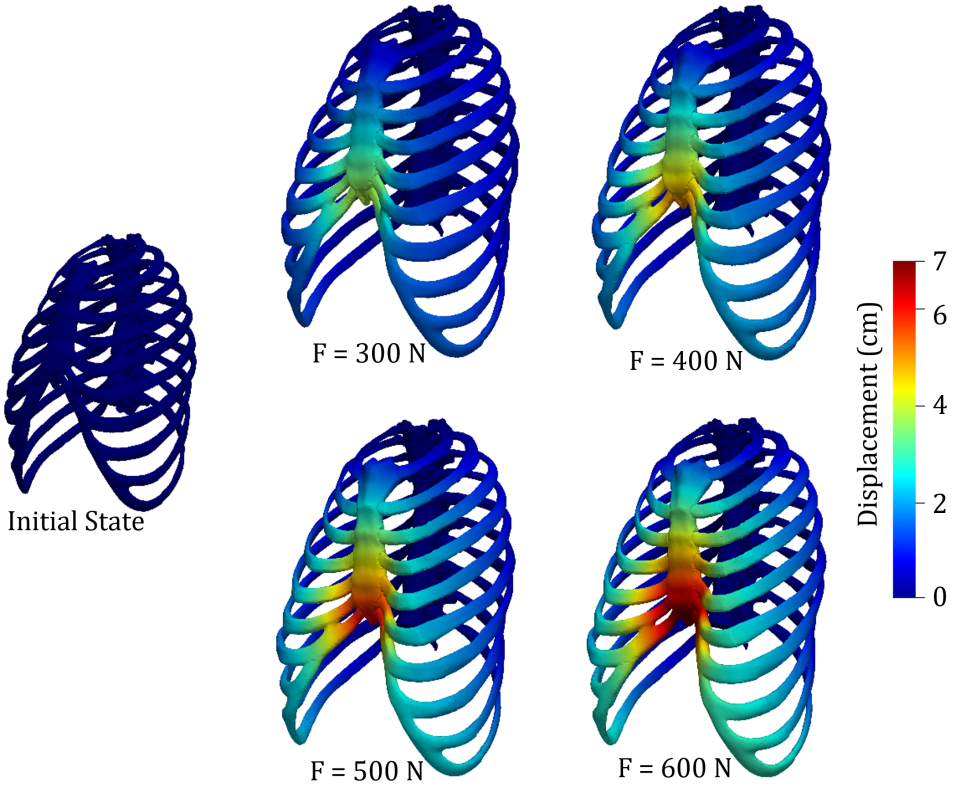

Figure 3.5: Deformation of the ribcage under different levels of applied force.

3.2.2 Heart deformation

As stated in Chapter 1, there are two primary theories that explain the mechanism of CPR: the "cardiac pump" theory and the "thoracic pump" theory. According to

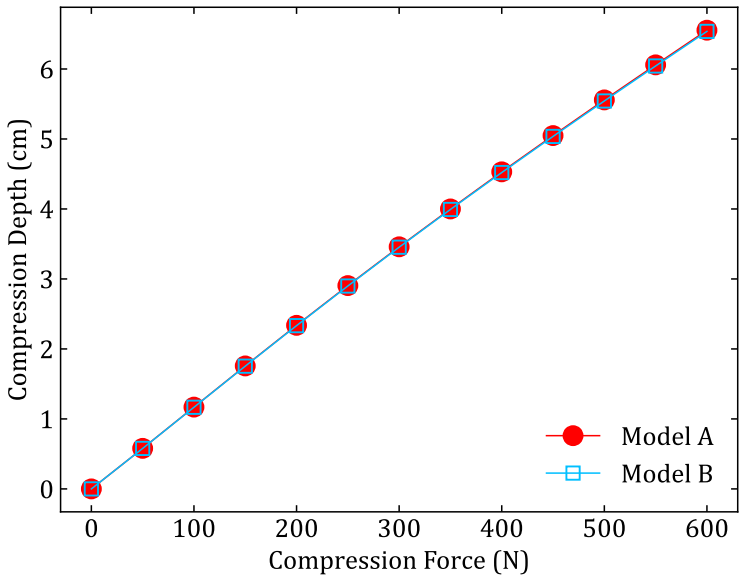

Figure 3.6: Compression depth achieved as a function of the level of the applied force for both heart geometry models A and B.

the cardiac pump theory, the deformation of the heart plays a crucial role. This section presents the simulation results for the heart deforamtion during CPR. Fig. 3.7 illustrates how the heart deforms under varying levels of applied force. It also displays the overall heart volume change (HVC) and the blood volume change (BVC) for each force level. HVC reflects the total volume change of the heart, encompassing the myocardium muscle and the blood within it, whereas BVC solely represents the change in the blood surrounded by the myocardium. Fig. 3.8 displays the ventricular deformation on the cross-section, indicating that the heart deformation in these simulations is appropriate. Moreover, under each respective contour in this figure, the changes in left ventricle volume (LVVC) and right ventricle volume (RVVC) resulting from each level of applied force are indicated. The wall of the right ventricle undergoes greater deformation than other parts of the myocardium due to its location directly beneath the force application area and its

proximity to that area (4.5 cm due to 500N force being applied). Due to its proximity to the fixed spine, the outer wall of the left atrium experiences the least amount of displacement. The maximum change in heart volume is 22.9%, with the right ventricle experiencing the most significant volume change at 59% compared to the left ventricle, which experiences a maximum volume change of 27.6%. These findings suggest that during CPR, the location of a chamber plays a more significant role in the level of deformation, contrary to what occurs during a normal cardiac cycle. The left atrium undergoes a higher deformation than the right atrium due to its location beneath the force application area, with the left atrium experiencing a maximum volume change of 45.3% and the right atrium experiencing a maximum volume change of 37.8%, according to the results presented in Table 3.2.

Venous valves prevent backward blood flow during CPR [72, 117, 118]. This means that the overall change in blood volume in the heart can be considered as the overall blood ejection fraction. Fig 3.9 shows the blood ejection fraction plotted against the compression depth for both models. It can be observed that within the recommended compression depth range (5-6 cm), the model with a larger heart predicts a slightly higher blood ejection fraction compared to the model with a smaller heart.

3.2.3 Lung deformation

According to the thoracic pump theory discussed in Chapter 1, the deformation of the lungs resulting from chest compressions plays a crucial role in CPR. Fig. 3.10

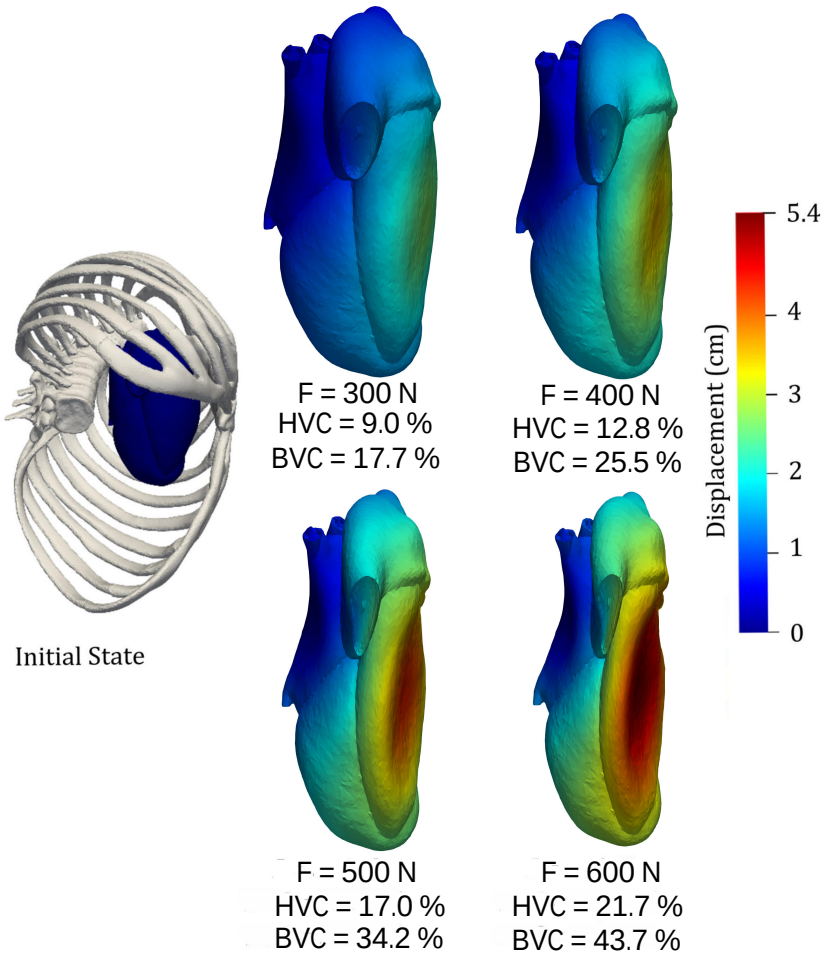

Figure 3.7: Heart deformation for different levels of applied force on the sternum.

shows the deformation of the lung in the simulation. When the chest is compressed perpendicular to the sternum, the lung tends to expand toward the arms, but the ribs and intercostal muscles prevent this expansion. The deformation of the lung is much lower in areas where it comes into contact with the ribs compared to the deformation in locations where it contacts the intercostal muscles due to the lower stiffness of the muscles in comparison to the ribs. This prevention of lung

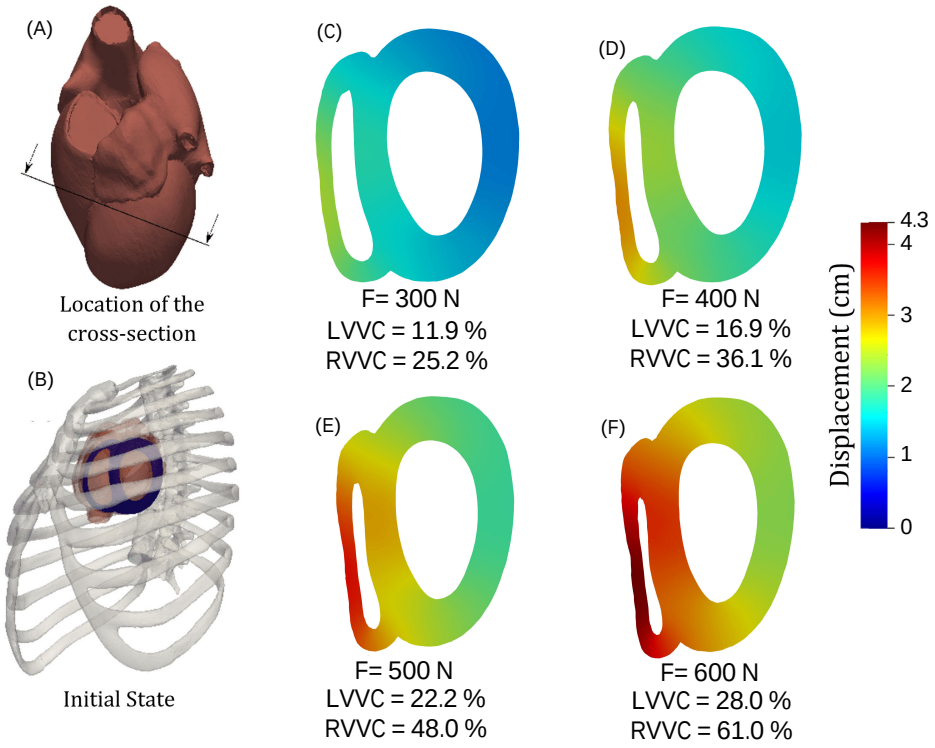

Figure 3.8: (a): The location of the cross-section on the myocardium wall; (b): The location and the initial shape of the cross-section in the chest;(c),(d),(e),(f): Details and deformation of the cross-section for different levels of applied force on the sternum.

expansion to the sides of the body leads to a decrease in lung volume. In the simulation, applying a compression range of 5 cm to 6 cm to the ribcage resulted in a reduction of left lung volume by 13.1% to 16.8% and right lung volume by 12.4% to 15.9%.

The simulation using small heart models resulted in a decrease in lung volume change compared to the simulation with larger heart model. As the force level increased during the simulations, the difference in lung volume change between the two models decreased. However, within a particular force range (above 400 N),

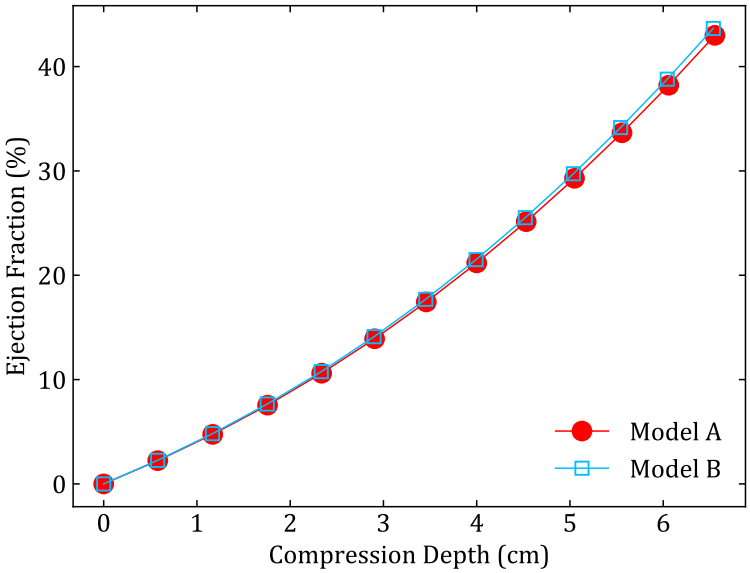

Figure 3.9: Predicted blood ejection fraction from the heart during the CPR compression for both heart geometry models.

the difference remained above 10 %, indicating that the choice of heart model can have an impact on the effectiveness of chest compressions and subsequent lung volume changes.

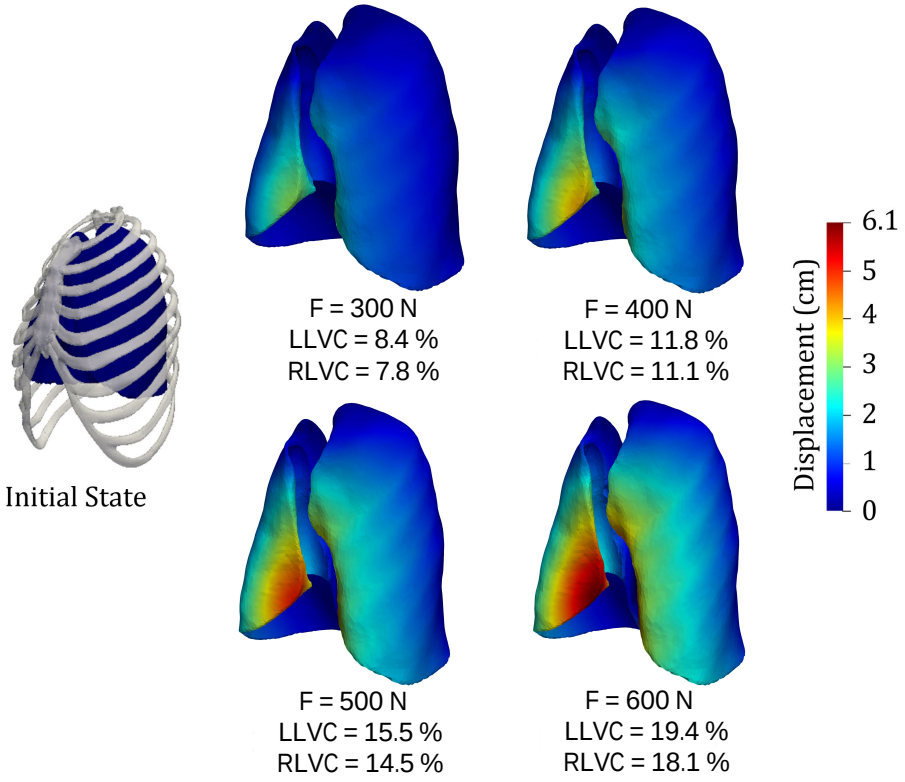

Figure 3.10: Lung deformation under different levels of applied force on the sternum

Chapter 4

Discussion

The focus of this chapter is to conduct a comprehensive analysis of the findings presented in the previous chapter. We will commence by discussing the equations presented in Chapter 3 for compression depth and ribcage maximum stress and will endeavor to simplify the equations by reducing the number of parameters while retaining their precision. In the following, we will provide a higher precision discussion of the simulation results on the full model. The primary goal will be to compare these results with the theoretical mechanisms of CPR described in the literature, with the aim of evaluating the accuracy and consistency of the simulation results with the existing literature on CPR.

4.1 Modification of the predictive equations

The generic form of the fit provided in Equation (3.1) is highly relevant as it serves as a valuable guide for future statistical analyses of empirical data related to CPR.

It helps identify which physical parameters describing the geometry of the patient's rib cage (as listed in Table 2.1) should be considered to characterize the relationship between the measured compression depth (ΔY) and rib cage dimensions. The volume of the rib cage, denoted as V = $W_R \times L_R \times H_R$, may not be a suitable parameter for characterizing the dependence of compression depth, as indicated by the varying exponents of δX, δY, and δZ in Equation (3.2). This means that the change in compression depth, as predicted by Equation (3.2), would depend on how V is altered. For instance, if V is increased by 10% by solely increasing the rib cage width, then ΔY would increase by approximately 5.4% ($1.1^{0.552}$ = 1.054) according to the equation. However, if the same 10% increase in V is achieved by solely increasing the rib cage depth, then ΔY would instead decrease by about 7% (as $1.1^{-0.753}$ = 0.930), rather than increasing. By applying the same reasoning, it becomes evident that Equation (3.2) indicates that the horizontal cross-sectional area ($A_{XY} = W_R \times L_R$) and the vertical frontal cross-sectional area ($A_{XZ} = W_R \times H_R$) are not appropriate parameters to correlate with empirical data on ΔY. Furthermore, if the change in rib angle (θ) can be approximated by the change in its tangent, i.e., $\delta\theta \approx \delta(tan\theta) = \delta Y/\delta Z$, it is worth noting that the exponents of δY and δZ in Equation (3.2) have the same sign, suggesting that rib angle is also not a suitable candidate for correlating ΔY variations.

On a positive note, we can consider utilizing two other physical quantities from Table 2.1, namely the Haller index and the sagittal cross-sectional area. Variations in the Haller index (HI, as shown in Fig. 2.2A) and the sagittal cross-sectional area (A_{yz}) can be expressed as δHI = δX/δY and $\delta A_{YZ} = \delta Y \times \delta Z$, respectively. Therefore, based on the signs of the exponents in Equation (3.2), these derived

quantities could be suitable candidates for empirical correlation with ΔY. To illustrate this idea, let's rephrase Equation (3.2) in terms of HI and A_{yz} instead of δX and δY:

$$\Delta Y_{P1}(\text{ cm}) = 0.0398 F^{0.757} \delta HI^{0.552} \delta A_{YZ}^{-0.211} \delta Z^{-0.095} \pm 0.0370 \text{ cm}, \quad 450N \leq F \leq 600N \tag{4.1}$$

There are two statistical indicators that suggest Equation (4.1) is superior to the original Equation (3.2). First, the sum of the absolute values of the exponents on the geometrical quantities is significantly lower in Equation (4.1) (0.858) compared to Equation (3.2) (1.621), indicating that random measurement errors are less likely to propagate in Equation (4.1). Second, the exponent associated with the least significant geometrical parameter in Equation (4.1) is close to zero (-0.095 on δZ), implying that this parameter has minimal impact on the overall equation. Furthermore, Figure 4.1 provides a compact graphical representation of the numerical results obtained from all the FE simulations conducted within the $450N \leq F \leq 600N$ force range, adding to the convenience of using Equation (4.1).

Furthermore, the relatively low absolute exponent of δZ in Equation (4.1) suggests that a reasonably accurate correlation of empirical data could be achieved by simplifying Equation (4.1) to ΔY = ΔY(F, HI, A_{yz}), neglecting the explicit dependence of ΔY on rib cage height. The corresponding fit, when the dependence on δZ is ignored, is given by:

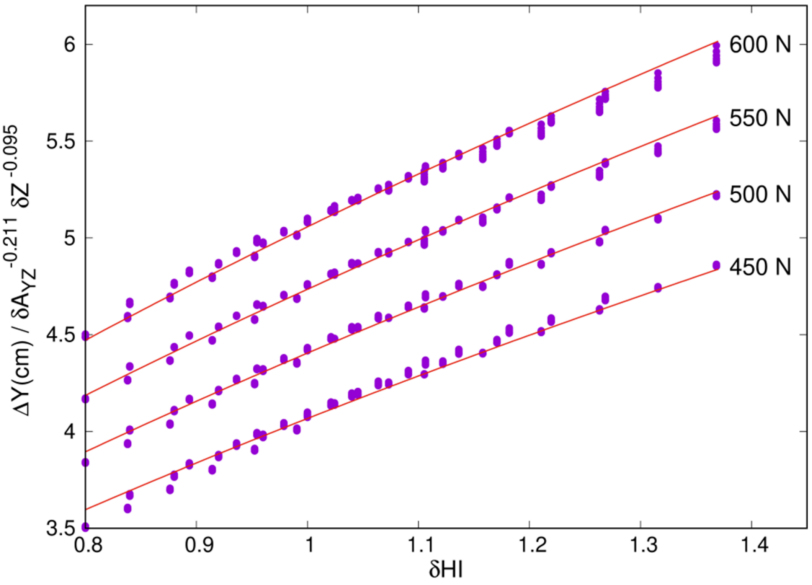

Figure 4.1: The relationship between the compression height, ΔY, and the Haller Index, HI, shown explicitly. The solid circles represent the predicted values from the simulations, while the red lines depict the values calculated using the equation (4.1) fit, which is given by the function $G(F, HI) = 0.0398F^{0.757}\delta HI^{0.552}$.

$$\Delta Y_{P1}(\text{ cm}) = 0.0397F^{0.757}\delta HI^{0.513}\delta A_{YZ}^{-0.267} \pm 0.0443 \text{ cm}, \quad 450N \leq F \leq 600N \tag{4.2}$$

As expected, when the dependency of the achieved compression depth on δZ is dropped, the fit to the FE simulation data is poorer, with a larger rms error of ±0.0443 cm in Equation (4.2), compared to ±0.0370 cm for the fit in Equation (4.1). The three-variable model (Equation (4.2)) can be considered statistically less meaningful compared to the original model in Equation (4.1), as indicated by the Akaike information criterion (AIC) value, which is more than 10 units higher for the former model than for the latter one [119]. Nevertheless, reducing the dependence of ΔY from four to three independent variables represents a significant gain

in terms of the number of data points (sample size) required to achieve a reasonably accurate fit.

As previously mentioned, mechanically assisted CPR is commonly used in modern medical practice. In such cases, a specific compression depth target is set, and a mechanical device applies the necessary compression force ($F_{\Delta Y}$) to achieve the target compression depth (ΔY). Although the simulations in this study were set up for a fixed force level (which is more representative of manual CPR), the equations (3.2), (4.1), and (4.2) can also be used for interpolation. For example, if the target compression depth is set at 5 cm, the corresponding fits for F5cm based on equations (3.2), (4.1), and (4.2) are:

$$F_{5cm}(\text{ N}) = 590.3\delta X^{-0.712}\delta Y^{0.898}\delta Z^{0.404} \pm 5.29\text{ N} \tag{4.3}$$

$$F_{5cm}(\text{ N}) = 590.3\delta HI^{-0.712}\delta A_{YZ}^{-0.267}\delta Z^{0.128} \pm 5.29\text{ N} \tag{4.4}$$

$$F_{5cm}(\text{ N}) = 591.5\delta HI^{-0.658}\delta A_{YZ}^{-0.351} \pm 6.16\text{ N} \tag{4.5}$$

The rms error for the approximate 2-variable interpolation of F_{5cm} in Equation (4.5) is higher at 6.16 N compared to the rms error in Equation (4.4) which is 5.29 N. However, the difference between these two rms values is relatively small, at 0.87 N, and can be considered modest. Figure 4.2 provides a visual comparison of the F_{5cm} interpolations in equations (4.4) and (4.5). It's important to note that only the results of FE simulations with ΔY values close to 5 cm are shown in the plots of Figure 4.2A and Figure 4.2B. However, since none of the FE simulations achieved an exact compression depth of 5 cm, there is inevitably some dispersion of the data points around the interpolation line in the plots, in addition to the

inherent error in the fit.

Qualitative comparison of Figure 4.2A and Figure 4.2B plots supports the idea that the approximation model in Equation (4.4) that does not consider δZ explicitly introduces only a small amount of additional error. Although, as mentioned earlier, the statistical significance of the simplified model in (4.5) is low compared to the full model in (4.4), as indicated by the higher AIC value. From a practical perspective, this simplification is particularly important since the antero-posterior diameter (D_{AP}) and transverse diameter (D_T) needed for the Haller index calculation are often easier to measure than rib cage height (H_R). Note that Equations (4.4) and (4.5) reveal that the compression force required to achieve a specific level of rib cage compression mainly depends on the Haller index, with a highly negative exponent. Thus, patients with a low Haller index require greater compression force during CPR.

Equation (3.4) provides valuable information on how the maximum von Mises stress levels (σ_v) experienced by the ribs during CPR depend on the compression force and rib cage dimensions. However, from a practical perspective, it is also important to understand how σ_v is influenced by rib cage geometry when a target compression depth (ΔY) is set for CPR. To investigate this, we can generate interpolation fits based on Equation (3.4) by substituting the F input quantity with the ΔY output quantity. For instance, for the 6th left rib, we obtain:

$$\sigma_v^{(6L)}(\text{ MPa}) = 11.28(\Delta Y(\text{ cm}))^{0.689}\delta X^{-0.676}\delta Y^{0.0099}\delta Z^{-0.060} \pm 0.365\text{ MPa} \quad (4.6)$$

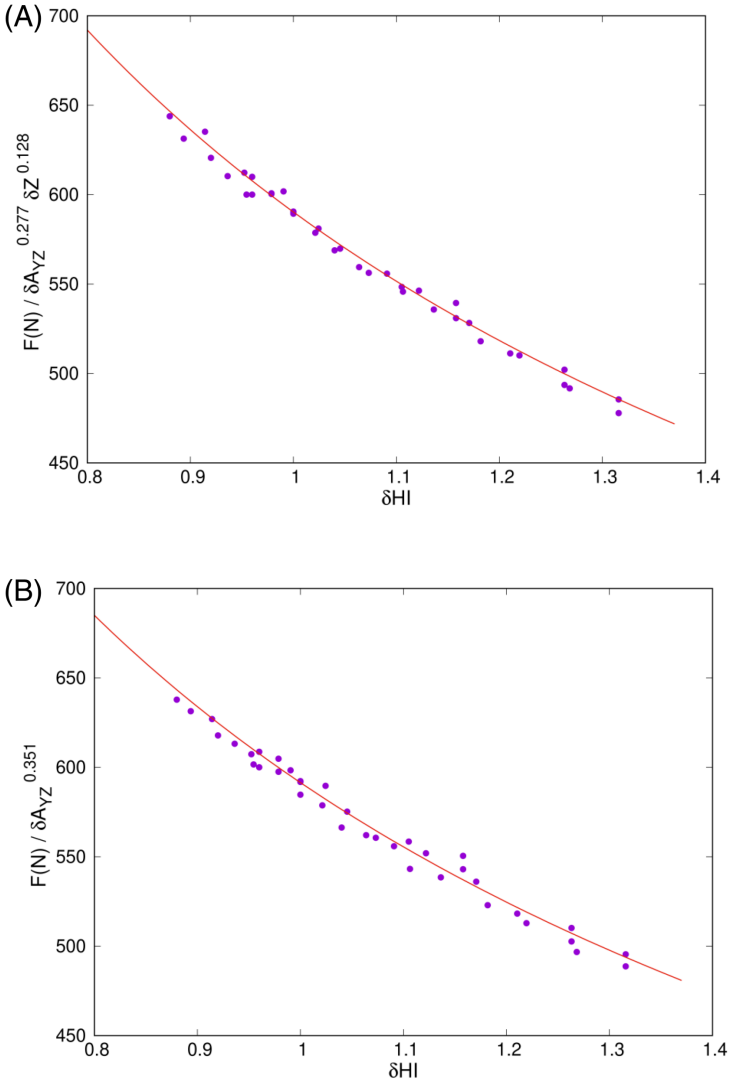

Figure 4.2: The relationship between the Haller index (HI) and the force required to achieve a target compression depth of ΔY = 5 cm at compression area P1 (F_{5cm}). The filled circles in the plots represent results from simulations that yielded ΔY values within 0.037 cm of the target, which is not further away than the rms of the fit in Equation (4.1). The solid lines in parts (A) and (B) represent the functions provided by Equations (4.4) ($G(HI) = 590.3\delta HI^{-0.712}$) and (4.5) ($G(HI) = 591.5\delta HI^{-0.658}$), respectively

For a desired compression depth of ΔY = 5 cm, the maximum σ_v for the 6th left rib is given by the equation:

$$\sigma_{v,5cm}^{(6L)}(\text{ MPa}) = 34.22\delta X^{-0.676}\delta Y^{0.0099}\delta Z^{-0.060} \pm 0.365 \text{ MPa} \tag{4.7}$$

For the sake of brevity, additional equations for the remaining ribs are not included here, although they follow the same trend as Equations (4.6) and (4.7) with different exponents. The dominant exponent for all these equations is always on δX, indicating that changes in the rib arc-length have the greatest impact on the resistance to bending. When the W_R increases (while keeping L_R and H_R constant), the rib arc-length also increases, leading to a decrease in the resistance to bending. Conversely, when W_R decreases, the rib arc-length shortens, resulting in an increase in resistance to bending from a mechanical standpoint, as reflected in Equations (4.6) and (4.7).

The results obtained from the fits in Equations (3.4) and (4.6) and (4.7), as well as the qualitative information provided by the plots in Figure 3.4, suggest that the risk of rib fracture during CPR would not be significant, as the maximum stress (σ_v) in the ribs remains below the fracture tension limit (around σ_C = 50 MPa [54]). However, empirical evidence shows that rib fractures do occur during CPR maneuvers [40, 120, 121], and some authors argue that chest injuries are an acceptable trade-off for achieving effective chest compressions [122]. It should be noted that the predicted maximum σ_v values for a target CPR compression depth of 5 cm exceed the yield strength limit (σ_Y = 30 MPa) set in the elastoplastic model for osseous tissue (as per Equation (4.7)). This suggests that the chest may not fully recover its original state after completing a compression cycle and that the osseous

rib tissue may gradually deteriorate in subsequent CPR cycles, as indicated by the present FE results.

Moreover, a more comprehensive interpretation of the findings from Equations (3.4) and (4.6) and (4.7) can be described as follows. When a certain level of compression force (F) is applied during CPR, two opposing effects come into play. On one hand, ΔY (a positive outcome) increases with higher F, but on the other hand, the stress levels experienced by the ribs (a negative outcome) also increase. It should be noted that Equations (3.2), (3.3), and (4.1) collectively suggest that patients with a wider chest (larger W_R and HI) generally exhibit a higher ΔY for a given F. Furthermore, Equation (4.4), along with the fit parameter values in Table 3.1, indicates that patients with larger chests actually experience lower stress levels in their ribs. Equation (4.6) also supports this finding for CPR performed with a target compression depth, suggesting that patients with a wider chest (larger W_R and transverse diameter, D_T) would have lower stress levels on their rib cage during CPR.

Recently, Azeli et al. [120] reported that there is a statistical correlation between a larger chest circumference of patients and the risk of severe chest injuries during CPR. The measured chest circumference is directly related to the in-plane rib arc-length, which is known to increase with age [123]. Previous studies have established typical changes in chest morphology with age, including an increase in the angle of the ribs (θ), resulting in an increase in the chest antero-posterior diameter (D_{AP}) and a decrease in the transverse diameter (D_T) [123–127]. In other words, older patients tend to have more horizontally aligned ribs and a lower

Haller index (*HI*) of their chests (as shown in Figure 2.2A). This increase in rib angle is associated with a higher risk of rib fractures and increased thoracic stiffness [125, 127]. These findings are in line with the results of the present simulations. Equation (4.4) suggests that for a given target compression depth, the required compression force and apparent thoracic stiffness would increase with decreasing HI. Similarly, according to Equation (4.7), the maximum stress levels in the ribs, and thus the probability of rib fracture during CPR, would increase with decreasing D_T.

4.2 Discussion of comprehensive model results

A value of at least 5 cm has been suggested for the compression depth by American Heart Association (AHA) guidelines [128]; based on the findings of this study, this value is equivalent to the compression depth for applying an approximate force of 440 N for model A. Additionally, guidelines from the European Resuscitation Council (ERC) propose a compression depth of 5 to 6 cm [35]. Based on the present findings, achieving this compression depth necessitates a force ranging from approximately 440 N to 540 N. The information displayed in Table 3.2 demonstrates that there is an insignificant difference (less than 0.3%) in the compression depth obtained from simulations using two diverse models with varying heart sizes. Hence, if the size of the heart increases by 10%, it would only result in a reduction of 0.3% in the compression depth (or in other words, if the heart size decreases by 9 %, the compression depth increase just by under 0.3 %). In this

particular situation, despite a significant increase in heart volume (10%) and myocardium thickness (almost 20%), the overall resistance of the chest to compression remains largely unaffected, suggesting that the heart's resistance is negligible in comparison to the overall resistance of the chest.

More force can be used to reduce the volume even further, but it also increases the risk of rib fractures. Furthermore, vascular compliance can play a crucial role in the limited output produced by chest compressions during CPR. Excessively forceful compressions may restrict filling or deplete volume in the cardiac chambers and great central vessels, thereby limiting blood flow [129].

Although there have been no clinical studies on heart volume changes during CPR, it is generally assumed that achieving a larger ventricle compression during a CPR cycle increases the chances of ROSC. This aligns with the cardiac pump mechanism theory, which proposes that compression and decompression phases during CPR cause high deformation in the ventricles, creating a pressure gradient between the ventricle and the aorta (or pulmonary artery for the right ventricle) and resulting in blood flow during chest compression [72]. The present numerical model also supports this theory by predicting significant changes in ventricular sizes during CPR. According to the obtained results, recommended chest compression depths of 5-6 cm, corresponding to a force of 440 N to 540 N, can result in volume changes ranging from 15.3% to 19.9% in the total volume of the heart, 39.5% to 51.4% in the right ventricle, 18.7% to 24.1% in the left ventricle and 28.5% to 37.3% in the total volume of the blood in the heart, resembling the systolic squeezing and diastolic relaxation of a normal cardiac cycle [11]. The cardiac pump mechanism is the main CPR mechanism in the initial phases of CPR

and is backed by compelling clinical evidence and suggests that high deformation in the ventricles occurs during CPR [72, 76].

Based on the findings presented in Table 3.2, simulating a larger heart results in a slightly higher change in the overall blood volume. This suggests that during the initial phases of CPR, when the primary mechanism relies on heart deformation, a larger heart undergoes a slightly larger volume change, potentially contributing to a slightly higher blood ejection fraction within the heart (Fig 3.9). However, it is important to note that the observed difference is only approximately 1.5% for the practical applied forces. Based on the present results, it cannot be asserted that heart size has a substantial effect on the outcome of CPR.

Lung compression due to chest compression has a key role in the blood flow during CPR. During the late stages of resuscitation, a thoracic pump mechanism might be the major determinant of forward blood flow because of a relatively stiff myocardium [76]. According to this theory, blood flow is not generated by direct cardiac compression but rather by an increase in intrathoracic pressure during compression, which forces blood from the thoracic vessels into the systemic circulation [130, 131]. Based on clinical observations, compressing of the lung due to chest compression leads to an increase the thoracic pressure [132].

As the stiffness of the heart increases over time during CPR, the heart's volume change due to chest compression decreases, leading to an increase in the volume change of the lung. While there is no data on the rate of change in myocardium stiffness during CPR, even with the consideration of constant myocardial properties, the present model confirms the hypothesis of an increase in intrathoracic pressure during chest compression.

The results provided in Table 3.2 indicate that the lung volume change induced by chest compression is higher for the case with a larger heart. The effect of heart size on the deformation of the lung and, consequently, on thoracic pressure is higher for lower levels of force, and this effect decreases by increasing the force level. This implies that the effect of heart size on lung volume change is higher for low deformation of the heart. While the deformation of the heart is not significant in the thoracic pump mechanism, it can be stated that the size of the heart has a meaningful positive impact on the thoracic pressure during the late phase of CPR. This means that a larger heart size leads to a higher thoracic pressure, increasing the chance of ROSC.

Chapter 5

Dynamic simulation of the comprehensive model

This study initially focused on static simulations. However, to study time-dependent parameters, considering the factor of time is necessary. To address this, a FE dynamic simulation is deemed necessary to explore the relationship between applied force and displacement over time. The material models employed thus far in the study, based on elasticity and elastoplasticity, were effective but lacked inherent time dependency and did not account for time-related parameters and their effects on material behavior. To address this limitation, a viscoelastic model for the ribcage was introduced to approximate realistic outcomes in the simulations. Firstly, this chapter discusses the importance of utilizing a dynamic simulation with a viscoelastic ribcage model. After that, the results for a compression rate of 100 compressions per minute are presented, including a comparison to experimental work. Finally, the effects of two compression rates (100 and 120 compressions per minute) on different parameters are discussed.

5.1 Introduction

In study 1, the aim was to predict the ribcage response to a single compression, considering various applied forces and ribcage dimensions. Study 2 focused on incorporating additional organs and tissues into the model to predict the thorax response to a single compression, along with the deformation of internal organs. These studies utilized static simulation, which yielded valuable results. Previously, the time factor was considered unnecessary, and static simulation was used to analyze the effects of different parameters on CPR outcomes.

Considering the element of time is necessary when examining the impact of time-dependent parameters, such as compression rate, or when conducting simulations involving multiple compressions. To achieve this, a different type of simulation, known as dynamic simulation, must be employed. By employing this FE simulation technique, we will be able to thoroughly investigate the relationship between the applied force and displacement at every distinct moment in time.

Experimental studies conducted on CPR reveal that force-displacement curve is not the same for the compression and decompression phases. This difference makes a hysteresis loop in the force-displacement graph [21, 133]. The existence of this hysteresis loop serves as a crucial criterion for representing the time-dependent properties exhibited by the ribcage. It is important to note that this phenomenon can be attributed to the viscoelastic nature of the ribcage [134, 135]. To achieve simulation results that closely resemble experimental data, it is necessary to employ a viscoelastic model for the ribcage. This model will help to approximate the experimental outcomes and provide valuable insights into CPR dynamics.

5.2 Viscoelatic model

In this study, the behavior of the ribs and intercostal muscles was modeled using the standard linear solid (SLS). The schematic representation of this model is shown in Figure 5.1.

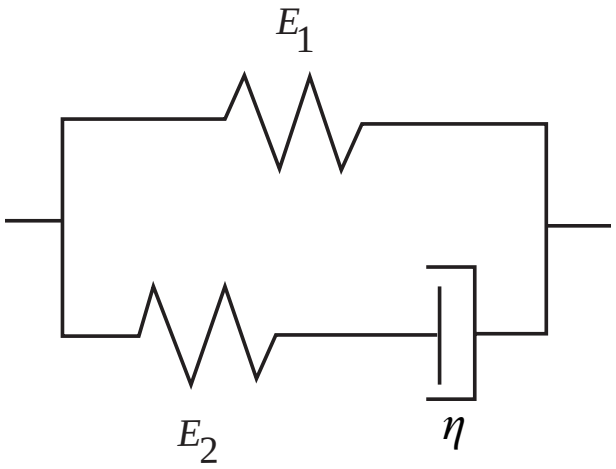

Figure 5.1: Schematic illustration of the viscoelastic model.

The SLS model was initially proposed by Schmid-Schonbein et al. in 1981 [136] for studying small-strain deformation. The constitutive relation of the SLS model can be expressed as [136, 137]:

$$s_{ij} + \frac{\eta}{E_2}\dot{s}_{ij} = e_{ij}E_1 + \dot{e}_{ij}\eta\left(1 + \frac{E_1}{E_2}\right), \tag{5.1}$$

where E_1 and E_2 represent two elastic coefficients, and η denotes the viscous coefficient. In Equation 5.1, s denotes the deviatoric stress tensor (as defined in Equation (2.17)), and e refers to the deviatoric strain tensor, which is defined as:

$$e_{ij} = \varepsilon_{ij} - \frac{1}{3}\delta_{ij}\varepsilon_{kk}. \tag{5.2}$$

The notation $\dot{s}_{ij}$ and $\dot{e}_{ij}$ signifies the time derivatives of the stress and strain deviators, respectively, i.e., $\partial s_{ij}/\partial t$ and $\partial e_{ij}/\partial t$.

5.3 Material Properties

In this simulation, the material properties used are the same as in study 2, except for the ribs and intercostal muscles. For these organs, the SLS viscoelastic model has been employed. The specific viscoelastic parameters for the ribs and intercostal muscles used in this study are presented in Table 5.1.

Table 5.1: Viscoelastic Parameters for Ribs and Intercostal Muscles in the Dynamic Simulation

Tissue	E_1 (MPa)	E_2 (MPa)	η (MPa.s)
Breastbone, Osseous ribs	777	27820	149.1152
Intercostal muscles	6	6	0.12

5.4 Boundary conditions

A sinusoidal force is used to compress the chest with a maximum force of 500N and a period of 0.6 sec which is equal to a compression rate of 100 compressions per minute. The details of the applied force have been shown in Fig 5.2 for three cycles. The location of the applied force is the same as the study 2. Also the geometry used in this simulation is the same as the geometry with a large heart in study 2.

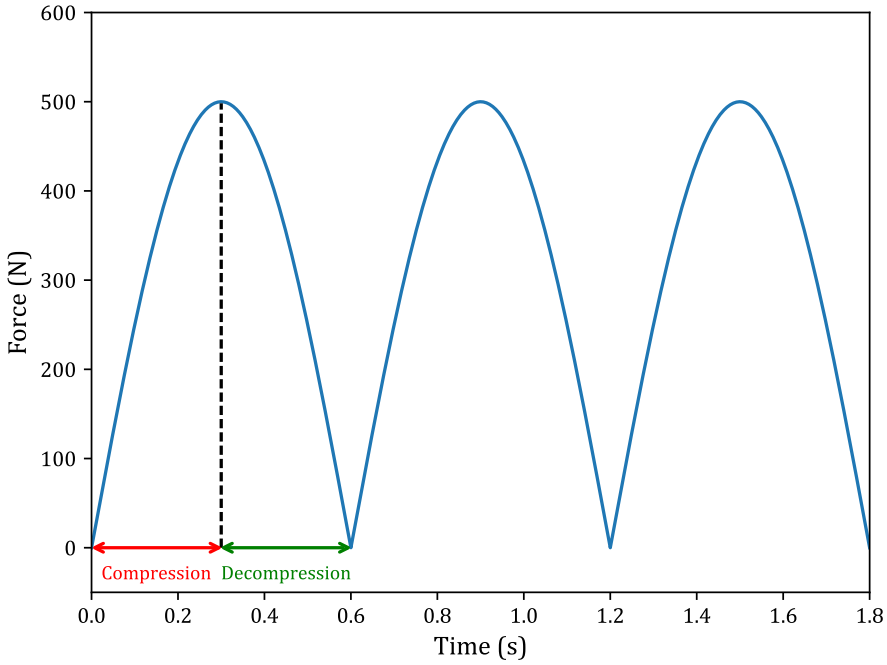

Figure 5.2: Sinusoidal Force Profile for Chest Compression at 100 Compressions per Minute .

5.5 Results and Discussion

5.5.1 Force-deflection curve

The force-deflection curve depicted in Fig. 5.3 provides valuable insights into the nonlinear and time-dependent characteristics resulting from the viscoelastic properties of the ribs. During compression, the ribcage undergoes deformation, leading to an increase in compression depth. However, during decompression, the chest exhibits hysteresis, where the force required to maintain a specific deflection is lower compared to loading. This behavior is attributed to the viscoelastic nature of the ribcage, which allows it to exhibit time-dependent deformations and resist immediate recovery .

The force-deflection curves in Fig. 5.3 show the presence of residual deflection at the end of each compression-decompression cycle. In cycle one, a noticeable residual deflection is observed, and there is a slight increase in residual deflection during cycle two. However, by the end of cycle three, the residual deflection is almost the same as the starting point. These differences in increasing residual deflection between cycles can be attributed to energy dissipation within the viscoelastic material during the first cycle [135, 138].

Comparing the force-deflection curves for cycle two in our study (blue curve) with those from an experimental study [133] (red curve) in Fig. 5.4 reveals similar patterns, indicating the presence of a hysteresis loop in the force-displacement relationship. Discrepancies between these curves can be attributed to factors such as differences in body dimensions, maximum applied force, and the experimental

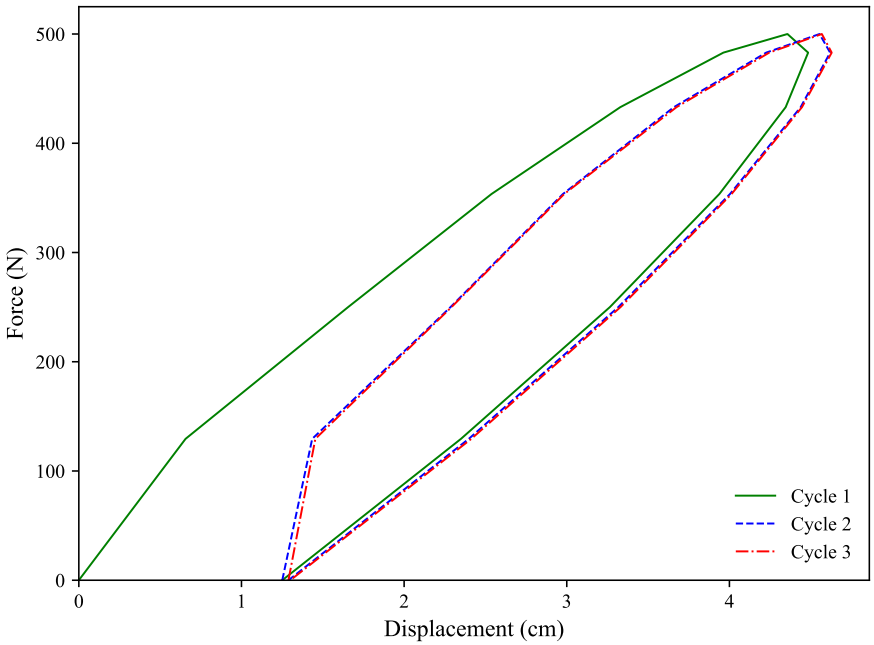

Figure 5.3: Force-Deflection Curve during Three Cycles at a Compression Rate of 100 Compressions per Minute.

setup compared to our finite element (FE) simulation. Nonetheless, this comparison demonstrates a favorable correspondence between the results obtained in our study and those reported in experimental studies.

5.5.2 Variation of compression depth by time

Fig. 5.5 provides insight into the average displacement of the applied force location over time for three compression cycles. At the end of cycle 1, a minimum displacement of 1.25 cm is observed, representing the residual deflection after compression. A slight increase in this residual displacement is seen at the end of cycle 2 (1.29 cm), and there is a marginal difference between cycle 2 and cycle 3

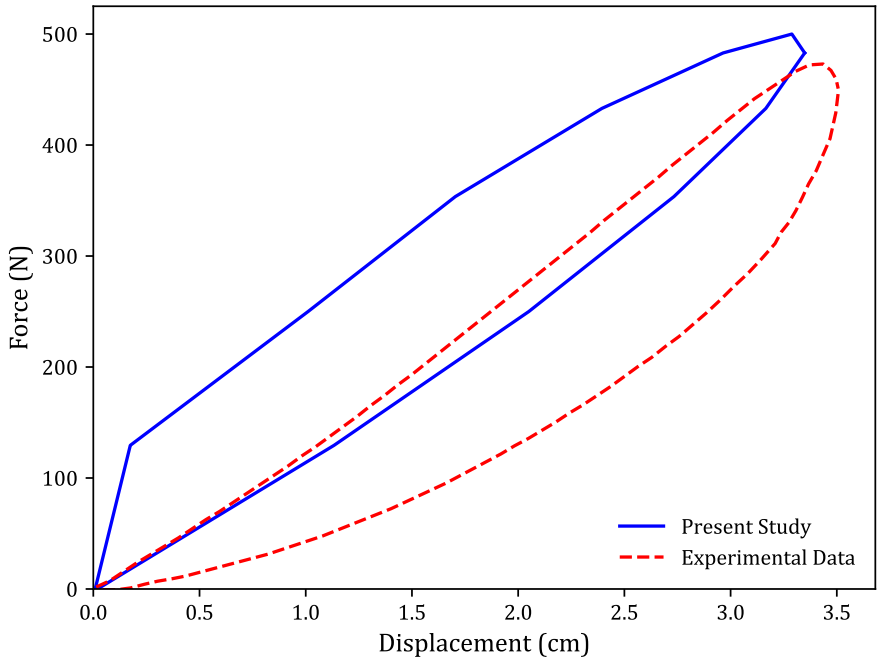

Figure 5.4: Comparison of Force-Deflection Curves: Cycle Two of our Study (Blue Curve) vs. Experimental Study [133] (Red Curve).

(1.29 cm and 1.3 cm, respectively). The graph also reveals a similar trend in maximum compression depth, with cycle 1 recording a maximum depth of 4.48 cm, increasing to 4.62 cm in cycle 2, and reaching 4.63 cm in cycle 3.

It is interesting to note that the time of maximum compression depth does not align with the time of maximum force. This discrepancy can be attributed to the viscoelastic properties of the ribcage, causing time-dependent deformations and resistance to immediate recovery. Consequently, the timing of the maximum compression depth differs from that of the peak force, emphasizing the influence of the ribcage's viscoelastic properties on the dynamics of compression and highlighting the complex behavior of the chest during chest compressions.

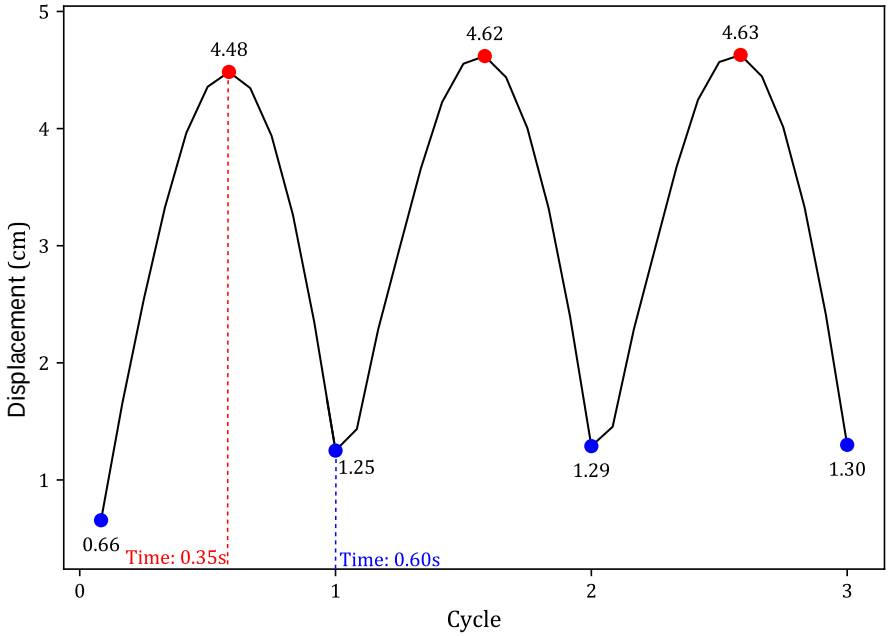

Figure 5.5: Temporal Variation of Applied Force Location Displacement in Various Chest Compression Cycles.

5.5.3 Variation of heart volume by time

Fig. 5.6 presents the variation in heart volume over time. The time of minimum volume aligns with the time of maximum compression depth, indicating a relationship between chest compressions and the heart's pumping activity. Examining the maximum change in heart volume across the compression cycles provides insights into the heart's efficiency in pumping blood. In cycle 1, the maximum change in heart volume is 13.6%, but it decreases to 11.26% in cycle 2 and further reduces to 11.22% in cycle 3. These diminishing percentages suggest a decline in the heart's efficiency in pumping blood after the first cycle, which can be attributed to the residual deflection in the chest caused by the viscoelastic properties

of the ribcage.

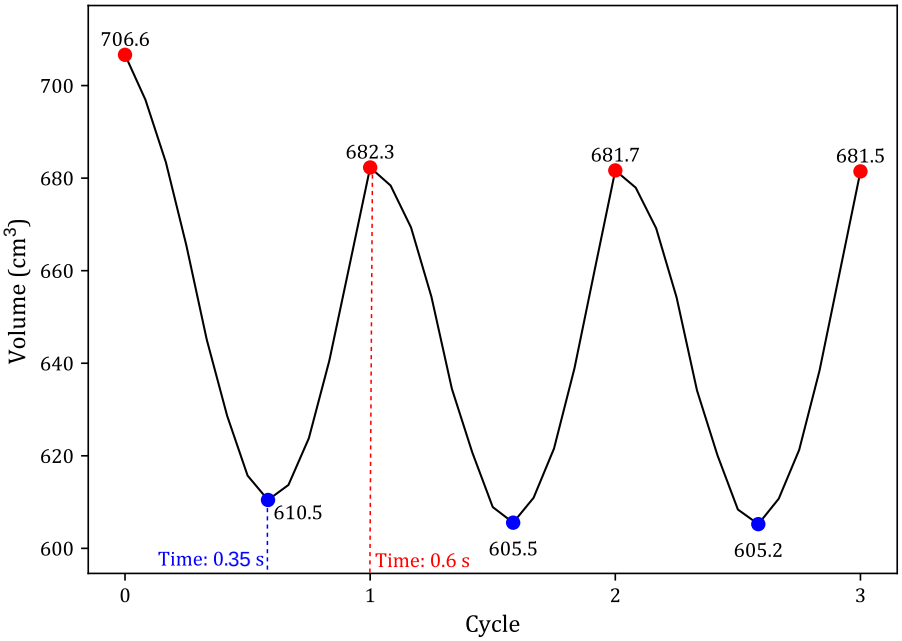

Figure 5.6: Temporal Variation of the Heart Volume in Various Chest Compression Cycles.

5.5.4 Variation of lung volume by time

Fig. 5.7 depicts the deformation of lung volume over time. The time of minimum lung volume aligns with the maximum compression depth, indicating a relationship between chest compressions and lung dynamics. However, there is an intriguing observation that the time of maximum lung volume differs from the time of minimum compression depth. At 0.65 seconds, the lung volume reaches its maximum, while the minimum compression depth occurs at 0.6 seconds. The reasons for this time disparity require further investigation, considering factors

such as the mechanical properties. Additional studies are necessary to unravel the mechanisms governing lung volume changes during chest compressions.

Similar to heart volume, the change in lung volume exhibits a decreasing trend across the compression cycles. In the first cycle, the change in lung volume is 12.87%, which reduces to 10.03% in cycle 2 and further decreases to 10.01% in cycle 3. This decreasing trend suggests a diminishing effectiveness of thoracic pressure with subsequent cycles of compression. Further investigations and comprehensive analyses are needed to fully understand the observed differences in lung volume dynamics and their relationship to compression depth.

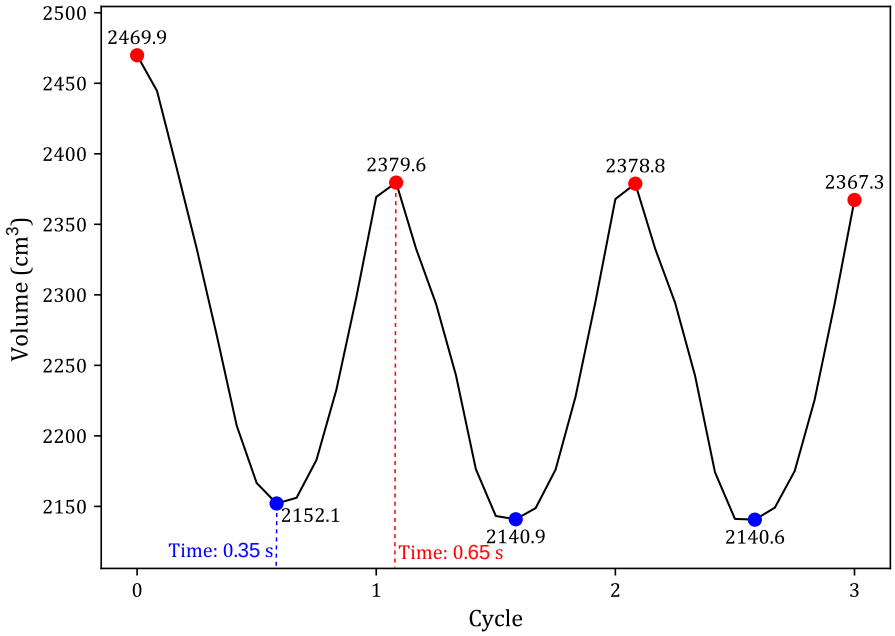

Figure 5.7: Temporal Variation of the Lung Volume in Various Chest Compression Cycles.

5.5.5 Effect of compression rate on force-deflection curve

Fig. 5.8 provides a visual comparison of the force-deflection curves for compression rates of 100 and 120 compressions per minute. While the curves exhibit overall similarity, there are slight differences in maximum compression depth and residual deflection. Analyzing Fig. 5.9 alongside Fig. 5.8 allows for a more comprehensive analysis of compression characteristics. At a compression rate of 100 compressions per minute, a higher maximum compression depth is observed compared to the rate of 120 compressions per minute. This can be attributed to the longer duration of each compression cycle, allowing for deeper compression and increased chest displacement. On the other hand, at a compression rate of 120 compressions per minute, the shorter compression cycle duration limits the chest's ability to fully recover and respond to the applied force, resulting in a slightly lower maximum compression depth. Additionally, the comparison of residual deflection reveals a slightly higher value for the compression rate of 120 compressions per minute due to the shorter compression phase duration.

5.5.6 Effect of compression rate on the variation of heart and lung volume over time

Fig. 5.10 and 5.11 provide a comparison of the volume changes in the heart and lung, respectively, for the two compression rates. The maximum volumes in the heart and lung are lower for the compression rate of 120 compressions per minute compared to the rate of 100 compressions per minute. Conversely, the minimum volumes for both organs are higher for the compression rate of 120 compressions

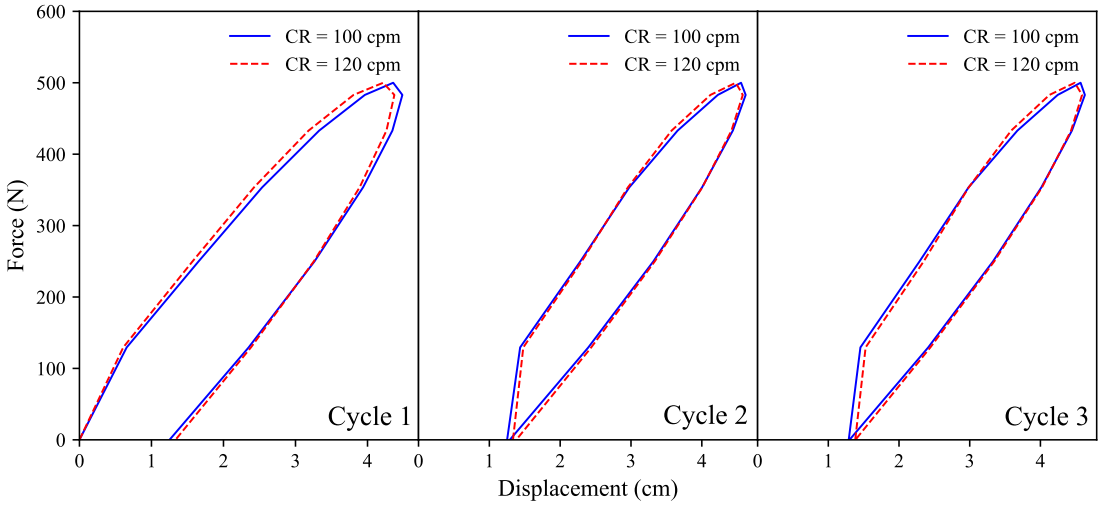

Figure 5.8: Comparison of Force-Deflection Curves for Different Compression Rates in Various Cycles.

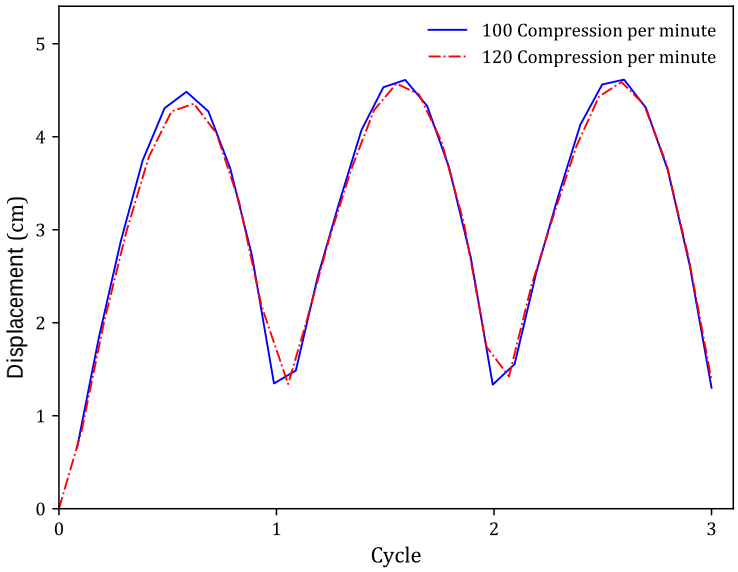

Figure 5.9: Temporal Variation of Applied Force Location Displacement for Different Compression Rates in Various Chest Compression Cycles.

per minute. These findings indicate that volume changes in CPR with a compression rate of 120 compressions per minute are lower compared to the rate of 100 compressions per minute, suggesting a decrease in the efficiency of blood circulation and lung ventilation. These observations can be attributed to the viscoelastic properties of the ribcage. Although a higher compression rate allows for more compressions within a given time frame, the specific impact and clinical implications of this factor were not investigated in this study. Further research is needed to comprehensively understand the trade-offs between compression rate, volume changes, and overall CPR efficacy, considering various physiological and clinical factors.

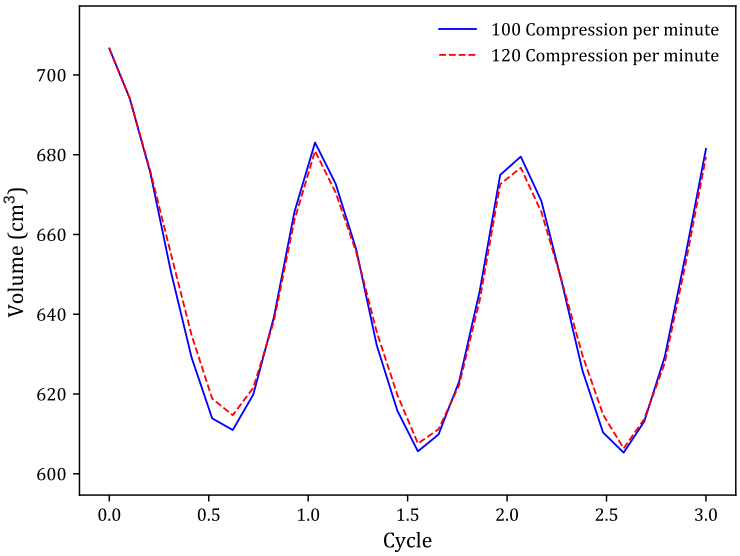

Figure 5.10: Temporal Variation of the Heart Volume for Different Compression Rates in Various Chest Compression Cycles.

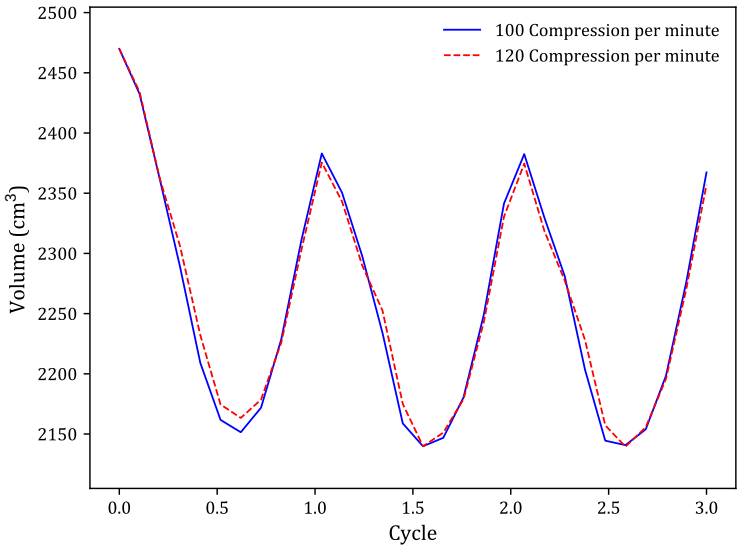

Figure 5.11: Temporal Variation of the Lung Volume for Different Compression Rates in Various Chest Compression Cycles.

5.6 Conclusion

In conclusion, this chapter aimed to provide insight into the nonlinear and time-dependent characteristics of chest compressions, emphasizing the influence of the viscoelastic properties of the ribcage. The force-deflection curves confirm the presence of residual deflection and hysteresis, highlighting the ribcage's ability to exhibit time-dependent deformations and resist immediate recovery. The comparison with experimental studies further strengthens the validity of our findings. The analysis of displacement at the applied force location reveals a notable residual deflection at the end of the first cycle, followed by minimal increases in subsequent cycles. The disparities in timing between maximum compression depth and peak force underscore the intricate nature of chest compressions due to the ribcage's

viscoelastic properties. The relationship between chest compressions and the deformation of the heart and lungs is evident through the alignment of minimum volume with maximum compression depth. Examining the temporal changes in heart and lung volume indicated a decline in cardiac and thoracic pumping capacity as time progressed. Additionally, the variation in lung volume timing and minimum compression depth calls for additional investigation. Comparing compression rates of 100 and 120 compressions per minute highlights differences in maximum compression depth and residual deflection, with the lower compression rate allowing for deeper compressions. The volume changes in the heart and lungs reveal lower maximum volumes and higher minimum volumes at the rate of 120 compressions per minute, indicating the impact of compression rate on blood circulation and thoracic pressure efficiency. Overall, this chapter sheds light on the complex dynamics of chest compressions and emphasizes the importance of considering viscoelastic properties and compression rates in CPR simulations.

Chapter 6

Conclusion and Future Research Lines

The last section of this dissertation highlights the key findings and main conclusions, emphasizing their importance. It also discusses potential directions for future research.

6.1 Conclusion

In conclusion, this thesis has aimed to enhance the comprehension of the impact of parameters that are often overlooked or difficult to study in clinical and laboratory investigations of CPR. FE models were employed, utilizing open source software, primarily `Code Aster`, to conduct simulations. Realistic anatomical structures and appropriate material properties for thoracic organs were incorporated into these models.

The investigation initially focused on the relationship between compression

depth (ΔY) and maximum rib cage stress with rib cage dimensions. The findings revealed that, for a given compression force (F), achieving greater compression depth is associated with increased rib cage width (W_R) and decreased rib cage depth (L_R) and height (H_R). Consequently, the force required to achieve a target compression depth during CPR decreases with increasing W_R and increases with increasing LR and HR. Most interestingly, it has been found that a fairly good fit of the current predictions can be obtained by using only two quantities based on the rib-cages dimensions, which are the Haller index (HI) and the vertical sagittal cross-area (A_{YZ}). Particularly, a positive correlation between ΔY and HI was observed, indicating that patients with higher HI tend to achieve greater ΔY. Similarly, mechanically assisted CPR at a fixed target ΔY would require less force for patients with higher HI. Furthermore, the results suggest that patients with wider chests (larger W_R) would experience reduced rib stress as a result of compression.

The study also examined the deformation of various thoracic organs during CPR. Although heart size did not significantly impact compression depth or overall thoracic stiffness, the deformation of the heart was found to be substantial, emphasizing its crucial role in CPR mechanics. Lung volume was found to undergo considerable changes due to chest compression, potentially leading to increased thoracic pressure. Moreover, the model with a larger heart exhibited greater changes in lung volume and, consequently, higher thoracic pressure.

The dynamic simulation of CPR provided insights into the complex nature of chest compressions, emphasizing the role of the ribcage's viscoelastic properties. Residual deflection and hysteresis were observed in the force-deflection curves,

indicating the ribcage's time-dependent deformations and resistance to immediate recovery. An initial considerable residual deflection, followed by minimal increases in subsequent cycles was observed. Investigation of the temporal changes in heart and lung volume indicated a decline in cardiac and thoracic pumping capacity as time progressed. Comparing compression rates of 100 and 120 compressions per minute revealed differences in maximum compression depth, with the lower rate enabling deeper compressions. Changes in heart and lung volumes at the higher compression rate suggested an impact on cardiac and thoracic pump potential, with lower maximum volumes and higher minimum volumes observed.

Overall, the employed FE model proved to be a valuable tool for evaluating the influence of different parameters on CPR outcomes and identifying potential avenues for enhancing CPR effectiveness. In summary, this thesis broadens our perspective on the impact of intricate parameters in CPR that are typically overlooked in traditional clinical and laboratory studies. By employing FE models and realistic anatomical structures, this research provides valuable insights into the effects of rib cage dimensions, heart deformation, and lung volume changes during CPR. These findings have the potential to contribute to the advancement of CPR techniques and improve patient outcomes.

6.2 Future research lines

There are several potential avenues for future research in the field of CPR based on the findings and limitations of this study. The following areas are recommended

for further investigation:

1. Inclusion of additional organs: While the current model includes important thoracic organs, there are other non-essential organs, such as the thymus, trachea, shoulders, and arms, that can be incorporated to explore their effects on CPR outcomes. By expanding the model to encompass these organs, a more comprehensive understanding of their contributions to CPR effectiveness can be gained.

2. Investigating the effect of sex: There are notable differences in material properties and organ shape between men and women. Therefore, it is recommended to study the effect of sex on CPR outcomes. By considering these sex-specific factors, a more tailored and effective approach to CPR can be developed.

3. Exploring the impact of age: Age-related changes in material properties and ribcage shape can influence the effectiveness of CPR. Future research should focus on studying the effect of age on CPR outcomes to better understand the unique considerations and adaptations required for different age groups.

Exploring these future research directions will contribute to further advancements in CPR techniques, enhance our understanding of the factors influencing CPR outcomes, and ultimately improve survival rates following CA.

UNIVERSITAT ROVIRA I VIRGILI
NUMERICAL SIMULATION OF CARDIOPULMONARY RESUSCITATION
Jafar Moradicheghamahi

Appendix A

Code Aster Pseudocodes

This section describes implementing the FE model in `Code Aster` open-source software. For clarity, we explained the implementations of pseudocodes step by step i.e.; the descriptions are provided under each box–code.

The extension of the `Code Aster` file is .comm and it begins with the variables involved throughout the problem. The explanation of the code is detailed below the box–code.

A.0.1 Read and Modify the Mesh

```
DEBUT()
MAIL =  LIRE_MAILLAGE(FORMAT = 'MED',
                      UNITE =  20)
                      MAIL =  MODI_MAILLAGE(
                              reuse = MAIL,
                              MAILLAGE = MAIL,
                              ORIE_PEAU_3D =  _F(
                              GROUP_MA =
                              ('presF')))
```

In this portion of the code, the "DEBUT()" function is called to start the code execution. The "LIRE_MAILLAGE" function is used to read the mesh data from a file in 'MED' format, with the file being assigned the Fortran unit LU 20 (Logical Unit 20). The resulting mesh data is stored in the variable 'MAIL'. Then, the "MODI_MAILLAGE" function is applied to modify the mesh. The "ORIE_PEAU_-3D" parameter is used to reorient the meshes of edges, ensuring that their normals are coherent. In this case, the reorientation is performed for the group of elements labeled as 'Force_Area'. The modified mesh is stored back in the 'MAIL' variable for further processing.

A.0.2 Making a FEM from the Mesh

```
MODE =  AFFE_MODELE(AFFE = _F(MODELISATION='3D',
                              PHENOMENE =
                              'MECANIQUE',
                              TOUT =  'OUI'),
                              MAILLAGE =  MAIL)
```

The variable 'MODE' is assigned using the "AFFE_MODELE" keyword. Within this keyword, the "AFFE" parameter is set to specify the modeling aspects, including the "MODELISATION" as '3D' (indicating a 3D model) and the "PHENOMENE" as 'MECANIQUE' (representing the mechanical phenomenon). The "TOUT" parameter is set to 'OUI', which indicates that all components of the model are included. The "MAILLAGE" parameter is assigned as the previously defined mesh variable 'MAIL'.

A.0.3 Defining a Linear Material Properties

```
mater = DEFI_MATERIAU(ELAS=_F(E=Young,
                              NU = NU,
                              AMOR_HYST = ETA,
                              RHO =  DENS))
```

The material properties are defined using the "DEFI_MATERIAU" keyword. Within this keyword, the "ELAS" parameter is specified with the elastic properties.

The Young's modulus (E) is assigned using the variable 'Young', the Poisson's ratio (ν) is assigned using the variable 'NU', the hysteretic damping coefficient (η) is assigned using the variable 'ETA', and the density (ρ) is assigned using the variable 'DENS'.

A.0.4 Defining a non–Linear Elasto–Plastic Material Properties

```
mater = DEFI_MATERIAU(ECRO_LINE=_F(D_SIGM_EPSI=Young_T,
                                   SY = S_Y),
                      (ELAS=_F(E=Young,
                      NU = NU,
                      AMOR_HYST = ETA,
                      RHO =  DENS)))
```

In order to define the elastoplastic properties of osseous tissue in our model, we need to introduce additional parameters beyond those necessary for elastic materials. To accomplish this, we utilize the "ECRO_LINE" keyword, which allows us to specify the stress-strain behavior of the material. Specifically, we must define the tensile yield strength (σ_Y) using the "SY" keyword and the tangent modulus (E_T) using the "D_SIGM_EPSI" keyword.

A.0.5 Assigning Material Properties to the Elements

```
MATE =  AFFE_MATERIAU(AFFE = _F(GROUP_MA = 'Part1',
                                MATER=  mater),
                                MAILLAGE =  MAIL)
```

The material properties are assigned to a specific part of the mesh named 'Part1' using the "AFFE_MATERIAU" keyword. The "GROUP_MA" parameter is set to 'Part1' to indicate the targeted group. The "MATER" parameter is assigned the previously defined material properties variable 'mater'. Lastly, the "MAILLAGE" parameter is set to the mesh variable 'MAIL'.

A.0.6 Stepping for the Solution

```
TPS =  DEFI_LIST_REEL(DEBUT=0.0,
INTERVALLE = _F(JUSQU_A = 0.6,
                PAS=  0.05))
llista =  DEFI_LIST_INST(DEFI_LIST = _F(LIST_INST=TPS,
                                        PAS_MAXI = 0.01,
                                        PAS_MINI = 1e-6),
                                        METHODE =  'AUTO')
```

The variable 'TPS' is defined as a list of real numbers using the "DEFI_LIST_REEL" keyword. The "DEBUT" parameter is set to 0.0, indicating the starting

value of the list. The "INTERVALLE" parameter is assigned with the "JUSQU_-A" value of 0.6, indicating the end value of the list, and the "PAS" value of 0.05, indicating the interval between consecutive values.

The variable 'llista' is defined as a list of time instances using the "DEFI_LIST_-INST" keyword. Within this keyword, the "DEFI_LIST" parameter is specified with the "LIST_INST" value of 'TPS', representing the list of time instances. The "PAS_MAXI" parameter is set to 0.01, indicating the maximum time step size and the "PAS_MINI" parameter is set to 1e-6, indicating the minimum time step size. The "METHODE" parameter is set to 'AUTO', indicating the automatic time stepping method is used. If the simulation fails to converge at the given time step, the code automatically reduces the time step to a number between "PAS_MINI" and "PAS_MAXI".

A.0.7 Definition of Function for Zero Displacement

```
formule0 = FORMULE(NOM_PARA='INST',
                   VALE= '(0.0)')
```

We establish a function that represents the displacement of components with fixed boundary conditions at every time step. This function is utilized in the code sections where boundary conditions are defined. The variable 'formule0' is created as a formula using the "FORMULE" keyword. Within this keyword, the "NOM_PARA" parameter is set to 'INST', which signifies the time variable (t). The "VALE" parameter is given the value '(0.0)', indicating that the formula yields 0.0 for all instances of time.

A.0.8 The Level of Applied Force

```
formule = FORMULE(NOM_PARA='INST',
                  VALE= '(1000*INST)')
```

In our simulations, we employed 12 distinct levels of applied force. This section of the code utilizes a function defined as 'formule' to determine the applied force based on the time variable ('INST'). The function is defined as '(1000*INST)', indicating that the applied force increases linearly with time, scaled by a factor of 1000. The lowest applied force of 50 N is assigned at 0.05 seconds, while the highest force level of 600 N is associated with 0.6 seconds.

A.0.9 Applying Boundary Conditions

```
grav = AFFE_CHAR_MECA_F(DDL_IMPO=(_F(DX= formule0,
                                     DY = formule0,
                                     DZ = formule0,
                                GROUP_MA=('Fixed')),
                        FORCE_FACE = _F(FY=formule,
                        GROUP_Ma= ('Force_Area', )),
                        MODELE = MODE)
```

We utilize the "AFFE_CHAR_MECA_F" keyword to establish the boundary conditions and mechanical characteristics of the system. The "DDL_IMPO" parameter within this keyword specifies the degrees of freedom (DOF) to be fixed

for the components with fixed boundary conditions. In this case, the displacement values in the global reference of the mesh definition for the DX, DY, and DZ directions are set using the corresponding formulas defined in 'formule0'. This ensures that the components' displacements are fixed in the X, Y, and Z directions. The "GROUP_MA" parameter is set to 'Fixed' to specify the parts with fixed boundary conditions.

We utilize the "FORCE_FACE" keyword to apply forces on specific areas. Within this keyword, the "FY" parameter is defined using the 'formule' function, indicating the force component in the Y direction. The "GROUP_Ma" parameter is set to 'Force_Area', specifying the parts where the force is applied.

The resulting mechanical characteristics and boundary conditions are stored in the 'grav' variable, which is assigned the result of the "AFFE_CHAR_MECA_F" keyword. Finally, the "MODELE" parameter is set to 'MODE' to specify the specific model used in the analysis.

A.0.10 Solving a Problem

```
RESU = STAT_NON_LINE(ARCHIVAGE=_F(LIST_INST = TPS),
                     CHAM_MATER = MATE,
                     COMPORTEMENT = _F(
                     DEFORMATION = 'SIMO_MIEHE',
                     RELATION= 'VMIS_ISOT_LINE',
                     RESI_INTE_RELA = 1e-06,),
                     _F(RELATION = 'ELAS',
                     GROUP_MA = ('ELASTIC_PART'))
                     CONVERGENCE = _F(
                     ITER_GLOB_MAXI = 10,
                     RESI_GLOB_RELA = 0.0001),
                     EXCIT = _F(CHARGE = grav),
                     INCREMENT = _F(
                     LIST_INST = llista),
                     MODELE = MODE,
                     NEWTON = _F(
                     MATRICE = 'TANGENTE',
                     PAS_MINI_ELAS = 1e-05,
                     PREDICTION = 'TANGENTE',
                     REAC_ITER = 1,)
                     SOLVEUR = _F(METHODE = 'MUMPS',
                     NPREC = 8,))
```

In this section of the `Code Aster` code, a nonlinear static analysis is performed, and the results are stored in the variable 'RESU'. The "ARCHIVAGE" parameter is used to store results at specific time instances listed in the 'TPS' variable. The material properties are defined using the "CHAM_MATER" keyword and the 'MATE' variable. The mechanical behavior model for deformation is set as "SIMO_MIEHE", and the relationship between stress and strain is defined as "VMIS_ISOT_LINE" with an internal residual tolerance of 1e-06. Firstly, we utilize the keyword "VMIS_ISOT_LINE" to establish von Mises elastoplastic characteristics with linear isotropic hardening across all components. Subsequently, we employ the "ELAS" keyword to specify that the particular component exhibits purely elastic behavior. Convergence criteria are set with "ITER_GLOB_MAXI" as the maximum number of global iterations and "RESI_GLOB_RELA" as the relative global residual tolerance. The system is excited with the boundary conditions defined in the 'grav' variable. The analysis is performed in increments defined by the time instances listed in the 'llista' variable. The finite element model is defined by the 'MODE' variable. The Newton-Raphson solver options are specified using the "NEWTON" keyword with "MATRICE" for the 'TANGENTE' matrix, "PAS_MINI_ELAS" for the minimum elastic time step, "PREDICTION" for the type of prediction, and "REAC_ITER" for the number of reaction iterations. The solver method 'MUMPS' is selected, with "NPREC" specifying the number of preconditioning steps.

A.0.11 Calculating Results

```
RESU = CALC_CHAMP(reuse = RESU,
                  CONTRAINTE = ('SIGM_ELNO',
                  'SIGM_NOEU', 'SIGM_ELGA'),
                   CRITERES = ('SIEQ_ELNO',
                  'SIEQ_NOEU'),
                   DEFORMATION = ('EPSG_ELNO',
                   'EPSG_NOEU', 'EPSI_NOEU'),
                   FORCE = ('FORC_NODA',
                  'REAC_NODA'),
                   RESULTAT = RESU)
```

It is necessary to indicate the stress and deformation field for post–processing. In this part of the code, the 'RESU' variable is updated using the "CALC_CHAMP" keyword to calculate and store various field quantities based on the existing results. Within this keyword, the "CONTRAINTE" parameter is used to specify the stress components to be calculated, including 'SIGM_ELNO' for element nodal stresses, 'SIGM_NOEU' for nodal stresses, and 'SIGM_ELGA' for element Gauss stresses. The "CRITERES" parameter is employed to calculate strain energy quantities, namely 'SIEQ_ELNO' for equivalent element nodal strain energy and 'SIEQ_NOEU' for equivalent nodal strain energy. The "DEFORMATION" parameter is used to calculate deformation-related quantities such as 'EPSG_ELNO' for element nodal plastic strains, 'EPSG_NOEU' for nodal plastic strains, and 'EPSI_NOEU' for nodal elastic strains. Furthermore, the "FORCE" parameter includes 'FORC_NODA' for nodal forces and 'REAC_NODA' for nodal reactions. Lastly,

the "RESULTAT" parameter is set to 'RESU' to indicate that the calculated quantities should be stored in the same results variable. By utilizing the "CALC_-CHAMP" keyword with these specified parameters, additional field quantities related to stresses, strains, deformations, forces, and reactions are calculated and appended to the existing results stored in the 'RESU' variable.

A.0.12 Printing Results for Graphical Viewing

```
IMPR_RESU(FORMAT = 'MED',
                RESU = _F(NOM_CHAM = ('DEPL',
                'SIGM_NOEU', 'EPSG_NOEU'),
                RESULTAT = RESU,
                TOUT = 'OUI',
                TOUT_CMP = 'OUI'),
                UNITE = 80)
FIN()
```

To output the results in a desired format, we use the "IMPR_RESU" keyword. Within this keyword, we specify the format as 'MED' and define the field quantities we want to include in the output. The "NOM_CHAM" parameter is used to select the desired field quantities, such as displacements ('DEPL'), nodal stresses ('SIGM_NOEU'), and nodal plastic strains ('EPSG_NOEU'). The "RESULTAT" parameter is set to 'RESU' to indicate that we want to output the results stored in the 'RESU' variable. By setting "TOUT" and "TOUT_CMP" parameters to 'OUI', we

ensure that all components and all computation points are included in the output. The "UNITE" parameter is set to 80 to specify the output unit. Finally, we conclude the code with the "FIN()" keyword.

Finally, the results we want to be displayed graphically in the Post-Processing or `Para views` modules of `Salome-Meca` are then placed in a .med file. We save the results in .rmed file which has a unit number 80.

Bibliography

[1] Saeed Alqahtani et al. “Changes in the incidence of out-of-hospital cardiac arrest: Differences between cardiac and non-cardiac aetiologies”. en. In: *Resuscitation* 155 (Oct. 2020), pp. 125–133.

[2] Amy E. Peden et al. “Fatal river drowning: the identification of research gaps through a systematic literature review”. In: *Injury Prevention* 22.3 (2016). ISBN: 1353-8047 Publisher: BMJ Publishing Group Ltd, pp. 202–209.

[3] Ellen Kramarow et al. “Food-related choking deaths among the elderly”. eng. In: *Injury Prevention: Journal of the International Society for Child and Adolescent Injury Prevention* 20.3 (June 2014), pp. 200–203.

[4] Alaaddin M. Salih et al. “Airway foreign bodies: A critical review for a common pediatric emergency”. eng. In: *World Journal of Emergency Medicine* 7.1 (2016), pp. 5–12.

[5] European Monitoring Centre for Drugs and Drug Addiction. *European drug report 2020 : trends and developments*. Publications Office of the European Union, 2020.

[6] Nana Wilson et al. “Drug and opioid-involved overdose deaths—United States, 2017–2018”. In: *Morbidity and Mortality Weekly Report* 69.11 (2020). Publisher: Centers for Disease Control and Prevention, p. 290.

[7] C.C. Evans et al. "Prehospital traumatic cardiac arrest: management and outcomes from the Resuscitation Outcomes Consortium Epistry-Trauma and PROPHET registries". In: *The journal of trauma and acute care surgery* 81.2 (Aug. 2016), pp. 285–293.

[8] P Viji et al. "Assess the effect of Cardiopulmonary Resuscitation Demonstration on Knowledge, Attitude and Practice among Relatives of Cardiac Patients". In: *Madridge J Nurs* 3.2 (2018), pp. 124–126.

[9] R. L. Taw. "Dr. Friedrich Maass: 100th anniversary of "new" CPR". In: *Clin Cardiol* 14.12 (1991), pp. 1000–2.

[10] Robert P. Sands et al. "An Inventive Mind : The Career of James O. Elam, M.D. (1918–1995)". In: *Anesthesiology* 88.4 (Apr. 1998), pp. 1107–1112.

[11] W. B. Kouwenhoven et al. "Closed-chest cardiac massage". In: *JAMA* 173.10 (July 1960), pp. 1064–1067.

[12] "Cardiopulmonary Resuscitation: Statement by the Ad Hoc Committee on Cardiopulmonary Resuscitation of the Division of Medical Sciences, National Academy of Sciences—National Research Council". In: *JAMA* 198.4 (Oct. 1966), pp. 372–379.

[13] ECC Committee, Subcommittees and Task Forces of the American Heart Association. "2005 American Heart Association Guidelines for Cardiopulmonary Resuscitation and Emergency Cardiovascular Care". eng. In: *Circulation* 112.24 Suppl (Dec. 2005), pp. IV1–203.

[14] John M. Field et al. "Part 1: Executive Summary: 2010 American Heart Association Guidelines for Cardiopulmonary Resuscitation and Emergency Cardiovascular Care". en. In: *Circulation* 122.18_suppl_3 (Nov. 2010).

[15] Douglas Chamberlain et al. "Guidelines for advanced life support: A statement by the Advanced Life Support Working Party of the European Resuscitation Council, 1992". en. In: *Resuscitation* 24.2 (Nov. 1992), pp. 111–121.

[16] Theresa M. Olasveengen et al. "European resuscitation council guidelines 2021: basic life support". In: *Resuscitation* 161 (2021). ISBN: 0300-9572 Publisher: Elsevier, pp. 98–114.

[17] Ashish R. Panchal et al. "Part 3: Adult Basic and Advanced Life Support: 2020 American Heart Association Guidelines for Cardiopulmonary Resuscitation and Emergency Cardiovascular Care". eng. In: *Circulation* 142.16_-suppl_2 (Oct. 2020), S366–S468.

[18] Elham Navab et al. "Predictors of Out of Hospital Cardiac Arrest Outcomes in Pre-Hospital Settings; a Retrospective Cross-sectional Study". eng. In: *Archives of Academic Emergency Medicine* 7.1 (2019), p. 36.

[19] Aspasia Deliliga et al. "Cardiopulmonary resuscitation (CPR) complications encountered in forensic autopsy cases". In: *BMC Emergency Medicine* 19 (Feb. 2019), p. 23.

[20] Shijiao Yan et al. "The global survival rate among adult out-of-hospital cardiac arrest patients who received cardiopulmonary resuscitation: a systematic review and meta-analysis". In: *Critical Care* 24 (Feb. 2020), p. 61.

[21] Kristy B. Arbogast et al. "Anterior-Posterior Thoracic Force-Deflection Characteristics Measured During Cardiopulmonary Resuscitation: Comparison to Post-Mortem Human Subject Data". English. In: *Stapp Car Crash Journal* 50 (Nov. 2006). Num Pages: 15 Place: Ann Arbor, United States Publisher: The Stapp Association, pp. 131–45.

[22] Christian Vaillancourt et al. "A survey of attitudes and factors associated with successful cardiopulmonary resuscitation (CPR) knowledge transfer in an older population most likely to witness cardiac arrest: design and methodology". In: *BMC Emergency Medicine* 8.1 (Nov. 2008), p. 13.

[23] H. Duhem et al. "Cadaver models for cardiac arrest: A systematic review and perspectives". en. In: *Resuscitation* 143 (Oct. 2019), pp. 68–76.

[24] M. Blondel et al. "How can we study cardiopulmonary resuscitation and cardiac arrest in animals: a review". In: *J Dairy Vet Anim Res* 3.2 (2016), pp. 37–41.

[25] David Weidenauer et al. "The impact of cardiopulmonary resuscitation (CPR) manikin chest stiffness on motivation and CPR performance measures in children undergoing CPR training—A prospective, randomized, single-blind, controlled trial". In: *PLoS ONE* 13.8 (Aug. 2018), e0202430.

[26] Hildigunnur Katrínardóttir. *Finite Element Modeling of Chest Compressions in CPR*. eng. 2017.

[27] Sandeep Kumar Parashar et al. "A review on application of finite element modelling in bone biomechanics". en. In: *Perspectives in Science*. Recent Trends in Engineering and Material Sciences 8 (Sept. 2016), pp. 696–698.

[28] Lars W. Andersen et al. "In-hospital cardiac arrest: a review". In: *Jama* 321.12 (2019). ISBN: 0098-7484 Publisher: American Medical Association, pp. 1200–1210.

[29] Jan-Thorsten Gräsner et al. "EuReCa ONE27 Nations, ONE Europe, ONE Registry: A prospective one month analysis of out-of-hospital cardiac arrest outcomes in 27 countries in Europe". en. In: *Resuscitation* 105 (Aug. 2016), pp. 188–195.

[30] Masashi Okubo et al. "Variation in Survival After Out-of-Hospital Cardiac Arrest Between Emergency Medical Services Agencies". eng. In: *JAMA cardiology* 3.10 (Oct. 2018), pp. 989–999.

[31] Ingela Hasselqvist-Ax et al. "Early cardiopulmonary resuscitation in out-of-hospital cardiac arrest". In: *New England Journal of Medicine* 372.24 (2015). ISBN: 0028-4793 Publisher: Mass Medical Soc, pp. 2307–2315.

[32] Charles F. Babbs et al. "Relationship of blood pressure and flow during CPR to chest compression amplitude: evidence for an effective compression threshold". In: *Annals of emergency medicine* 12.9 (1983). ISBN: 0196-0644 Publisher: Elsevier, pp. 527–532.

[33] Anthony J. Handley. "Press hard – But perhaps not too hard". English. In: *Resuscitation* 85.2 (Feb. 2014). Publisher: Elsevier, pp. 153–154.

[34] Ian G. Stiell et al. "What Is the Optimal Chest Compression Depth During Out-of-Hospital Cardiac Arrest Resuscitation of Adult Patients?" In: *Circulation* 130.22 (Nov. 2014). Publisher: American Heart Association, pp. 1962–1970.

[35] Gavin D. Perkins et al. "European Resuscitation Council Guidelines for Resuscitation 2015: Section 2. Adult basic life support and automated external defibrillation". In: *Resuscitation* 95 (2015). ISBN: 0300-9572 Publisher: Elsevier, pp. 81–99.

[36] Sue Duval et al. "Optimal Combination of Compression Rate and Depth During Cardiopulmonary Resuscitation for Functionally Favorable Survival". In: *JAMA Cardiology* 4.9 (Sept. 2019), pp. 900–908.

[37] Bush, Colleen M. et al. "Pediatric injuries from cardiopulmonary resuscitation". In: *Annals of Emergency Medicine* 28.1 (1996). Number: 1, pp. 40–44.

[38] Azeli, Youcef et al. "Serious injuries secondary to cardiopulmonary resuscitation: incidence and associated factors". In: *Emergencias* 31 (2019), pp. 327–334.

[39] A. C. Miller et al. "A systematic review and pooled analysis of CPR–associated cardiovascular and thoracic injuries". In: *Resuscitation* 85.6 (2014). Number: 6 Publisher: Elsevier, pp. 724–61.

[40] Youcef Azeli et al. "Chest wall mechanics during mechanical chest compression and its relationship to CPR-related injuries and survival". en. In: *Resuscitation Plus* 10 (June 2022), p. 100242.

[41] Jiri Karasek et al. "CPR-related injuries after non-traumatic out-of-hospital cardiac arrest: Survivors versus non-survivors". en. In: *Resuscitation* 171 (Feb. 2022), pp. 90–95.

[42] Youcef Azeli et al. "Understanding the Adverse Hemodynamic Effects of Serious Thoracic Injuries During Cardiopulmonary Resuscitation: A Review and Approach Based on the Campbell Diagram". In: *Frontiers in Physiology* 10 (2019).

[43] Jin Ho Beom et al. "Investigation of complications secondary to chest compressions before and after the 2010 cardiopulmonary resuscitation guideline changes by using multi-detector computed tomography: a retrospective study". en. In: *Scandinavian Journal of Trauma, Resuscitation and Emergency Medicine* 25.1 (Jan. 2017), p. 8.

[44] John M. Boe et al. "Mechanics of CPR Performed with the Patient on a Soft Bed Versus a Hard Surface". In: *Academic emergency medicine* (1999).

[45] Helena Jäntti et al. "Quality of cardiopulmonary resuscitation on manikins: on the floor and in the bed". In: *Acta anaesthesiologica scandinavica* 53.9 (2009). ISBN: 0001-5172 Publisher: Wiley Online Library, pp. 1131–1137.

[46] Akira Nishisaki et al. "Backboards are important when chest compressions are provided on a soft mattress". In: *Resuscitation* 83.8 (2012). ISBN: 0300-9572 Publisher: Elsevier, pp. 1013–1020.

[47] Gerrit J. Noordergraaf et al. "The impact of compliant surfaces on in-hospital chest compressions: effects of common mattresses and a backboard". In: *Resuscitation* 80.5 (2009). ISBN: 0300-9572 Publisher: Elsevier, pp. 546–552.

[48] Gavin D. Perkins et al. "Do different mattresses affect the quality of cardiopulmonary resuscitation?" In: *Intensive care medicine* 29 (2003). ISBN: 0342-4642 Publisher: Springer, pp. 2330–2335.

[49] Gavin D. Perkins et al. "Effects of a backboard, bed height, and operator position on compression depth during simulated resuscitation". In: *Intensive care medicine* 32 (2006). ISBN: 0342-4642 Publisher: Springer, pp. 1632–1635.

[50] Michael Tweed et al. "The effect of differing support surfaces on the efficacy of chest compressions using a resuscitation manikin model". In: *Resuscitation* 51.2 (2001). ISBN: 0300-9572 Publisher: Elsevier, pp. 179–183.

[51] Gavin D. Perkins et al. "Compression feedback devices over estimate chest compression depth when performed on a bed". In: *Resuscitation* 80.1 (2009). ISBN: 0300-9572 Publisher: Elsevier, pp. 79–82.

[52] Dana Niles et al. "Leaning is common during in-hospital pediatric CPR, and decreased with automated corrective feedback". In: *Resuscitation* 80.5 (2009). ISBN: 0300-9572 Publisher: Elsevier, pp. 553–557.

[53] Akira Nishisaki et al. "Effect of mattress deflection on CPR quality assessment for older children and adolescents". In: *Resuscitation* 80.5 (2009). ISBN: 0300-9572 Publisher: Elsevier, pp. 540–545.

[54] Mario Suazo et al. "Biomechanical response of human rib cage to cardiopulmonary resuscitation maneuvers: Effects of the compression location". en. In: *International Journal for Numerical Methods in Biomedical Engineering* 38.4 (2022). _eprint: https://onlinelibrary.wiley.com/doi/pdf/10.1002/cnm.3585, e3585.

[55] Theresa M. Olasveengen et al. "Adult Basic Life Support: 2020 International Consensus on Cardiopulmonary Resuscitation and Emergency Cardiovascular Care Science With Treatment Recommendations". eng. In: *Circulation* 142.16_suppl_1 (Oct. 2020), S41–S91.

[56] Kyoung-Jun Song et al. "2020 Korean guidelines for cardiopulmonary resuscitation. Part 3. adult basic life support". In: *Clinical and Experimental*

Emergency Medicine 8.Suppl (2021). Publisher: The Korean Society of Emergency Medicine, S15.

[57] Kenton L. Anderson et al. "Left ventricular compressions improve hemodynamics in a swine model of out-of-hospital cardiac arrest". In: *Prehospital Emergency Care* 21.2 (2017). ISBN: 1090-3127 Publisher: Taylor & Francis, pp. 272–280.

[58] Sung Oh Hwang et al. "Compression of the left ventricular outflow tract during cardiopulmonary resuscitation". In: *Academic Emergency Medicine* 16.10 (2009). ISBN: 1069-6563 Publisher: Wiley Online Library, pp. 928–933.

[59] Athanasios Chalkias et al. "Personalized physiology-guided resuscitation in highly monitored patients with cardiac arrest—the PERSEUS resuscitation protocol". In: *Heart failure reviews* 24 (2019). ISBN: 1382-4147 Publisher: Springer, pp. 473–480.

[60] Eric Qvigstad et al. "Clinical pilot study of different hand positions during manual chest compressions monitored with capnography". In: *Resuscitation* 84.9 (2013). ISBN: 0300-9572 Publisher: Elsevier, pp. 1203–1207.

[61] Roman Skulec et al. "Correlation between end-tidal carbon dioxide and the degree of compression of heart cavities measured by transthoracic echocardiography during cardiopulmonary resuscitation for out-of-hospital cardiac arrest". In: *Critical Care* 23.1 (2019). ISBN: 1364-8535 Publisher: BioMed Central, pp. 1–10.

[62] International Liaison Committee on Resuscitation. "2005 International consensus on cardiopulmonary resuscitation and emergency cardiovascular

care science with treatment recommendations". In: *Circulation* 112 (2005), pp. III1–III136.

[63] M Baubin et al. "Chest injuries after active compression–decompression cardiopulmonary resuscitation (ACD-CPR) in cadavers". en. In: *Resuscitation* 43.1 (Dec. 1999), pp. 9–15.

[64] Binhui Jiang et al. "Application of an anatomically-detailed finite element thorax model to investigate pediatric cardiopulmonary resuscitation techniques on hard bed". en. In: *Computers in Biology and Medicine* 52 (Sept. 2014), pp. 28–34.

[65] D. Smekal et al. "CPR-related injuries after manual or mechanical chest compressions with the LUCAS™ device: A multicentre study of victims after unsuccessful resuscitation". en. In: *Resuscitation* 85.12 (Dec. 2014), pp. 1708–1712.

[66] Ioanna Galatianou et al. "Body mass index and outcome of out-of-hospital cardiac arrest patients not treated by targeted temperature management". en. In: *The American Journal of Emergency Medicine* 35.9 (Sept. 2017), pp. 1247–1251.

[67] Heekyung Lee et al. "Retrospective Study Using Computed Tomography to Compare Sufficient Chest Compression Depth for Cardiopulmonary Resuscitation in Obese Patients". In: *Journal of the American Heart Association* 8.23 (Dec. 2019). Publisher: American Heart Association, e013948.

[68] Sayna Matinrazm et al. "Effect of body mass index on survival after sudden cardiac arrest". In: *Clinical Cardiology* 41.1 (Jan. 2018). Publisher: John Wiley & Sons, Ltd, pp. 46–50.

[69] Chih-Hung Wang et al. "Associations between body size and outcomes of adult in-hospital cardiac arrest: A retrospective cohort study". en. In: *Resuscitation* 130 (Sept. 2018), pp. 67–72.

[70] Nihat Mujdat Hokenek et al. "Effect of Differences in Thorax Volume and Dimensions on CPR-related Injuries." In: *Trauma.* 10118 (2021).

[71] Tuba Betül Ümit et al. "Relationship between measures of thoracic diameter and cardiopulmonary resuscitation-induced thoracoabdominal injury". In: *Revista da Associação Médica Brasileira* 68 (2022). ISBN: 0104-4230 Publisher: SciELO Brasil, pp. 1470–1475.

[72] Marios Georgiou et al. "Systematic review of the mechanisms driving effective blood flow during adult CPR". English. In: *Resuscitation* 85.11 (Nov. 2014). Publisher: Elsevier, pp. 1586–1593.

[73] Jerry P. Nolan. "What's new in the management of cardiac arrest?" en. In: *Intensive Care Medicine* 39.7 (July 2013), pp. 1211–1213.

[74] Pinming Liu et al. "Pump models assessed by transesophageal echocardiography during cardiopulmonary resuscitation". In: *Chinese medical journal* 115.03 (2002). ISBN: 0366-6999 Publisher: Chinese Medical Journals Publishing House Co., Ltd. 42 Dongsi Xidajie …, pp. 359–363.

[75] Anatol Prinzing et al. "Cardiopulmonary resuscitation using electrically driven devices: a review". In: *Journal of Thoracic Disease* 7.10 (2015). Publisher: AME Publications, E459.

[76] Simone Cipani et al. "Blood flow maintenance by cardiac massage during cardiopulmonary resuscitation: Classical theories, newer hypotheses, and

clinical utility of mechanical devices". In: *Journal of the Intensive Care Society* 20.1 (Feb. 2019), pp. 2–10.

[77] Emmanuel Charbonney et al. "Ventilation during cardiopulmonary resuscitation: what have we learned from models?" In: *Respiratory Care* 64.9 (2019). ISBN: 0020-1324 Publisher: Respiratory Care, pp. 1132–1138.

[78] Binhui Jiang et al. *Experimental validation of pediatric thorax finite element model under dynamic loading condition and analysis of injury*. Tech. rep. ISBN: 0148-7191. SAE Technical Paper, 2013.

[79] Johan Iraeus et al. "Generic finite element models of human ribs, developed and validated for stiffness and strain prediction–To be used in rib fracture risk evaluation for the human population in vehicle crashes". In: *Journal of the Mechanical Behavior of Biomedical Materials* 106 (2020). ISBN: 1751-6161 Publisher: Elsevier, p. 103742.

[80] Matthew Kindig et al. "Effect of intercostal muscle and costovertebral joint material properties on human ribcage stiffness and kinematics". In: *Computer Methods in Biomechanics and Biomedical Engineering* 18.5 (2015). ISBN: 1025-5842 Publisher: Taylor & Francis, pp. 556–570.

[81] David Poulard et al. "Thoracic response targets for a computational model: a hierarchical approach to assess the biofidelity of a 50th-percentile occupant male finite element model". In: *Journal of the mechanical behavior of biomedical materials* 45 (2015). ISBN: 1751-6161 Publisher: Elsevier, pp. 45–64.

[82] Samantha L. Schoell et al. "Age– and Sex–Specific Thorax Finite Element Model Development and Simulation". In: *Traffic Injury Prevention* 16.SUPPL. 1 (2015). Number: SUPPL. 1 Publisher: Taylor & Francis, pp. 557–565.

[83] Nobutaka Mitsuhashi et al. "BodyParts3D: 3D structure database for anatomical concepts". In: *Nucleic acids research* 37.suppl_1 (2009). ISBN: 1362-4962 Publisher: Oxford University Press, pp. D782–D785.

[84] CGAL. *The Computational Geometry Algorithms Library*. 2017.

[85] Christophe Geuzaine et al. *Gmsh. A three–dimensional finite element mesh generator with built–in pre– and post–processing facilities*. 2020.

[86] EDF R&D. *Code_Aster, Structures and Thermomechanics Analysis for Studies and Research*. 2018.

[87] Eduardo Baldassari Rebeis et al. "Anthropometric index for pectus excavatum". In: *Clinics* 62 (2007). ISBN: 1807-5932 Publisher: SciELO Brasil, pp. 599–606.

[88] James E. Archer et al. "The measurement of the normal thorax using the Haller index methodology at multiple vertebral levels". In: *Journal of anatomy* 229.4 (2016). ISBN: 0021-8782 Publisher: Wiley Online Library, pp. 577–581.

[89] Jun-Zhao Liu et al. "The effects of thoracic cage dimension and chest subcutaneous adipose tissue on outcomes of adults with in-hospital cardiac arrest: A retrospective study". In: *Resuscitation* 141 (2019). ISBN: 0300-9572 Publisher: Elsevier, pp. 151–157.

[90] Louis-Philippe Laurin et al. "Sternum length and rib cage dimensions compared with bodily proportions in adults with cystic fibrosis". In: *Canadian respiratory journal* 19.3 (2012). ISBN: 1198-2241 Publisher: Hindawi, pp. 196–200.

[91] Hamish M Aitken-Buck et al. "Estimating heart mass from heart volume as measured from post-mortem computed tomography". In: *Forensic Science, Medicine and Pathology* 18.3 (2022), pp. 333–342.

[92] Andreas Fuchs et al. "Normal values of left ventricular mass and cardiac chamber volumes assessed by 320-detector computed tomography angiography in the Copenhagen General Population Study". In: *European Heart Journal-Cardiovascular Imaging* 17.9 (2016), pp. 1009–1017.

[93] Braj Bhushan Prasad. "The theory of continuum and elasto-plastic materials". In: (2018).

[94] PH Mott et al. "Limits to Poisson's ratio in isotropic materials". In: *Physical review B* 80.13 (2009), p. 132104.

[95] Attila Kossa. "Exact stress integration schemes for elastoplasticity". PhD thesis. Budapest University of Technology and Economics (Hungary), 2015.

[96] William Prager et al. *Theory of perfectly plastic solids*. Dover Publications, 1968.

[97] Rodney Hill. *The mathematical theory of plasticity*. Vol. 11. Oxford university press, 1998.

[98] Fionn Dunne et al. *Introduction to computational plasticity*. OUP Oxford, 2005.

[99] Forman, J. L. "The structural characteristics of the costal cartilage: the roles of calcification and the perichondrium, and the representation of the costal cartilage in finite element models of the human body". PhD thesis. University of Virginia School of Engineering, Applied Science. Department of Mechanical, and Aerospace Engineering, 2009.

[100] W. F. McCormick. "Mineralization of the costal cartilages as an indicator of age: preliminary observations." In: *Journal of forensic sciences* 25.4 (1980). ISBN: 0022-1198, pp. 736–741.

[101] Jason L. Forman et al. "The effect of calcification on the structural mechanics of the costal cartilage". In: *Computer methods in biomechanics and biomedical engineering* 17.2 (2014). ISBN: 1025-5842 Publisher: Taylor & Francis, pp. 94–107.

[102] Won-Jin Yi et al. "Direct measurement of trabecular bone anisotropy using directional fractal dimension and principal axes of inertia". In: *Oral Surgery, Oral Medicine, Oral Pathology, Oral Radiology, and Endodontology* 104.1 (2007). ISBN: 1079-2104 Publisher: Elsevier, pp. 110–116.

[103] Isabel S. Maggiano et al. "Three-dimensional reconstruction of Haversian systems in human cortical bone using synchrotron radiation-based micro-CT: morphology and quantification of branching and transverse connections across age". In: *Journal of anatomy* 228.5 (2016). ISBN: 0021-8782 Publisher: Wiley Online Library, pp. 719–732.

[104] Ilaria Toniolo et al. "Anisotropic computational modelling of bony structures from CT data: An almost automatic procedure". In: *Computer methods and programs in biomedicine* 189 (2020). ISBN: 0169-2607 Publisher: Elsevier, p. 105319.

[105] Waltraud Baier et al. "Micro-CT for the examination of paediatric rib injuries: A case series". In: *Forensic Science International* 325 (2021). ISBN: 0379-0738 Publisher: Elsevier, p. 110789.

[106] Koichi Hashiguchi. *Elastoplasticity Theory*. en. Vol. 69. Lecture Notes in Applied and Computational Mechanics. Berlin, Heidelberg: Springer Berlin Heidelberg, 2014.

[107] Heng Xiao et al. "Elastoplasticity beyond small deformations". In: *Acta mechanica* 182.1-2 (2006). ISBN: 0001-5970 Publisher: Springer, pp. 31–111.

[108] Matthew Kindig et al. "Biomechanical response of ribs under quasistatic frontal loading". In: *Traffic injury prevention* 12.4 (2011). ISBN: 1538-9588 Publisher: Taylor & Francis, pp. 377–387.

[109] Beesems, Stefanie G. et al. "Force and depth of mechanical chest compressions and their relation to chest height and gender in an out-of-hospital setting". In: *Resuscitation* 91 (2015), pp. 67–72.

[110] C. F. Guimarães et al. "The stiffness of living tissues and its implications for tissue engineering". In: *Nature Reviews Materials* 5.5 (2020). Number: 5, pp. 351–370.

[111] Gurpreet Singh et al. "Mechanical properties of whole-body soft human tissues: A review". In: *Biomedical Materials* 16.6 (2021), p. 062004.

[112] Felipe Concha et al. "Micromechanical model of lung parenchyma hyperelasticity". In: *Journal of the Mechanics and Physics of Solids* 112 (2018), pp. 126–144.

[113] Ibrahim J Domian et al. "On materials for cardiac tissue engineering". In: *Advanced Healthcare Materials* 6.2 (2017), p. 1600768.

[114] Ramona Emig et al. "Passive myocardial mechanical properties: meaning, measurement, models". In: *Biophysical Reviews* (2021), pp. 1–24.

[115] Amelia Pickard et al. "Radiological assessment of the adult chest: implications for chest compressions". In: *Resuscitation* 71.3 (2006). ISBN: 0300-9572 Publisher: Elsevier, pp. 387–390.

[116] Anthony E Armenàkas. *Advanced mechanics of materials and applied elasticity*. CRC Press, 2016.

[117] J.A. Werner et al. "Visualization of cardiac valve motion in man during external chest compression using two-dimensional echocardiography. Implications regarding the mechanism of blood flow". English. In: *Circulation* 63.6 I (1981), pp. 1417–1421.

[118] Athanasios Chalkias et al. "Timing positive-pressure ventilation during chest compression: the key to improving the thoracic pump?" In: *European Heart Journal. Acute Cardiovascular Care* 4.1 (Feb. 2015), pp. 24–27.

[119] Joseph E. Cavanaugh et al. "The Akaike information criterion: Background, derivation, properties, application, interpretation, and refinements". In: *Wiley Interdisciplinary Reviews: Computational Statistics* 11.3 (2019). ISBN: 1939-5108 Publisher: Wiley Online Library, e1460.

[120] Youcef Azeli et al. "Serious injuries secondary to cardiopulmonary resuscitation: incidence and associated factors". In: *Emergencias* 31.5 (2019), pp. 327–334.

[121] Kralj, Eduard et al. "Frequency and number of resuscitation related rib and sternum fractures are higher than generally considered". In: *Resuscitation* 93 (2015), pp. 136–141.

[122] Robert Sebastian Hoke et al. "Skeletal chest injuries secondary to cardiopulmonary resuscitation". In: *Resuscitation* 63.3 (2004). ISBN: 0300-9572 Publisher: Elsevier, pp. 327–338.

[123] Sven A. Holcombe et al. "The effect of age and demographics on rib shape". In: *Journal of anatomy* 231.2 (2017). ISBN: 0021-8782 Publisher: Wiley Online Library, pp. 229–247.

[124] Francis S. Gayzik et al. "Quantification of age-related shape change of the human rib cage through geometric morphometrics". In: *Journal of biomechanics* 41.7 (2008). ISBN: 0021-9290 Publisher: Elsevier, pp. 1545–1554.

[125] Richard Kent et al. *Structural and material changes in the aging thorax and their role in crash protection for older occupants*. Tech. rep. SAE Technical Paper, 2005.

[126] Yulong Wang et al. "A parametric ribcage geometry model accounting for variations among the adult population". In: *Journal of biomechanics* 49.13 (2016). ISBN: 0021-9290 Publisher: Elsevier, pp. 2791–2798.

[127] Ashley A. Weaver et al. "Morphometric analysis of variation in the ribs with age and sex". In: *Journal of anatomy* 225.2 (2014). ISBN: 0021-8782 Publisher: Wiley Online Library, pp. 246–261.

[128] Robert A. Berg et al. "Part 5: Adult Basic Life Support: 2010 American Heart Association Guidelines for Cardiopulmonary Resuscitation and Emergency Cardiovascular Care". en. In: *Circulation* 122.18_suppl_3 (Nov. 2010).

[129] Yvette Koeken et al. "The influence of nonlinear intra-thoracic vascular behaviour and compression characteristics on cardiac output during CPR". en. In: *Resuscitation* 82.5 (May 2011), pp. 538–544.

[130] JOHN P. ROSBOROUGH et al. *Cough supported circulation*. Vol. 9. Issue: 5 Pages: 371-372 Publication Title: Critical Care Medicine. LWW, 1981.

[131] Myron L. Weisfeldt et al. "Physiology of cardiopulmonary resuscitation". In: *Annual review of medicine* 32.1 (1981). ISBN: 0066-4219 Publisher: Annual Reviews 4139 El Camino Way, PO Box 10139, Palo Alto, CA 94303-0139, USA, pp. 435–442.

[132] Myron L. Weisfeldt et al. "Cardiopulmonary resuscitation: beyond cardiac massage." In: *Circulation* 74.3 (1986). ISBN: 0009-7322 Publisher: Am Heart Assoc, pp. 443–448.

[133] Andreas Neurauter et al. "Comparison of mechanical characteristics of the human and porcine chest during cardiopulmonary resuscitation". en. In: *Resuscitation* 80.4 (Apr. 2009), pp. 463–469.

[134] Ali Jalali et al. "Modeling mechanical properties of the chest during the cardiopulmonary resuscitation procedure". In: *Computing in Cardiology 2014*. IEEE. 2014, pp. 13–16.

[135] Dominique François et al. *Mechanical Behaviour of Materials: Volume 1: Micro- and Macroscopic Constitutive Behaviour*. Vol. 180. Springer Science & Business Media, 2012.

[136] GW Schmid-Schönbein et al. "Passive mechanical properties of human leukocytes". In: *Biophysical Journal* 36.1 (1981), pp. 243–256.

[137] CT Lim et al. "Mechanical models for living cells—a review". In: *Journal of biomechanics* 39.2 (2006), pp. 195–216.

[138] S Abramowitch et al. "Introduction to classical mechanics". In: *Biomechanics of the female pelvic floor*. Elsevier, 2016, pp. 89–107.